



Studies of electronic and sensing properties of epitaxial InP surfaces for applications in gas sensor devices

Katarzyna Wierzbowska

► **To cite this version:**

Katarzyna Wierzbowska. Studies of electronic and sensing properties of epitaxial InP surfaces for applications in gas sensor devices. Electronics. Université Blaise Pascal - Clermont-Ferrand II, 2007. English. <NNT : 2007CLF21807>. <tel-00926562>

HAL Id: tel-00926562

<https://tel.archives-ouvertes.fr/tel-00926562>

Submitted on 9 Jan 2014

HAL is a multi-disciplinary open access archive for the deposit and dissemination of scientific research documents, whether they are published or not. The documents may come from teaching and research institutions in France or abroad, or from public or private research centers.

L'archive ouverte pluridisciplinaire **HAL**, est destinée au dépôt et à la diffusion de documents scientifiques de niveau recherche, publiés ou non, émanant des établissements d'enseignement et de recherche français ou étrangers, des laboratoires publics ou privés.

N° d'ordre: D.U: 1807
E D S P I C: 395

UNIVERSITÉ BLAISE PASCAL - CLERMONT-FERRAND II
École Doctorale
des Sciences Pour l'Ingénieur de Clermont-Ferrand

SILESIA TECHNICAL UNIVERSITY, GLIWICE, POLAND
Faculty of Automatic Control,
Electronics and Computer Science

PHD THESIS

presented by

KATARZYNA BARBARA WIERZBOWSKA

Master of Science, Engineer

To obtain academic degree:

DOCTOR OF PHILOSOPHY

SPECIALITY : MATÉRIAUX ET COMPOSANTS POUR L'ELECTRONIQUE

**STUDIES OF ELECTRONIC AND SENSING
PROPERTIES OF EPITAXIAL InP SURFACES FOR
APPLICATIONS IN GAS SENSOR DEVICES**

Public defence took place 14th DECEMBRE 2007 in front of the jury composed
by:

Mr Marcel BOUVET	Head of the jury and Reviewer
Mr Zdzislaw FILUS	Reviewer and Examiner
Mr Edward HRYNKIEWICZ	Examiner
Mrs Boguslawa ADAMOWICZ	Supervisor
Mr Alain PAULY	Supervisor
Mr Luc BIDEUX	Supervisor
Mrs Christelle VARENNE	Invited member

*Mojemu synowi,
ukochanym rodzicom i bratu,
Raphaelowi,
oraz moim bliskim.*

Acknowledgements

My PhD Thesis was realized in the three scientific groups: Gas Sensor Group and Surface Spectroscopy Group in LASMEA, Blaise Pascal University (Clermont-Ferrand) also in Department of Applied Physics, Institute of Physics, Silesian University of Technology (Gliwice). Thus my first, and most earnest, acknowledgment must go to my supervisors: Boguslawa Adamowicz (Gliwice), Alain Pauly and Luc Bideux (Clermont-Ferrand) for carrying out of my scientific development during hard years of PhD Thesis.

I thank Professor Boguslawa Adamowicz for being my scientific mentor from beginning of my scientific work i.e., from MSc Thesis up to PhD one also for her support and constructive discussions. Also great thanks to Professor Alain Pauly that has been instrumental in ensuring the welcome in his research group and financial support of my Thesis. To Professor Luc Bideux for showing me the fascinating world of surface spectroscopy studies.

Special thanks to the jury of my thesis, the reviewers Professor Marcel Bouvet and Professor Zdzislaw Filus, the examiner Professor Edward Hryniewicz for their time, findings and recommendations. Also, special thanks to the invited member Dr Christelle Varenne, her presence in the jury of the Thesis as a full member was impossible because of the administrative reasons of the Thesis in co-tutelle.

For too many people to mention individually have assisted in so many ways during my work. They all have my sincere gratitude. In particular, I would like to thank Dr Jerome Brunet for his guidances, Dr Laure Berry for the discussions, MSc Bernard Lauron and MSc Guillaume Monier for their help that was main in experimental part of my work in LASMEA and finally special thanks to Professor Jean Paul Germain whose voluntary help was instrumental in some theoretical problems of my Thesis; all currently or previously of B. Pascal University.

I also thank to the RCIQE, Hokkaido University, Sapporo for providing the computer simulator for surface analysis and Dr Marcin Miczek for his support in numerical calculations. I am also indebted to MSc Janusz Zywicki from High-Tech Int Services, Rome (owner of PHI 600 SAM system) and Dr Andrzej

Klimasek from Department of Applied Physics, Poland for their help in performing the AES experiment and valuable comments. Also, great thanks to Dr Florence Rollet for the realization of AFM images.

I cannot forget to thank Bernard Michaux for his precious help and many comments in the redaction of the various papers in English. Also, special thanks to Sebastian Lallechere for his help and comments in design of this work. I would like thank to many friends in Poland and France who were instrumental in the success of this studies, especially Marie Chassagne and family Chassagne for their love that they gave to me. Family Vernet for encouraging me in the hard moments and for all kindness they gave to me. Monika Pyka deserves particular credit for her friendship and presence when I needed the discussion. Many thanks also to Anna Trzeciakiewicz that shared with me the student life. For my French friends from Association France-Pologne particularly Colette Kosinski and Wanda Gliwa for their kindness, help and many constructive advices and conversation. I would like to thank Florent Daculty for introducing me into the nuances of rules in administrative life of B. Pascal University. Also, for Elzbieta and Baudime Jam who are my friend from the first time I have met them, and who make me discover the world of music.

This research was supported by Ministry of French Education and partially supported by the Ministry of Science and Higher Education, Poland (Research Project 3348/T02/2006/31).

A penultimate thank-you goes to my wonderful parents Irena and Piotr Wierzbowsky and my brother Robert. For always being there when I needed them most, and never once complaining about how infrequently I visit Poland, they deserve far more credit than I can ever give them.

My final, and most heartfelt, acknowledgment must go to Raphael Vernet for his never ending support in the hardness moments of my work and for his great help in daily and professional life. His support, encouragement, and companionship has turned my journey through PhD studies into a pleasure.

Contents

Acknowledgements	i
Introduction	1
1 Generalities of the atmospheric pollution	7
1.1 Atmospheric pollution	7
1.1.1 Major pollutants	8
1.1.2 Pollutant emission	12
1.1.3 European Commission and air quality	13
1.2 National organisation networks of air quality	13
1.2.1 French national organisation network	13
1.2.2 Polish national organisation network	20
1.2.3 Problematics of analysis used in air quality	21
1.3 Gas sensors	23
1.3.1 Gas sensor characterization	23
1.3.2 Chemical gas sensors	24
1.3.3 Sensitive materials	29
1.3.4 Advantages and disadvantages	32
2 General properties of semiconductor surfaces	35
2.1 Semiconductor surface	35
2.2 Models of surface states	39
2.3 Properties of InP surfaces	42
2.3.1 Native oxides	43
2.3.2 Electronic properties of native oxides	43
2.3.3 Chemical properties of native oxides	44
2.3.4 Native oxide formation	45
2.3.5 InP annealed surface	46
2.4 Adsorption in general	46
2.4.1 Physisorption	47

2.4.2	Chemisorption	47
2.4.3	Adsorption isotherms	48
2.4.4	Adsorption on the semiconductor surface	50
2.5	Ohmic contacts	51
2.5.1	Ohmic contact model	51
2.5.2	Ohmic contact technology	52
3	Experimental	55
3.1	Sensor device	55
3.1.1	n-InP epitaxial layers	55
3.1.2	Ohmic contacts	56
3.1.3	Sensor structure	56
3.2	Gas measurement set-up	59
3.3	Electronic properties characterization	60
3.3.1	The Van der Pauw method	60
3.3.2	Hall measurement cell	62
3.4	Chemical properties of InP surface	62
3.4.1	Secondary electrons	63
3.4.2	Attenuation length of electrons in solids	64
3.4.3	X-ray photoelectron spectroscopy	64
3.4.4	Auger spectroscopy	66
3.4.5	Surface spectroscopy analysis	67
3.4.6	Electron analysers	70
3.4.7	Measuring set-up	73
4	Results and discussion	79
4.1	NO ₂ action on InP surface	79
4.2	Ohmic contacts	82
4.2.1	AES in-depth profile	82
4.2.2	AFM image analysis	83
4.2.3	SEM image analysis	83
4.3	Chemical properties of n-InP surfaces	85
4.3.1	Auger results	85
4.3.2	XPS results	87
4.3.3	Quantitative analysis of XPS	91
4.3.4	AFM images	94
4.4	Studies of electronic properties	96
4.4.1	Principle of rigorous analysis	96
4.4.2	In-depth profiles	97

4.4.3	$N_{SS}(E)$ influence on sensor electronic characteristics . . .	99
4.4.4	Q_{FC} impact on electronic properties of InP	100
4.4.5	Temperature influence on electronic properties	101
4.5	Studies of InP gas sensor	102
4.5.1	Electronic properties	102
4.5.2	NO_2 action on electronic properties of InP	106
4.5.3	Mechanism of NO_2 action	108
4.6	Sensor characteristics	108
4.6.1	Sensor response	109
4.6.2	Response stabilization	112
4.6.3	Selectivity	114
4.6.4	Sensitivity	114
4.6.5	Response time	114
4.6.6	Reproducibility	115
4.6.7	Other parameters	116
Conclusion		119
A Conversion of $\mu\text{g.m}^{-3}$ in ppb		125
B Electron and Hole Statistics in Semiconductors		127
C Hall effect functions		131
D The configuration of Hall effect measurements		133
D.1	Configuration without magnetic field	133
D.2	Configuration with magnetic field	134
E Temperature regulation system		135
F Uncertainties of electrical measurements		137
G Principle of Hall effect measurements		139
References		141
List of publications		153

Introduction

The detection and the concentration measurement of pollutants in atmospheric air have become one of the main European political concern since the late 1970's. Because of the increase in the number of vehicles and international transport as well as with development and industrialization of the cities, a strong degradation of environment is observed. Thus, monitoring and detection of gases, especially primary pollutant like nitrogen dioxide (NO_2) and secondary one like ozone (O_3), become extremely important for environmental protection, industrial process analysis and protecting human health. The numerous study shows the destructive influence of the air pollutants on the human health. Depending on pollutants, they may cause problems of breathing, eye irritating, tracheal burns, bronchiolar and alveolar oedema even to airway destruction resulting in respiratory distress or failure. As a result, scientists in the frame of governmental and non-governmental organisations are developing and optimizing detecting and measuring networks for air quality monitoring. In Poland, one of network organisations working for air quality monitoring is Institute for Ecology of Industrial Areas (IETU) [1,2]. IETU is a research and development unit acting under the Polish Ministry of Environment. In France, regulations on the preservation of air quality are mainly defined by the French law on 'Air Quality and the Rational Use of Energy' (LAURE) dated September 1996. There are around forty organisations governed by this law. They constitute the monitoring network approved by the Ministry of Ecology and called Atmo sites for air quality monitoring [3].

In Polish sites for air quality monitoring, as a gas detector a system called OPSIS is used. In France, it is the system of commercial analysers or diffusion tubes. Measurements of concentration of air pollutants obtained by different commercial gas analysers or OPSIS measuring system are selective and insensitive to interfering gases. Moreover, the obtained gas concentration is very precise and measured in real time. However, the commercial analysers and measuring systems used in measurements, suffer from many inconveniences like their dimensions and their weight. In addition, the price of all commercial gas analysers and their costs during usage are very high. Moreover, they employ more and more complicated technology of measurements. All inconveniences of commercial systems show that the use of other sensitive materials in air quality monitoring seems to be a necessity. Thus, collaborations with different univer-

sities and laboratories are established to find new technological solutions for air quality monitoring. Lately, the most studied solution is the chemical sensor technology [4]. Chemical sensors are these ones where the interaction between the target gas and sensing materials is chemical. Among studied materials used in gas sensing technology are electrolytes [4,5] and semiconductors, e.g., metal oxides [6,7,8,9,10,11], molecular semiconductors [12,13,14,15,16,17] and III-V semiconductors [18,19,20,21,22]. Standard gas sensors are mostly based on metal oxides. However, they are not free from many disadvantages like selectivity problems and working temperature. Very often, they work at high temperatures or are characterized by a very long response time; they miss stability and sensor response reproducibility. Thus, often additional technological solutions are used to make the sensor work, which can complicate and increase the cost of gas sensor. In addition, the technology of the structure based on the metal oxides and molecular semiconductors does not allow for the miniaturization and on-chip co-integration with signal processing and communication circuits.

Desired materials in gas sensor technology need to exhibit a high sensitivity (enough to detect oxidizing gases of concentration less than 50 ppb) and a selectivity to target gas. The sensor signal should be stable and reproducible in time. Also, the fabrication technology has to be easy and not expensive, allowing for easy transport and installing in desired monitoring places (streets, traffics, vehicles, etc.). Recently, studies on III-V semiconductor compounds, including indium phosphide (InP) largely used in micro and opto-electronics, show various advantages of this material (superb electron transport properties with high surface sensitivity, a wide variety of these materials and the availability of advanced nano-technology, etc. [18]) making them attractive also for gas sensor technology.

However, one of the crucial problems in technological progress of III-V based devices is control of the chemical and electronic state of semiconductor surfaces and interfaces since they usually exhibit a high density of non-desired surface states in the energy band-gap. For example, the standard passivated surfaces of these semiconductors, including InP, are usually characterized by a surface state continuum with a minimum density in the range from 10^{11} to 10^{12} $\text{cm}^{-2}\text{eV}^{-1}$ [28]. On the other hand, surfaces exposed to air atmosphere after standard wafer preparation treatments, i.e. cutting and chemical polishing, are covered by hardly to remove native oxide layer. This oxide layer is responsible for an increase of surface state density, which induces a surface band bending and depleted near-surface region in InP. Theoretical studies show that surface states at insulator-InP interfaces play also the key role in the so-called surface Fermi level pinning phenomenon [29,30,31]. This Fermi level pinning may provoke a semiconductor surface totally insensitive for gas adsorption, however weak Fermi level pinning may stabilize the surface electronic parameters like its initial resistance. The standard models largely used in practice for description of

the sensing mechanism in semiconductor gas sensors, including InP-based devices, are usually based on the non-realistic ‘flat bands’ assumption (i.e., perfect surface structure) before gas action. In this context, examinations focused on understanding of electronic status of InP surfaces and near-surface region as well as the role of surface Fermi level pinning in sensing mechanism are of great importance.

In the research group of gas sensors under direction of A. Pauly at LASMEA, Blaise Pascal University in Clermont-Ferrand, the novel resistive sensor devices based on n-type InP epitaxial layers were developed and tested in collaboration with Atmo Auvergne. These devices, in spite of the surface native oxide layer existence as well as surface Fermi level pinning are extremely sensitive to oxidizing gases (NO_2 and O_3) of concentration less than 50 ppb. In addition, the InP layer initial resistance in pure air is observed to be very stable in time, probably because of the properties of the native oxide layer and as following electronic properties of InP. Moreover, due to single-crystal structure of InP material - obtained by means of Molecular Beam Epitaxy (MBE) - in comparison with metal oxides (usually of grain structure) and molecular semiconductors (macrocyclic compounds) the gas sensitive InP layers can be well controlled in terms of such important characteristics like layer thickness, doping level, conductivity and carrier mobility. Thus, InP is a very promising material for oxidizing gas sensors, which can be used in both indoor and outdoor applications [14,15,20,21,22,23,24,25,26,27].

Therefore, the main **aim** of the presented Thesis is complex studies - both experimental and theoretical - on the sensing, electronic and chemical properties of n-type InP epitaxial film resistive sensors for oxidizing gases. The result of the performed research is important for further development and optimization of InP thin film sensor technology.

The **scope** of the Thesis contains:

- Fabrication of the series of n-InP based gas sensors with different InP active layer thickness (from 0.2 to 0.4 μm) and examination of their sensing properties in terms of the resistance changes under adsorption of gases (NO_2) of very low concentration (in the range below 50 ppb) and at different working temperatures (from room temperature to 100 °C);
- The Hall experiment (before and under gas adsorption) in order to get information about charge carrier concentration and mobility;
- Characterization of the chemical properties of the surface of InP epitaxial layers before and after gas action, using X-ray photoelectron spectroscopy (XPS) and Auger electron spectroscopy (AES) combined with ion sputtering in order to get in-depth chemical composition profile of InP-related native oxides;

- Theoretical analysis of the influence of surface states and temperature on the electronic parameters of the near-surface region (surface band bending, charge concentration profiles) as well as resistance of InP samples.

The presented work was realized within the following laboratories:

- gas sensor laboratory under direction of A. Pauly in LASMEA, B. Pascal University (France), where the InP sensor devices are fabricated and the gas sensing studies as well as Hall effect measurements are performed;
- laboratory for spectroscopic studies of chemical properties of solid surfaces under direction of L. Bideux also in LASMEA, B. Pascal University (France), where the XPS studies are carried out;
- laboratory for numerical modelling of semiconductor surfaces as well as laboratory of AES microscopy for chemical characterization of solid surfaces and interfaces in the Department of Applied Physics Institute of Physics, Silesian University of Technology (Poland) under direction of B. Adamowicz, where the rigorous analysis of electronic properties as well as AES measurements combined with in-depth sample profiling are realized.

Synopsis of the Thesis

In Chapter 1, characteristics of existent air pollutants, their impacts on human health and concentration limits in air quality monitoring are described. National organisations working in the frame of international programs are also presented. Different methods of detection and monitoring of air pollutants from commercial solutions to studied ones are discussed.

Chapter 2 deals with different approaches to understand the phenomena on the semiconductor surfaces and interfaces. The InP near-surface properties in terms of contamination and native oxide layer are also presented. Moreover, the adsorption process as well as adsorption isotherms allowing to better understanding the gas action on the semiconductor surface are shown. The role of the near-surface region in the adsorption process is also described. In addition, the importance of realisation of the high quality ohmic contacts in resistive gas sensing technology is explained.

In Chapter 3, the sensor structures based on n-InP epitaxial layers (with a layer thickness from 0.2 to 0.4 μm) are presented. The fabrication process of the sensor structure, which consists of the ohmic contact fabrication, mounting of the sensor structure on the heating substrate and wire mounting for output signal registration, is described in detail. Also, the idea and realization

of measuring set-up used in gas sensing studies and Van der Pauw measurement method implemented in Hall effect measurements are explained. This set-up allows for controlling of gas flow, sensor working temperature, time of gas exposure and gas concentration (from very low – less than 50 ppb – to rather high values of few ppm). The chemical properties are studied by means of Auger electron spectroscopy (AES) and X-ray photoelectron spectroscopy (XPS); AES and XPS techniques are presented. Measuring set-ups regarding both of these techniques are detailed as well as methods for qualitative and quantitative analysis.

In Chapter 4, the results of sensing, electronic and chemical systematic studies of the fabricated n-InP-based gas sensors are presented. Their sensing properties are investigated in terms of the sensor response, selectivity, reproducibility and stability. The investigation of the influence of such an important parameter as temperature on sensor characteristics is also shown. The sensor response is studied in terms of n-InP resistance changes as a function of gas concentration. Also, the Hall effect measurement in a novel configuration, which allows for experiment under NO₂ exposure, is carried out to investigate the concentration of charge carriers as a function of gas concentration. In addition, from the Hall effect measurements such the sensor electronic parameters are determined, like the Hall resistivity, mobility and charge carrier concentration. Furthermore, the results of spectroscopic (XPS, AES) studies are discussed. They are performed in order to understand better the chemical composition of n-InP near-surface region and its changes due to gas action. For the first time in the literature, the AES quantitative analysis combined with in-depth profiling (upon argon ion sputtering) is applied for the detailed characterization of the chemical composition of the InP related native oxide layer. The changes in the chemical composition of the sensor surface upon gas action are studied by means of XPS technique and Atomic Force Microscopy (AFM). The quantitative analysis of XPS peak intensities and surface roughness obtained from AFM images of the InP surface are discussed. Moreover, from the quantitative analysis of combined XPS and AES spectroscopic studies, the complementary information about the complex composition of the native oxide layer is obtained. Generally, a native oxide layer is produced during exposure of a freshly prepared free surface to ambient conditions. This complex oxide layer strongly influences the near-surface region and thus is probably responsible for sensing mechanism to NO₂ in the InP sensor device [20,21,22]. However, L. Talazac et al. [14,15,23,24,26,27,32,33,34,35] do not take into account in their considerations the oxide layer formation at free InP surfaces and its influence on the sensing mechanism. Therefore, in this Chapter the phenomenological approach resulting from surface spectroscopy studies, which allows for better understanding the action of NO₂ on the n-InP gas sensor surface, is discussed.

Moreover, in Chapter 4 the electronic status of n-InP surfaces is studied theoretically by means of a rigorous computer analysis. This analysis takes into

account the influence of continuous surface states on the parameters of the surface space charge layer and thus on the InP layer conductivity. This is done for the first time in case of the thin InP layers. The applied computer program was developed at the Research Center for Integrated Quantum Electronics at Hokkaido University in Sapporo (Japan) by the group of H. Hasegawa [28,29,30,31,36,37,38,40]. This unique computer tool uses a one-dimensional Scharfetter-Gummel-type vector matrix algorithm for self-consistent solving of the Poisson's equation and charge transport equations for electrons and holes in a semi-infinite sample at room temperature (at the equilibrium and non-equilibrium conditions). As a result, profiles of carrier concentrations $p(x)$ and $n(x)$ as well electric potential $V(x)$ are obtained and then various surface parameters, including the surface potential, the surface Fermi level position and the surface resistivity are calculated. In calculations, an U-shaped continuum of surface states is assumed with the density distribution $N_{SS}(E)$, in accordance with the DIGS model for semiconductor surfaces and interfaces. Such a $N_{SS}(E)$ distribution has been found experimentally for III-V surfaces covered by native oxide or passivation layer [28]. The surface band bending is induced by both surface states $N_{SS}(E)$ and the surface fixed charge Q_{FC} that represents ions adsorbed on the semiconductor surface or surface-doping. These two parameters are largely used for the modification of electronic properties of semiconductor surfaces.

In addition, the investigation of the quality of ohmic contacts is done in terms of the specific resistivity studies. The Scanning Electron Microscopy (SEM) images of the boundary region between the n-InP surface and contact are also presented. Moreover, AES in-depth profiles and AFM images of the ohmic contacts are shown in Chapter 4.

Additionally, the appendixes contain:

- the method of conversion of $\mu\text{g}\cdot\text{m}^{-3}$ in ppb, units used in gas concentration measuring;
- the statistics of electrons and holes in the semiconductor;
- the graphical representation of the functions used in determination of the Hall effect parameters and electron mobility;
- the diagram of electrical systems used in Hall measurements;
- the scheme of Wheatstone bridge used in temperature control of sensor devices;
- the method of measurement uncertainty estimation;
- the Hall effect principle.

Chapter 1

Generalities of the atmospheric pollution

Air is the foremost element required for life, from some literature data we breathe about 15 000 litres of air, every day [3]. The average composition of dry air is 78% of nitrogen (N_2), 21% of oxygen (O_2) and 1% of other gases, mainly Argon (Ar) followed by carbon dioxide (CO_2). It should be noted that many other constituents exist in much lower concentrations. An air pollutant can be defined as a substance present at a concentration sufficiently above its normal level to produce a measurable adverse effect on human, animal or plant life or on materials.

Air pollution may have natural (volcanic eruptions, vegetal emissions, humid zones, etc.) or anthropogenic origins, i.e., linked to human activity (fixed or mobile combustion sources, industrial emissions, etc.). Pollutants can also be divided into primary pollutants which are emitted directly, and secondary pollutants which are created by chemical transformations in the atmosphere. Thus, this Chapter deals with the variety of atmospheric pollutants, their influence on the human health and environment. The standard concentration of pollutants in air atmospheric is also shown. Moreover, the methods of their detection and measurements are presented.

1.1 Atmospheric pollution

In both developed and rapidly industrialising countries, the level of atmospheric pollutants has been observed to arise; it originates from the combustion of fossil fuels such as coal for domestic and industrial purposes. As a result of changing fuel-use patterns, the increasing use of cleaner fuels such as natural gas, and the implementation of effective smoke and emission control policies the level of one of the major atmospheric pollutant, sulphur, has diminished. However, petrol and diesel-engined motor vehicles emit a wide variety of pollutants,

principally carbon monoxide (CO), nitrogen oxides(NO_x), volatile organic compounds (VOCs) and particulates, which have an increasing impact on urban air quality. Therefore, in both developed and developing countries, the major threat to clean air is now posed by traffic emissions.

Additionally, NO_2 takes place in photochemical reactions resulting in the formation of ozone, a secondary long-range pollutant, which may impact in rural areas often far from the original emission site.

1.1.1 Major pollutants

The principal pollutants produced by industrial, domestic and traffic sources are as follows [44]:

Sulphur Dioxide (SO_2)

It is a corrosive acid gas which combines with water vapour in the atmosphere and produces acid rains. It has been implicated in the damage and destruction of vegetation and in the degradation of soils, building materials and watercourses. SO_2 in ambient air is also associated with asthma and chronic bronchitis. The principal source of this gas is power stations burning fossil fuels which contain sulphur. Now, major SO_2 problems only tend to occur in cities, in which coal is still widely used for domestic heating, in industry and in power stations. As some power stations are situated far away from the cities, SO_2 may affect air quality as well in rural as in urban areas. In most European countries, SO_2 pollution is no longer considered as a significant threat to health since the general decline in domestic coal burning in cities and in power stations.

Particulate Matter (PM)

It is airborne particulate matter which varies in physical and chemical composition, source and particle size. They can be small enough, like PM_{10} particles less than $10\ \mu\text{m}$, to penetrate deep into the lungs and so potentially pose significant health risks. Larger particles normally are not inhaled and are removed relatively efficiently from the air by sedimentation. But they create dirt, odour and visibility problems. There exist the primary particulate matter (those emitted directly into the atmosphere) and secondary (those formed or modified in the atmosphere from condensation and growth). A major source of the pollution of primary particles are combustion processes, in particular diesel combustion. Secondary particles are typically formed when low volatility products are generated in the atmosphere. The atmospheric lifetime of particulate matter is strongly related to particle size, it may be 10 days for particles of about $1\ \mu\text{m}$ in diameter.

Carbon monoxide (CO)

It is produced almost entirely from road traffic emission. It is a toxic gas which is emitted into the atmosphere as a result of combustion processes; it may be also formed by the oxidation of hydrocarbons and other organic compounds. CO may reduce the oxygen-carrying capacity of the blood. The CO atmospheric lifetime is a period of approximately one month but it is eventually oxidized to carbon dioxide (CO₂).

Nitrogen Oxides NO and NO₂

They are formed during high temperature combustion processes from the oxidation of nitrogen in the air or fuel. The principal nitrogen oxide released into the atmosphere is nitrogen oxide (NO) and forms from reaction with ozone or oxygen, nitrogen dioxide (NO₂). The principle source of NO and NO₂ is road traffic, which is responsible for approximately half the emissions in Europe. Thus, NO and NO₂ concentrations are greatest in urban areas where traffic is the biggest problem. Other sources are power stations and industrial processes.

Nitrogen dioxide is a molecule constituted of two atoms of oxygen and one atom of nitrogen, the angle between two atoms of oxygen is 134.3 ° and the distance between oxygen and nitrogen atoms is equal to 119.7 pm. Figure 1.1 shows the scheme of NO₂ molecule [41].



Figure 1.1: *Representation of the molecule of NO₂.*

It exists in the forms of NO₂, NO₂⁻ and NO₂⁺, the O–N–O angle changes with the form being equal to 180 ° for NO₂⁺ and 115 ° for NO₂⁻. Also, the N–O distance modifies, being equal to 115.4 pm for NO₂⁺ and 123.6 pm for NO₂⁻.

Nitrogen dioxide has a variety of environmental and health impacts. It is a respiratory irritant and may exacerbate asthma. In addition, it is a strong oxidizing gas with characteristic odour. At elevated concentration levels (more than 200 µg.m⁻³), NO₂ is strongly toxic. The elevated levels occur in urban environments under stable meteorological conditions because the airmass is unable to disperse it. Moreover in the presence of sunlight, it reacts with hydrocarbons to produce photochemical pollutants such as ozone. Additionally, nitrogen oxides have an atmospheric lifetime of around one day with respect to conversion to nitric acid (HNO₃). The nitric acid is directly deposited to the ground or transfers to aqueous droplets (e.g., cloud or rainwater), as resulting in a contribution to acid deposition.

Ozone (O_3)

Two types of ozone are known. The first is the stratospheric one (on the level from the ground to between 15 and 35 km with concentration around 10 ppm) which protects us from some ultraviolet (UV) radiation. The second type is the 'ground level' ozone; it is an atmospheric secondary pollutant produced by reaction between nitrogen dioxide, hydrocarbons and sunlight. Ozone is a strong oxidant and strongly reactive chemical. It is capable to attack surfaces of fabrics and rubber materials. It is characterized by blue colour and strong odour. Ozone can irritate the eyes and air passages causing breathing difficulties. Also it may increase susceptibility to infection. Moreover, it is very toxic to some crops, vegetation and trees.

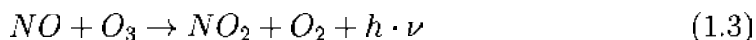
The formation of ozone is with participation of nitrogen dioxide by photochemical reaction:



The products of that photochemical reaction are nitrogen oxide and atomic oxygen. This atomic oxygen can combine with molecular oxygen and creates ozone:



However, the ozone pollution level is not as high in urban areas (where high levels of NO are emitted from vehicles) as in rural ones, by reason of decomposing ozone by nitrogen oxide into forms oxygen and nitrogen dioxide:



As sunlight energy causes ozone formation, near-ultra-violet radiation dissociates stable molecules to form reactive species known as free radicals. Thus, in the presence of nitrogen oxides, these free radicals catalyse the oxidation of hydrocarbons to carbon dioxide and water vapour. Partially oxidized organic species such as aldehydes, ketones and carbon monoxide are intermediate products, with ozone being generated as a by-product. Since ozone itself is photodissociated to form free radicals, it promotes the oxidation chemistry and so catalyses its own formation. So, the elevated levels of ozone are generally observed during hot, still, sunny, summertime weather in places where the air-mass has previously collected emissions of hydrocarbons and nitrogen oxides (e.g., urban areas with traffic). The ozone pollution or 'summertime smog' may have a lifetime of up to several days and be transported over long distances.

Ammonia (NH_3)

It occurs naturally in the rural zones as a product of natural decomposition of organic matter. Under unusual conditions it can reach dangerous concentrations. Ammonia is also produced by the reaction of hydrogen with nitrogen.

About 80% of the ammonia is used in fertilizers. It is also used as a refrigerant gas. It can be found in manufacture of plastics, explosives, pesticides, other chemicals (e.g., as a corrosion inhibitor, as a component of household cleaners, in the pulp and paper, metallurgy, rubber, food and beverage, textile and leather industries) and of pharmaceuticals. Ammonia is a colourless gas with a very distinct odour but it can be dissolved in water. Once exposed to open air, liquid ammonia quickly turns into a gas. Inhalation of ammonia may cause nasopharyngeal and tracheal burns, bronchiolar and alveolar oedema, or airway destruction resulting in respiratory distress.

Hydrocarbons

There are two main groups of hydrocarbons:

- volatile organic compounds (VOC), with its two most important representants: benzene and 1,3-butadiene. Benzene is an aromatic VOC, with a chemical structure of six carbon and six hydrogen atoms, is a minor constituent of petrol (around 2% by volume). So, the main sources of this pollutant in atmosphere are distribution and combustion of petrol. Benzene is emitted also as a product of the decomposition of other aromatic compounds. As for 1,3-butadiene, its molecule comprises four carbon and six hydrogen atoms. At ambient temperature, it is a gas and trace amounts can be found in the atmosphere that we breathe. Benzene and 1,3-butadiene derive mainly from the combustion of petroleum in motor vehicle engines and from other sources such as fossil fuels and accidental fires. They are also known as a human carcinogen.
- polycyclic aromatic hydrocarbons (PAH) that mainly include Toxic Organic Micropollutants (TOMP) which are produced by the incomplete combustion of fuels.

Lead (Pb) and heavy metals

They are in form of particulates in air. They result from activities such as fossil fuel combustion (including vehicles), metal processing industries and waste incineration. Lead is the most widely used non-ferrous metal and has a large number of application in industry like world-wide industrial use in the manufacture of batteries (60-70% of total consumption of 4 million tons) and it is also used in paints, glazes, alloys, radiation shielding, tank lining and piping. Lead is a cumulative poison to the central nervous system, particularly to the mental development of children.

Acid deposition

It may be either wet or dry. It contains of compounds resulting principally from the SO₂ and NO₂ oxidation and from fossil fuel combustion. Acidification

of environment (water and soils) has got a consequent impact on agriculture, forestry and fisheries.

1.1.2 Pollutant emission

As the number of vehicles and international transport increases every year with the development of the countries, this results in increase in level of four major pollutants (SO₂, NO_x, VOCs and ammonia) responsible for acidification, eutrophication and formation of ground-level ozone. Thus, the Table 1.1 shows the percentage part of emitted pollutants from transport in global emission of these pollutants.

Table 1.1: *The % of emitted pollutants from the transport in global emission [42].*

Pollutant	CO ₂	CO	NO _x	SO ₂	Hydrocarbons
Emission (%)	33	26	52	6	22

Especially in the cities under stable meteorological conditions where the airmass is unable to disperse the produced by automobiles pollutants, establishment of the maximum concentration limit of each pollutant is necessary. Table 1.2 shows the maximum concentration limit for the major pollutants present in atmospheric air. In case of overflow the concentration limit of NO_x, hydrocarbons and O₃, the public is supposed to be informed.

Table 1.2: *The norms of pollutant concentration [3].*

Pollutant	Limit concentration ($\mu\text{g}\cdot\text{m}^{-3}$)	Comments
CO	> 10 000	Average concentration per 8 hours
NO _x	> 200	Average concentration per hour
SO ₂	> 300	Average concentration per hour
Hydrocarbons (Benzene)	> 5	Average concentration per year
PM	> 50	Average concentration per day *
O ₃	> 180	Average concentration per hour
* supposes not overflow 35 days per year		

1.1.3 European Commission and air quality

One of the aims of European Commission (EC) for air quality is:

‘Protecting, preserving and improving the environment for present and future generations, and promoting sustainable development.’

As air pollutants are transported in large quantities across national boundaries, individual country cannot in general meet the air quality objectives within their territory by national action alone. Thus, the detection and concentration measurement of pollutants in air atmosphere have become extremely important for environmental protection and industrial process analysis and have been one of Europe’s main political concerns since the late 1970s.

The control of emissions from mobile sources, improving fuel quality, promoting and integrating environmental protection requirements into the transport and energy sector are part of the aims of European Union policy on air quality. This is why the Establishment of National Emission Ceilings was set to limit acidification, eutrophication and formation of ground-level ozone. The Directive 2001/81/EC of the European Parliament and the Council on National Emission Ceilings for certain pollutants (NEC) set upper limits for each Member State for the total emissions in 2010 (see Table 1.3) of the four pollutants, which are SO₂, NO_x, VOCs and ammonia. These national emission limits are designed with the aim of broadly meeting the interim environmental objectives set out in Article 5 [43].

Based on the provisions of the Directive, Member States are obliged to report each year their national emission inventories and their projects for 2010 to the European Commission and the European Environment Agency. They shall also draw up national programs in order to demonstrate how they are going to meet the national emission ceilings by 2010. The first year for drawing up national programs was 2002. There are currently no EC standards for metals other than lead, although several are under development.

1.2 National organisation networks of air quality

To follow the obligations of European Commission, each European country has got its own network of air quality monitoring. The associations for air quality measurements are structured differently in each country. Thus, this section deals with the national organisation network of quality air measurements in France and Poland.

1.2.1 French national organisation network

French regulations on the preservation of air quality are mainly defined by the French law on ‘Air Quality and the Rational Use of Energy’ (LAURE) dated

Table 1.3: *National Emission Ceilings for SO₂, NO_x, VOC and NH₃, to be obtained by 2010 (in kilotons) [43].*

Country	SO ₂	NO _x	VOC	NH ₃
Austria	39	103	159	66
Belgium	99	176	139	74
Bulgaria	836	247	175	108
Cyprus	39	23	14	9
Czech Republic	265	286	220	80
Denmark	55	127	85	69
Estonia	100	60	49	29
Finland	110	170	130	31
France	375	810	1050	780
Germany	520	1051	995	550
Greece	523	344	261	73
Hungary	500	198	137	90
Ireland	42	65	55	116
Italy	475	990	1159	419
Latvia	101	61	136	44
Lithuania	145	110	92	84
Luxembourg	4	11	9	7
Malta	9	8	12	3
Netherlands	50	260	185	128
Poland	1397	879	800	468
Portugal	160	250	180	90
Romania	918	437	523	210
Slovakia	110	130	140	39
Slovenia	27	45	40	20
Spain	746	847	662	353
Sweden	67	148	241	57
United Kingdom	585	1167	1200	297
EC27	8297	9003	8848	4294

30th September 1996. The aim of this law is to ‘implement the recognised right of each person to breathe air that is not harmful to their health’ [3,45]. The local region Atmo associations, created in the name of this law, aim to measure and monitor certain air pollutants over all the regions, in particular in urban areas. There are around forty Atmo located in the different regions in France (see Fig. 1.2). In the case of Clermont-Ferrand, it is Atmo Auvergne. These associations are governed by the French law and constitute the monitoring network approved by the Ministry of Ecology. Atmo are members of the federation of the forty approved French Air Quality Monitoring Associations (AASQA) group.



Figure 1.2: Location of the Atmo sites in France [3].

Among all the pollutants, Atmo mainly measures pollutants targeted by European and French regulations or draft regulations setting concentration thresholds. The main gaseous pollutants measured are sulphur dioxide, nitrogen dioxide, ozone, carbon monoxide, certain volatile organic compounds, particles in suspension (PS), lead and heavy metals. Moreover, Atmo associations conduct analysis of pollen concentration in air and measurements of the radioactivity.

Basic aspects of pollutants detection and measurements

In principle, the Atmo stations of air quality monitoring localized in the urban areas mainly, consist of air pollutant analysers or passive diffusion tubes. There exists a variety of methods used in commercial analysers. Usually, one commercial analyser embodies of one method adapted to detect and measure the concentrations of target pollutant. The methods corresponding to measured gases are normalized and are collected in the Table 1.4. The standard unit of pollutant concentration is the $\mu\text{g}\cdot\text{m}^{-3}$ and the concentration measured by the analyser is expressed in ppm or ppb. Table 1.5 represents the calculated concentration of 1 ppb of detected major pollutants at 25 °C.

Analysis method of pollutant detection

The normalized methods used in analysers are as follows:

Table 1.4: *Analysis methods for different air pollutants [3].*

Pollutant	Analysis method
CO	IR absorption
SO ₂	UV fluorescence
NO _x	Chemi-luminescence, passive diffusion tube
O ₃	UV photometry, passive diffusion tube
VOC	Flame ionisation and photometry, passive diffusion tube

Table 1.5: *Calculated concentrations for 1 ppb of gas molecules.*

Gas	1 ppb of gas expressed in $\mu\text{g}\cdot\text{m}^{-3}$
CO	1.15
SO ₂	2.62
NO	1.23
NO ₂	1.88
O ₃	1.96

- CO detection by IR absorption:** this method is based on the infrared (IR) absorption properties of CO molecules. The sample of air analysed by this method is introduced into the measuring cell. While IR light passing through the measuring cell, which contains CO, all the waves corresponding to the CO absorption specific wave are absorbed by CO molecules. After IR passage, the light is collected by photodetectors. The detected IR spectrum is compared with the reference spectrum. Its difference is a function of CO concentration. This analysis is characterized by a measurement range from 0 to 200 ppm and a response time of 20 s.
- measurements of SO₂ by UV fluorescence:** this method consists of light excitation (with a wavelength equal to 214 nm) of the SO₂ molecules:



The return of the excited molecules of sulphur dioxide SO₂* to their initial state is accompanied by the fluorescence phenomenon. This analyser works in the measuring range from 0.05 to 10 ppm and its response time is around 20 s.

- NO_x analysis by chemi-luminescence:** this method involves in the first step the oxidation of NO molecules. The sample of air, which contains NO₂ and NO molecules, is introduced into the measuring cell with O₃ and the oxidation of the NO molecules takes place:



In this reaction the excited molecule of nitrogen dioxide is produced. While return to its initial state, the molecule emits the wave light with a length between 600 and 1200 nm (chemiluminescence). This light intensity is measured by photointensifier and is proportional to the NO concentration in analysed air sample. In the second step, in parallel, the second air sample is introduced in the molybdenum catalytic oven where the reduction of NO₂ molecules into NO is obtained. After that, the concentration of NO is measured by chemiluminescence. The difference between the NO concentration measured in the first and the second step gives the total NO₂ concentration in the investigated air sample. In this method, the measurement range is from 0 to 10 ppm and the measurement duration is around 30 s.

- **O₃ analysis by UV photometry:** this method is based on the UV absorption spectrum of the molecules of ozone, in general with wavelength from 200 to 320 nm; the maximum of absorption is at 253.7 nm. The UV light passes through the measuring cell and is collected at the end by the photodetectors. In the measuring cell, two different samples of analysed air are introduced. The first one is free from ozone contamination because of using gas filters to purify air, the second one is the air to analyse. After a comparison of the detected UV light passed through the air sample with and without ozone contamination, the ozone concentration could be obtained. This analyser allows for a measurement range from 0 to 10 ppm and for a measurement duration of around 20 s.
- **VOC detection by photometry and flame ionisation:** this method uses a selective adsorbent; the sample of air is introduced into the tube, which contains a selective adsorbent where the adsorption process takes place. After the desorption by heating of the capillary tube, the chromatographic separation of desorbed compounds is realized. Finally, the detection of the compounds is carried out by the flame ionisation detector or flame photometry detector.

The detection by flame ionisation consists of the decomposition of organic molecules into ions. The compounds coming from the tube are mixed with hydrogen and pass through the flame where the ionisation process takes place. The ions are captured on the polarised electrode and the signal electric produced by capturing the ions is proportional to the gas concentration. This method is very sensitive to gases like methane (CH₄) or ethane (C₂H₆).

The detection by flame photometry allows for the sensitive and selective measurements of the sulphurous and phosphorus compounds. The detection principle is to excite the sulphurous or phosphorus compounds by flame intermediation. After, in the tube equipped with a photomultiplier, the measurements of the chemiluminescence emission are done. The

chemiluminescence emission is characteristic for each compound and is proportional to its concentration. The measurement range is from 100 to 1000 ppm and the response time is around 20 s.

- **passive diffusion tube:** in this method, the pollutant molecules diffuse into the diffusion tube through an air column. This column is permeable for the passing molecules up to the moment when they are trapped by a specific adsorbent. The evaluation of target pollutant concentration is done in the laboratory where reaction products between target pollutant and its adsorbent are investigated. Table 1.6 represents the different substances used in measurements and their correspondent among pollutants.

Table 1.6: *Specific absorbents and their corresponding pollutant used in passive diffusion tube [3].*

Pollutant	Adsorbent
SO ₂	Carbonate of potassium + glycol
NO ₂	Triethanolamine
O ₃	1.2 di(peridyl)ethylene
Benzene, toluene	Active carbon

Table 1.7: *Thresholds used to define index levels based on regulatory criteria on air quality [3].*

Sub-indexes	Indexes	NO ₂ scale		SO ₂ scale		O ₃ scale		PS Average daily concentrations for the various sites µg/m ³
		Average of the hourly maximum for the various sites						
		µg/m ³	ppb	µg/m ³	ppb	µg/m ³	ppb	
1	Very good	0 - 29	0 - 15	0 - 39	0 - 15	0 - 29	0 - 15	0 - 9
2	Very good	30 - 54	16 - 28	40 - 79	16 - 30	30 - 54	16 - 27	10 - 19
3	Good	55 - 84	29 - 44	80 - 119	31 - 45	55 - 79	28 - 40	20 - 29
4	Good	85 - 109	45 - 57	120 - 159	46 - 60	80 - 104	41 - 53	30 - 39
5	Average	110 - 134	58 - 71	160 - 199	61 - 76	105 - 129	54 - 65	40 - 49
6	Poor	135 - 164	72 - 87	200 - 249	77 - 95	130 - 149	66 - 76	50 - 64
7	Poor	165 - 199	88 - 105	250 - 299	96 - 114	150 - 179	77 - 91	65 - 79
8	Bad	200 - 274	106 - 145	300 - 399	115 - 152	180 - 209	92 - 107	80 - 99
9	Bad	275 - 399	146 - 212	400 - 599	153 - 229	250 - 359	127 - 183	100 - 124
10	Very bad	≥ 400	≥ 213	≥ 500	≥ 191	≥ 240	≥ 122	≥ 125

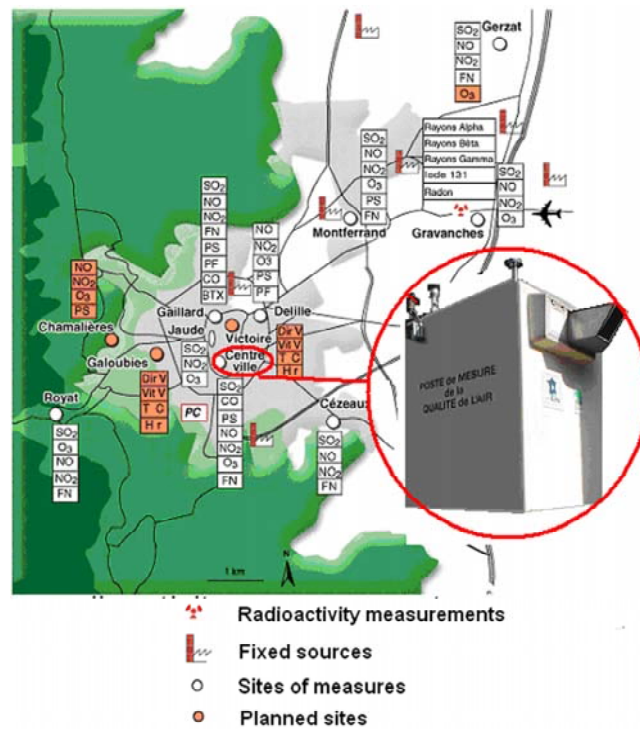


Figure 1.3: Location of the air quality measuring Atmo sites in Clermont-Ferrand [3].



Figure 1.4: Atmo panel displaying air quality level installed at Place Galliéni in Clermont-Ferrand [3].

Measured pollutants

In September 1997, Clermont-Ferrand became the first French city where the installation of an urban station network specialized in public information on air quality took place. Figure 1.3 shows the location of the measuring sites in Clermont-Ferrand. The pollutant level is displayed by two Atmo panels, installed at Place Delille and Place Galliéni (Figure 1.4). The displayed Atmo air quality level is based on calculated indexes. This information is transmitted by the central unit and is daily updated [3]. Table 1.7 shows the indexes representing the air quality level, calculated for the four pollutants SO_2 , NO_2 , O_3 and PS. Used since January 2005, this calculation method is defined by the French law dated July 2004 governing air quality indexes.

1.2.2 Polish national organisation network

In Poland, one of the organizations for air quality monitoring is the Institute for Ecology of Industrial Areas (IETU). It is working in collaboration with the World Health Organisation, U.S. Environmental Protection Agency, U.S. Department of Energy, EC and European Union. IETU is a research and development unit acting under the Polish Ministry of Environment. It has been functioning under its present name since 1992.

The goal of the scientific and research activities of IETU is to develop basis for policies and strategies aimed at sustainable development of the environment of urbanized and industrialized areas [1,2].

Analysis method and the location of air quality monitoring sites

Within the research programs of IETU, the installing of a measuring system for air quality monitoring in the Polish cities is realized. This system is called OPSIS and produced by OPSIS AB in Furulund, Sweden [2]. Figure 1.5 shows photos of OPSIS. OPSIS works on the base of Differential Optical Absorption Spectroscopy (DOAS).

In this concept, light with a wavelength from 200 to 1800 nm is emitted from a source to detector, the distance between them may be from 200 to 2000 m. In the detector, light is sent by a wave guide to the photo analyser. During the light passage, the absorption by air pollutants appears. The measured adsorption spectrum is specific for each air pollutant.

OP SIS was successively installed in cities in the years of 1992–1996 (see Figure 1.6) and it is used to measure [1,2]:

- urban pollutants emitted from city transport (Warszawa, Bydgoszcz, Poznan, Torun, Tarnobrzeg, Pszczyna),

- the pollutant level emitted in industrial process (Czestochowa, Bielsko-Biala, Lublin, Czechowice-Dziedzice, Katowice),
- the pollutant level in the urban area (Gdansk, Wloclawek, Plock, Lodz).



(a) The source.



(b) The detector.

Figure 1.5: Photos of OPSIS measuring system in Poznan, Poland [2].



Figure 1.6: Location of air-quality measuring sites in Poland.

1.2.3 Problematics of analysis used in air quality

In conclusion, measurements of concentration of air pollutants obtained by different commercial gas analysers or OPSIS measuring system are selective and insensitive to interfered gases. Moreover, the obtained gas concentration is

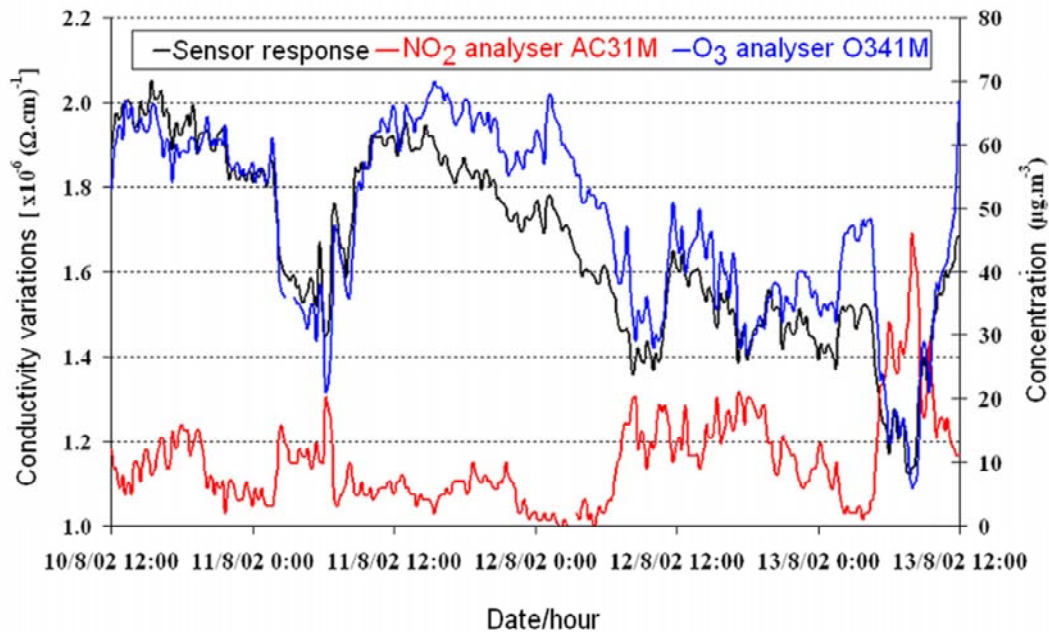


Figure 1.7: *Phthalocyanine based sensor response toward atmospheric pollutants at 50 °C [14].*

measured very precisely and in real time, instead of diffusion tubes. However, commercial analysers and measuring systems suffer from many inconveniences like their dimensions and weight. Moreover, gas analysers work at constant temperature and they need a special treatment like regular calibration, which results in increase in their cost while using. All commercial gas analysers are rather expensive and employ more and more complicated technology of measurements.

As an alternative, diffusion tubes are rather cheap but the pollutant concentration needs to be obtained in laboratory conditions. Thus, the pollutant concentration is the average of the concentration measured during the measurement period. Additionally, tube measurements are sensitive to climatic variations.

All the inconveniences of commercial solutions indicate that the use of other methods in air quality preservation seems to be a necessity. Thus, collaborations among different universities and laboratories are established. One of the results of these collaborations is the use of chemical gas sensors on the base of phthalocyanine and indium phosphide (InP) as sensitive materials. It was realized within the frame of the projects between Atmo Auvergne and the research group of gas sensors under direction of A. Pauly of Blaise Pascal University. The novel resistive and Schottky-type [14,15,19] InP based sensors were fabricated and successfully tested in outdoor applications [14,15,26]. Figure 1.7 represents obtained results for a phthalocyanine based sensor.

1.3 Gas sensors

Gas sensitive materials used as gas sensors are various: from metals as the catalytic gate, through crystalline and molecular semiconductors, to insulators implemented in different transistor structures. Thus, in this section, a short survey through used materials as gas sensors and their characteristic features is presented.

1.3.1 Gas sensor characterization

Chemical gas sensors are characterized by different important parameters as follows:

- **selectivity** : it is the ability of gas sensor to distinguish target gases from the gas mixture. Usually, sensors are selective to a certain category of gases like oxidizing gases or reducing ones.
- **sensitivity** : it is the ratio between the sensor signal output variations ΔS and variations of the measured quantity ΔC . In the case of gas pollutants, C is the gas concentration.

$$S = \lim_{\Delta C \rightarrow 0} \frac{\Delta S}{\Delta C} \quad (1.6)$$

The maximum of the sensor sensitivity is obtained when small variations of the gas concentration produce a maximum of signal output fluctuation.

- **response time** : it is the amount of time required to process the signal response from the sensor initial contact with the gas. In practice, it is the sensor signal rise time from 10 to 90% [46].
- **reversibility** : it is the ability of the gas sensor to return to its initial state once the gas action is finished and the target gas is not at the reach distance of the gas sensor. This parameter is directly linked to the reversibility of physical or chemical reactions. It influences the reproducibility of results.
- **reproducibility and stability** : they are parameters describing the gas sensor ability to stay stable in the time. Moreover, sensing parameters are supposed not to change as a function of number of exposures to gas. In the case of the chemical gas sensor, this criterion is very difficult to implement because it may suffer from gas poisoning and as a result, the ageing effect is observed.
- **recovery time** : it is the necessary time for the gas sensor to return to its initial state.

- **resolution** : it is the necessary concentration quantity of air or gas that produce a visible sensor device signal.
- **range of measurements** : it is the range of the gas concentration for which the produced sensor signal is exploitable. In the case of air quality monitoring especially regarding oxidizing gases, the sensor used is supposed to have a range of measurements from few ppb to 1 ppm.
- **distance** : it is the maximum distance where the sensor can be positioned and still give a usable signal when gas is released from the source.

The important operating parameters, which are also considered in gas sensor technology, are temperature and humidity.

1.3.2 Chemical gas sensors

A chemical gas sensor is a sensor in which the interactions between a sensitive material and gas molecules are chemical ones. Chemical interactions may take place on the surface of sensitive material or at the interface of the gas sensor structure. They produce a sensor signal, which can be represented as electrical, optical or acoustic changes [4].

Only three sorts of gas sensors using materials in solid phase lead to industrial developments [13]:

Catalytic sensors

These sensors are small calorimeters used to measure the energy released from the catalytic oxidation of reducing gas species ($Q_{reaction}$) in air at the surface of heated sensor. The example of an catalytic sensor with platinum or palladium as an catalytically active metal is presented in Figure 1.8. They are usually operated in a Wheatstone bridge arrangement with an inactive reference sensor. The sensor response may be chosen as the change in the temperature monitored by the resistance change. Those sensors need oxygen to work and they present a weak selectivity because they are sensitive to almost all of the hydrocarbon species. They are mainly used in safety control applications to detect methane.

Electrochemical sensors

These sensors are based on one or several electrodes. When there is a modification of the concentration of the active species at the surface of electrodes or at the membranes covering electrodes exposed to atmosphere, a displacement of charges and then generation of an electric field between surface and the bulk take place. Equilibrium is reached when diffusion forces, caused by species gradient become equal to electric forces [13]. The typical principle of electrochemical

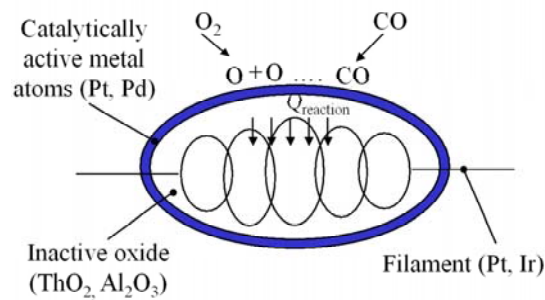


Figure 1.8: Diagram of a catalytic sensor to detect reducing gasses [4].

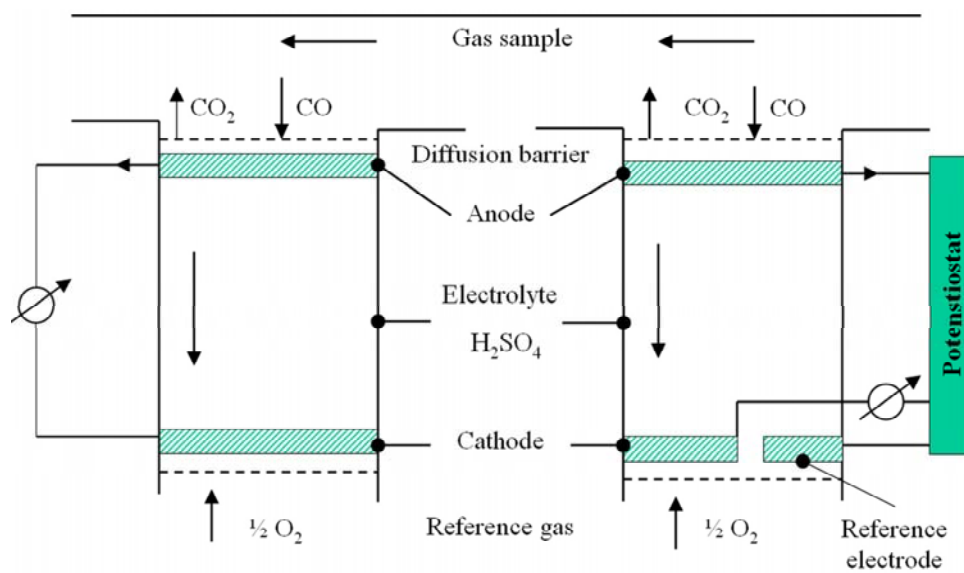


Figure 1.9: Schema of an electrochemical sensor [4].

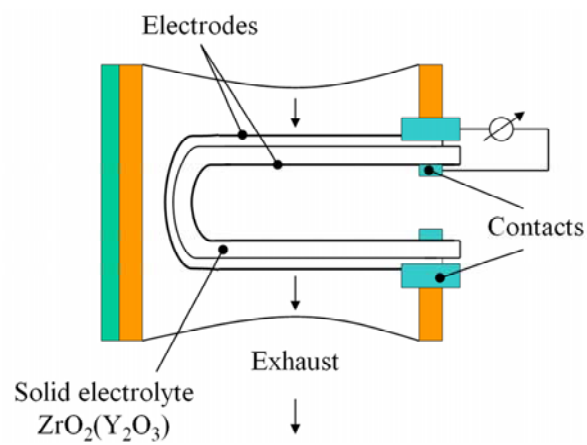


Figure 1.10: Diagram of a solid state electrolyte sensor [4].

sensor is the CO sensor with liquid electrolyte between electrodes (see Figure 1.9). It detects CO in air with two or three electrodes. Its operation is based on the electrocatalytic reaction between CO and O₂ molecules to form CO₂. The CO oxidation occurs at the anode, the O₂ reduction at the cathode. The rate-determining step in the overall reaction is controlled by the diffusion of CO molecules from the diffusion barrier to the surface of the anode where the fast oxidation of CO molecules takes place. Since the activity gradient between the diffusion barrier and the anode itself is proportional to the partial pressure of CO, the reaction rate, hence the current (sensor response), is a linear function of the CO pressure.

The other example of electrochemical sensor is gas sensors based on ZrO₂ doped with Y₂O₃ to measure the oxygen partial pressure, e.g., in a car exhaust. Figure 1.10 shows the schema of a solid state electrolyte sensor. The solid electrolyte exhibits high bulk conductivity of O₂⁻ ions. The porous platinum electrodes make possible the dissociation of molecular O₂ from the gas phase and the electron transfer between the cathode and the anode. At a constant temperature and a constant oxygen partial pressure in the reference gas (usually air), a potential is generated in the concentration gradient between the anode and the cathode. The potential is determined by the difference in chemical potentials of O₂ between the exhaust and the constant phase.

In principle, this sensor can be used for the detection of all electrochemical active species which can be oxidized or reduced at a particular potential. This potential is characteristic for a specific electrode and a chemical component.

Semiconductor sensors

The main types of semiconductor sensors - called also electronic ones - are the conductance or resistance sensors. They are used for monitoring both reducing and oxidizing gases. Materials used for electronic sensors are semiconductors (e.g., metal-oxides, molecular semiconductors, III-V semiconductors). The signal output is the electronic conductance or resistance changes, which are usually measured between ohmic contacts (see Figure 1.11). The response value is determined by competitive electronic charge transfer reaction between gas molecules or adsorbed ions and the sensitive material. As a result of this reaction, a change occurs in the electron density and, following, in the conductance or resistance of the sensitive material. The definition of an electronic sensor also includes Schottky-diode or Metal Oxide Semiconductor-diode (MOS) sensors with their capacitance as a sensor signal, which is monitored with alternating currents. The general sensor responses of these sensors may be also characterized by a change of the frequency-dependent conductance (or admittance).

The other sensor structures not industrialized yet, were also developed:

Field effect chemical sensors

These are the gas-sensitive devices typically based on Gas-FET. Monitored gases are for example H_2 , O_2 , H_2O , CO , etc. In the case of hydrogen measurements, the H atom induces modifications in the electrical double layer at Pd/SiO₂ interface which can be monitored by a drain-source current change through n-conducting channel (see Figure 1.12). The value of the drain-source current is usually adjusted at a certain level by an electrical field E . E is perpendicular to the channel, which is generated by a positive voltage at the Pd gate. Adsorption and dissociation of H_2 at the Pd surface and subsequent diffusion of H atoms to the Pd/SiO₂ interface lead to the formation of surface and interface dipoles. These dipoles modify the conductance of the n-type channel at a given voltage. For the concentration monitoring of ions or adsorbed oriented dipoles, the Ion-Sensitive Field-Effect Transistors (ISFETs) were developed. In this case, the metallic gate of Gas-FET is replaced by the liquid and a reference electrode is added.

Lately, the great interest is concentrated on nano-structures and advanced FETs for gas sensing. The most promising are based on III-V semiconductors and nitrides III-N because of such advantageous features of these materials like superb electron transport properties with high surface sensitivity, the variety of materials, the possibility to miniaturize into a chip and co-integrate with signal processing and communication circuits [47]. Figure 1.13 shows an example of a novel hydrogen and liquid-phase sensors formed on AlGa_N/Ga_N heterostructure (HFET) [18,48]. The first structure is a Schottky diode with a Pd ring and the second one is an open-gate FET.

Mass-sensitive sensors

These sensors are the quartz microbalance sensors coated with a chemically sensitive layer. They are using the surface or bulk acoustic waves (SAW or BAW) generated and detected on the piezoelectric substrate. These devices make possible a sensitive weighting of mass changes upon adsorption of particles from the gas or liquid phase. It leads to a shift of the resonance frequency. It may be monitored as a difference signal compared with a uncoated quartz. SAW and BAW devices have similar responses. The difference is in operation frequencies. SAW oscillator may be designed for 100 MHz, which is much higher than BAW frequency of about 10 MHz [13].

Figure 1.14 shows a standard design of an SAW gas sensor. This is a sensor based on the electrode configuration where one is a reference electrode and the other is generally with the sensitive material to adsorption of analysing gases between electrodes. In the case of the sensor showed in Figure 1.14 electrodes are in form of interdigital transducers (IDTs) photolithographically etched on the quartz surface. As an input signal serves the radio-frequency RF voltage. RF is

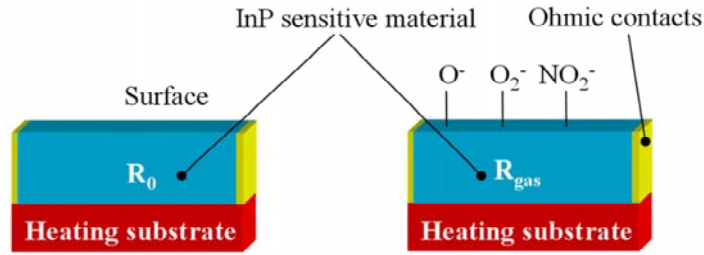


Figure 1.11: Diagram of an electronic sensor.

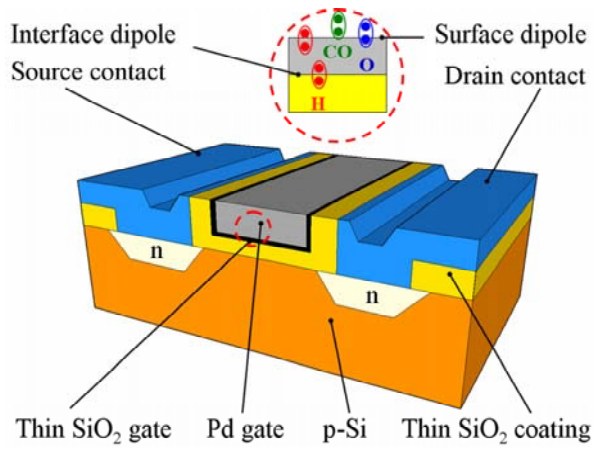


Figure 1.12: Diagram of a field effect sensor [4].

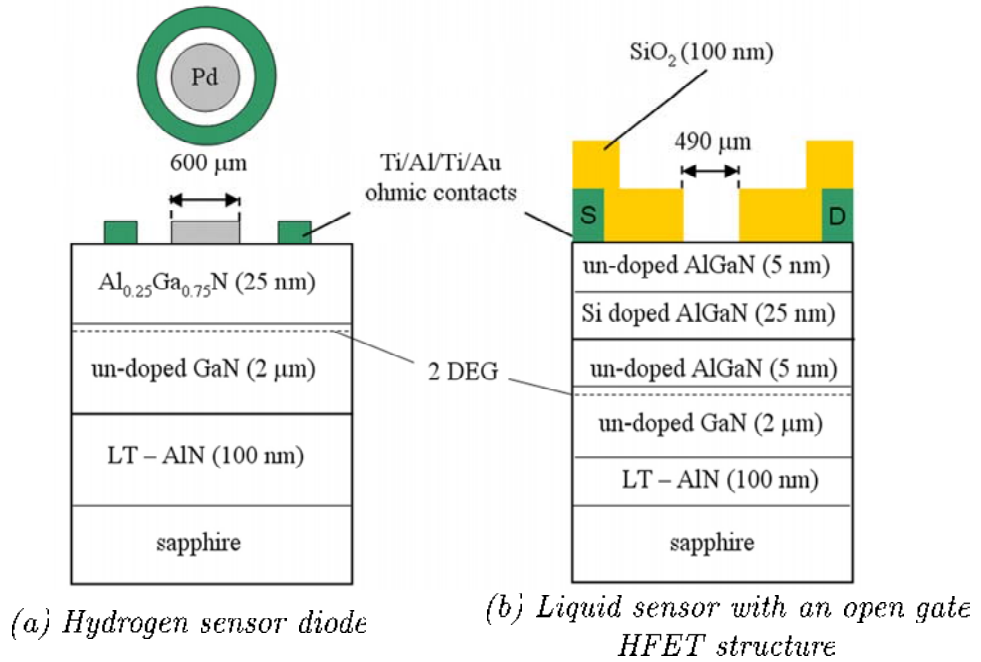


Figure 1.13: Diagram of AlGaN/GaN based sensors [18].

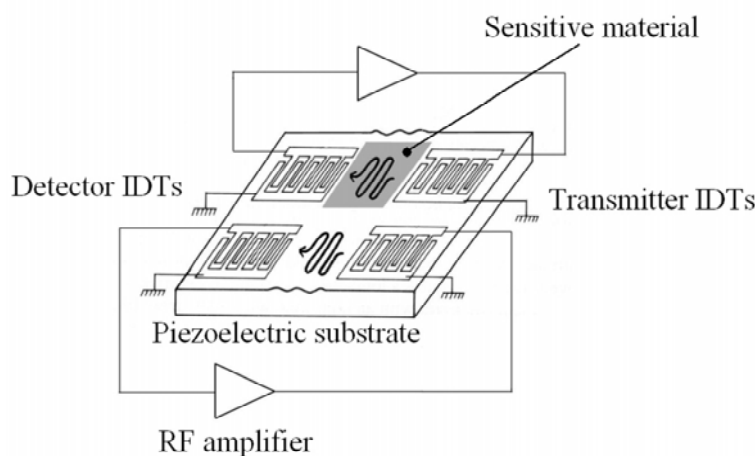


Figure 1.14: *Schema of a SAW sensor [13].*

applied across transmitter IDTs which induces deformation in the piezoelectric substrate. These deformations create the acoustic surface waves. The acoustic waves pass from transmitter to detector. When changes in mass on the sensitive material due to an adsorption phenomenon take place, the shift of SAW device resonant frequency is observed.

Optochemical sensors

These sensors are based on the spectroscopic detection of molecules by a 'fluoresensor'. Absorbed light excites molecules, which are deactivated by emission of characteristic fluorescence radiation. This radiation is monitored by a photodetector. Such sensor that embodies organic material as a sensitive part is used in detection of VOC.

1.3.3 Sensitive materials

Among the variety of materials used in chemical gas sensor technology, the best known are electrolytes and semiconductors, i.e., metal-oxides, molecular semiconductors, III-V semiconductors. In this section a short survey through these sensitive materials as well as their characteristic features is presented.

Solid state electrolytes

This group of sensitive materials may be constituted of a number of ceramic metal oxides, but the most commonly used material as a chemical gas sensor is zirconium dioxide (ZrO_2). ZrO_2 is normally an electrical insulator but when doped with traces of di- or trivalent metal oxides (Y_2O_3) and heated above 600°C , it becomes conductive due to the presence of oxygen vacancies in the

crystal lattice. In the case of NO and NO₂, the measurement range extends from 25 to 450 ppm [5].

Metal oxides

This group consists of three different types of binary oxygen compounds:

- oxides, containing oxide ions O²⁻, with which metal M form metal oxides MO;
- peroxides, containing peroxide ions O₂²⁻, which contain O–O covalent single bonds that form M₂O₂;
- superoxides, containing superoxide ions O₂⁻, which also have O–O covalent bonds but with one negative charge less than peroxide ions that form MO₂.

Nowadays, the most used metal oxides in chemical gas sensor technology are tin dioxide (SnO_{2-x}), indium oxides (In₂O₃), tungsten oxides (WO_{3-x}), titanium dioxide (TiO₂) and molybdenum oxides (MoO₃). Some parameters like the work temperature and range of measurements for chosen metal oxides, are collected in Table 1.8.

Table 1.8: *Chosen metal oxides and their sensing parameters.*

Pollutant	Semiconductor	Gas concentration range (ppm)	Working Temperature (°C)	Reference
CO	SnO ₂ doped with Pd and Pt	100	300	[10]
CO, NO ₂ , O ₃	SnO ₂	0.1 - 100	100 - 600	[49]
NO ₂ , O ₃	In ₂ O ₃ doped with Fe ₂ O ₃	0.2 - 5000	70 - 300	[7]
CO, NO ₂ , O ₃	MoO ₃ , WO ₃ , TiO ₂ and MoO ₃ -WO ₃ , MoO ₃ -TiO ₂	1 - 150	150 - 300	[5]
CO, NO ₂	MoO ₃ , TiO ₂	0.5 - 400	300	[6]
NO ₂ , O ₃	In ₂ O ₃ , In ₂ O ₃ -NiO, In ₂ O ₃ -MoO ₃	0.2 - 1	20 - 400	[8]
SO ₂	WO ₃ doped with Pd, Pt, Cu, Ag, Au, Rh	800	200 - 600	[50]

Molecular semiconductors

Among the large number of molecular semiconductors, the typical material used in sensing technology is phthalocyanine. It is a macrocyclic compound having an alternating N–C atom ring structure. This molecule is able to coordinate hydrogen and metal cations in its center. Therefore, a variety of phthalocyanine complexes exist. Some of the chosen examples and their gas sensor parameters are collected in Table 1.9.

Table 1.9: *Examples of phthalocyanines used in gas sensing technology.*

Pollutant	Semiconductor	Gas concentration range (ppm)	Working temperature (°C)	Reference
NO	NiPc	5 - 500	160	[51]
NO ₂	CuPc	10 - 100	25 - 100	[16]
NO ₂	PbPc-polypyrrole	49	100 - 170	[52]
NO	Gd(Pc) ₂	0.25 - 1	ambient	[53]
NO	CoPc	5 - 100	ambient	[15]
NO ₂ , O ₃	CuPc	atmospheric	50	[13]
O ₃	NiPc	0 - 0.3	ambient	[12]

III-V semiconductors

In this group of materials, the typical ones used in gas sensor technology are indium phosphide (InP), gallium arsenide (GaAs), gallium nitride (GaN) and related compounds. Materials may be in a form of ingots or single crystal wafers or nano-size structures [18,48]. III-V semiconductors are used as well as a sandwich structure in field effect chemical sensors and the electronic ones particularly resistive. Moreover, III-V semiconductors are excellent material candidates for high performance sensors because of their attractive features [18]:

1. superb electron transport properties with high surface sensitivity;
2. a wide variety of materials;
3. the availability of advanced nano-technology;
4. the possibility to miniaturize into a chip and co-integrate with signal processing and communication circuits.

Recently, resistive sensors based on n-type InP epitaxial layers proved great sensitivity to oxidizing gases of concentration less than 50 ppb. Because of its monocrystalline structure in comparison with metal oxides and molecular semiconductors, n-InP active layers have got well defined features like their thickness, doping level, conductivity, and carrier mobility. Additionally, the InP layer initial resistance in pure air is observed to be very stable in time. Moreover, sensors work at temperature less than 100 °C and are characterized by a fast response time for air quality monitoring [14,15,20,21,22]. However, many important problems, like the electronic properties of surface states and their role in charge carrier transport in thin InP films as well as mechanism of surface Fermi level pinning and its impact on gas sensing parameters are still under debate.

1.3.4 Advantages and disadvantages

In conclusion, advantages and disadvantages of different sensitive materials used as chemical sensors for pollutant detection and measurements, including the major pollutants like O_3 and NO_2 are collected in Table 1.10. From all the materials presented, the sensors based on the InP and phthalocyanine seem to have the best characteristics in air quality applications, firstly because of working temperature, secondly because of the detected gas concentration range. It has to be noted here that the materials like SnO_2 , SiO_2 , Al_2O_3 are often used as gas sensors with added metal at the surface, that is needed to stabilize sensor signal. The metal–semiconductor gas sensor structure is very interesting because of the ionic properties of the semiconductor material (interface potential barrier strongly depends on the metal electronic work function [49]). The coefficient S of these materials goes to 1, S represents the difference of the electronegativity between cations and anions contained in the semiconductor [50]. The coefficient S of InP goes to 0.3 (it means that the potential barrier is rather not dependent on the metal electronic work function) [50], however, the use of simple resistive InP gas sensor shows its great sensitivity to very low NO_2 concentrations [20, 21,22]. Thus, in spite of existence of native oxide layer that causes the great density of surface states and Fermi level pinning and is responsible for small coefficient S , the InP resistive sensors are very sensitive and their sensor signal is very stable in the time.

Moreover, the great advantage of InP over the phthalocyanine and the other material is a possibility to on-chip miniaturization and co-integration with signal processing and communication circuits. This is why the main aim of this Thesis is a thorough characterization of the sensing, electronic and chemical properties of the gas sensor based on n-InP epitaxial layers.

Table 1.10: *Characteristic features of sensitive materials.*

Material	Gas	Gas concentration range (ppb)	Work temperature (°C)
Solid state electrolytes	NO_x	250 - 450	600
Metal oxides (SnO_2)	NO_x , O_3	> 100	> 100
Molecular semiconductors (CuPc)	NO_x , O_3	0 - 300	50
III-V semiconductors (InP)	NO_x , O_3	> 20	80

In conclusion, the variety of pollutants, their impacts on human health and environment as well as their characteristics are presented. Moreover, different

methods of their monitoring and detection are shown and compared. From this comparison, the chemical sensor based on III-V compounds seems to be satisfying for detection of atmospheric pollutants. Thus, in the next Chapter, the electronic properties of III-V semiconductor surface and surface phenomena, particularly for InP will be shown. A survey through the InP-related native oxides and adsorption process will be also presented. In addition, the ohmic contacts to a semiconductor and technological aspects of their realization will be discussed.

Chapter 2

General properties of semiconductor surfaces

The knowledge of physical and chemical status of the semiconductor surface and near-surface region is necessary for understanding the electronic phenomena in microelectronic structures. Particularly, in the case of devices based on thin and nano-layers the near-surface region strongly determines the performance of those devices leading to their instability, leakage currents and surface Fermi level pinning [28,29,30,37].

One of the important surfaces for technology of modern devices, including gas sensors, is a free surface of semiconducting compounds, such as gallium arsenide, indium phosphide and their ternary and quaternary alloys, which is covered by native oxides. The oxide layer is responsible for the high density of interface states and, therefore, completely changes the characteristics of the near-surface region in comparison with those in the bulk [57,58]. Generally, a native oxide layer is produced during exposure of the freshly processed surface to ambient conditions. After removal of the native oxide and exposition to air, these surfaces exhibit a very fast re-growth of native oxide layer [59]. Therefore, the characterization of native surfaces is particularly important to understand the sensing mechanism in III-V compound based gas sensor devices since the gas action takes place firstly on the surface. In this context, the studies of the surface state density distribution in the energy bandgap as well as their chemical and structural origin is of great importance.

2.1 Semiconductor surface

A semiconductor surface is the boundary between periodical distribution of the potential in the solid bulk and non-periodical distribution of the potential in solid environment. I.E. Tamm and W. Shockley [57,56,60] proved that the termination of a periodical one-dimensional potential at the semiconductor sur-

face gives rise to a new type of energy states. These states are described by a wave function with the maximum of probability density at the surface and decaying in the solid bulk.

In order to achieve the minimum surface free energy condition and taking into account the existing environment among solids (gas pressure, temperature), two processes can appear at the surface. On one hand, the surface reconstruction is when surface atoms or molecules change their position and the surface atom configuration is completely different from that in the bulk. On the other hand, physical or chemical adsorption processes may appear. The surface reconstruction and adsorption processes lead to a change of periodical distribution of the potential by appearance of vacancies and stresses. In consequence, in the surface reconstruction case the intrinsic surface states are created and the non-intrinsic surface states in the case of adsorption [56,60].

It should be stressed that the surface states cause usually many undesirable effects in the technology of semiconductor devices as surface recombination of charge carriers, reduction of luminescence efficiency, electrical breakdown and Fermi level pinning. Furthermore, surface states play the main role in the gas sensing process which starts at the semiconductor surface.

Table 2.1: *Charge of surface states [61].*

Kind of state	Empty state	Occupied state
Acceptor-like	0	-
Donor-like	+	0

Considering the charge feature of different surface states, one can classify them in two groups: anti-bonding acceptor-like states and bonding donor-like states. As it is shown in Table 2.1, the acceptor-like surface state is neutral if empty and negatively charged if occupied. The behaviour of the donor-like state case is different; it is positively charged if empty and neutral if occupied. It should be mentioned that states derived from the conduction band can be treated like acceptor-like states, and states from the valence band like donor-like ones [61].

The development of the theory of surface states connected with experimental results of adsorption in controlled conditions allows to understand the relationship between surface phenomena and the surface band bending as well as creation of the surface space charge Q_{sc} (see Figure 2.1 where E_D represents the energy location of bulk donors). The existence of surface states creates an electric field E . This field shifts all bulk energy levels with respect to the surface, resulting in the surface band bending that is equal to $q \cdot V_s$ where q is the absolute value of the elementary charge and V_s is the surface potential. In the case of an n-type semiconductor the assumed acceptor-like surface states give

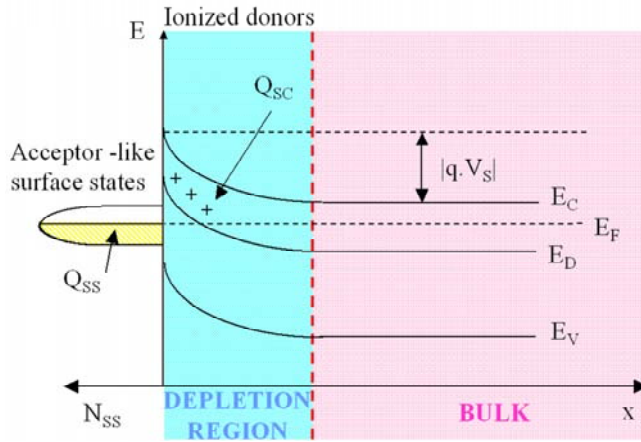


Figure 2.1: Energy schema of a near surface region in n-type semiconductor with acceptor-like surface states; Q_{ss} - charge in surface states, Q_{sc} - surface space charge [61].

rise to the negative charge transfer from the semiconductor bulk to the surface states, which become ionised negatively (see Figure 2.1).

According to the charge neutrality rule in a semiconductor under thermal equilibrium, the negative charge in surface states Q_{ss} is balanced by the positive surface space charge in the near-surface region Q_{sc} . As a result, the near-region surface exhibits a different concentration of free carriers than that in the bulk. In the case where the concentration of majority Q_{sc} carriers is lower than the bulk one, the space charge region is called a depletion layer. In the situation where the surface band bending is so large that for n-type semiconductor, the hole concentration near the surface is larger than the electron bulk one, such a region is called an inverted layer [60]. When surface states are donor-like and lie above the Fermi level energy, electrons tend to leave them and the surface becomes positively charged. In the surface-space charge region, the major carrier concentration is larger than in the bulk and this region is called an accumulation layer. It should be stressed that an introduction of acceptor-like states above E_F or donor-like states below E_F does not cause creation of a band bending.

In the case of the semi-infinite (one-dimensional analysis) non-degenerated n-type semiconductor under thermal equilibrium with all impurities ionised and intrinsic carriers neglected, the profile of electric potential $V(x)$ can be calculated analytically from the Poisson's equation [58,60]:

$$\frac{d^2 V(x)}{dx^2} = \frac{-\rho_q(x)}{\varepsilon \cdot \varepsilon_0} \quad (2.1)$$

where:

- $\rho_q(x)$ is the space charge density;

- ε and ε_0 are the relative permittivity of the semiconductor and the permittivity of free space, respectively.

The charge density $\rho_q(x)$ is determined by the Boltzmann distribution [56, 57, 60, 58], and is expressed by the following relationship:

$$\rho_q(x) = -q \cdot n_b \cdot \left[\exp\left(-\frac{q \cdot V(x)}{k \cdot T}\right) - 1 \right] + q \cdot p_b \cdot \left[\exp\left(-\frac{q \cdot V(x)}{k \cdot T}\right) - 1 \right] \quad (2.2)$$

where n_b and p_b are the bulk concentrations of free electrons and holes, respectively.

For the low values of the surface band bending:

$$q \cdot V_s \ll k \cdot T \quad (2.3)$$

and for:

$$Z = \frac{q \cdot V}{k \cdot T} \quad (2.4)$$

the linear approximation:

$$\exp(Z) \approx 1 + Z \quad (2.5)$$

can be used for determination of the profile of the electric potential $V(x)$:

$$V(x) = V_s \cdot \exp\left(-\frac{Z}{L}\right) \quad (2.6)$$

where the effective Debye length L is a characteristic parameter of the electric field decay and expressed by the relationship:

$$L = \sqrt{\frac{\varepsilon \cdot \varepsilon_0 \cdot k \cdot T}{q^2 \cdot (n_b + p_b)}} \quad (2.7)$$

The high surface potential is better approximated by the parabolic dependence of x :

$$V(x) = \frac{k \cdot T}{2 \cdot q \cdot L^2} \cdot (x - W)^2 \quad \forall x < W \quad (2.8)$$

and

$$V(x) = 0 \quad \forall x > W \quad (2.9)$$

W is called a depletion or accumulation layer width (also depletion or accumulation width) and is equal to:

$$W = \sqrt{\frac{2 \cdot \varepsilon \cdot \varepsilon_0 \cdot V_s}{q \cdot (n_b + p_b)}} \quad (2.10)$$

The plane at the depth $x = L$ or at $x = W$ from the surface, can be considered as a boundary between the near-surface region and the bulk [61, 60].

2.2 Models of surface states

The key problem of present approaches in modelling of the semiconductor surfaces and interfaces is to develop the model of surface states which supposes to fulfil physicochemical, measurement and technological aspects. The physicochemical aspect is taking into account the physical and chemical nature of surface/interface states (like existence of the native oxide layer). The measurement aspect is a prediction of the surface/interface state density distribution shape and an explanation of measurement results of static and dynamic features of surface states in a consistent way. As for the technological aspect, it is an indication of the best suitable technological process used, e.g., in passivation of the semiconductor surface.

Extensive studies of III-V semiconductor surfaces and interfaces have shown that the Fermi level is already pinned at free surface (vacuum semiconductor or V-S) as well as at insulator-semiconductor (I-S) interfaces and unoptimized semiconductor-semiconductor (S-S) interfaces. In addition, the strong correlation between the semiconductor substrate and the energy position of pinning was revealed [37,28]. The Fermi level pinning is usually understood as an impossibility to move the surface Fermi level E_{F_s} beyond a narrow energy interval, even by applying to the surface an external electric field. A well-known example is a so-called midgap pinning at clean molecular beam epitaxy (MBE) surface. The mid-gap pinning is as well observed at air exposed surfaces, I-S and regrown S-S interfaces of GaAs. In spite of a long history of research, the main mechanism of the Fermi-level pinning at III-V semiconductor-based surface/interfaces has not been well established so far.

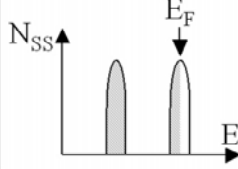
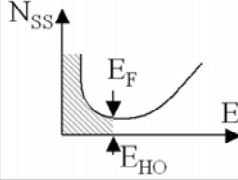
Thus, the surface state distribution model supposes to fulfil all the aspects previously explained and to include the Fermi level pinning phenomenon. There exists two main models of surface states fulfilling those conditions. They are:

- the unified defect model (UDM) proposed by W. E. Spicer et al. [62,63];
- the disorder induced gap state (DIGS) model by H. Hasegawa and H. Ohno [37].

In Table 2.2, basic ideas and a short comparison of main features of discussed models are presented. As for the E_F pinning, on one hand according to the UDM, E_F position at the semiconductor interface is determined by the energy of the acceptor-type discrete deep level, in the case of n-type materials. On the other hand, in DIGS model, E_F is pinned at the so-called charge neutrality energy level [37].

The UDM is mainly applied for the interpretation of surface electronic phenomena at III-V (100) atomically clean surfaces with an oxygen or metal atom

Table 2.2: Major models of interface states at III-V surfaces and interfaces [37].

Models	Origin of pinning states	N_{SS} distribution and E_F pinning
UDM	Deep levels related to non-stoichiometry	
DIGS	Loss of 2D periodicity at interface	

layer, in the range of coverage from the small fraction of one monolayer to very thick overlayers [62]. However, the discrete distribution of surface states related to missing atoms giving rise to surface defects [62,63,64], as proposed in the UDM, are based mainly on indirect conclusions from XPS and UPS (X-ray and Ultraviolet Photoemission Spectroscopy). It should be stressed here that either standard XPS or UPS are not particularly sensitive to band gap states. Moreover, in the literature, there is no general agreement about the nature and charge behaviour of surface defects [38,62,63,64]. Also, there is no direct evidence of the existence of sharp discrete levels in the band gap. In contrary to UDM model, the U-shaped continuous distribution of surface states with the well developed minimum near the midgap was experimentally obtained by R.M. Feenstra [65,66] at the clean and metal covered GaAs (110) surfaces from the Scanning Tunneling Microscopy.

The minimum in the surface state density distribution, corresponding to a Fermi level position has the physical meaning. It is the charge neutrality energy level E_{HO} , which is a characteristic value of a given semiconductor because this quantity corresponds to the average hybrid orbital energy for sp^3 hybrid bonding [37,38,39,40,28,67,68]. The location of the E_{HO} level for indium phosphide with respect to the conduction band minimum is equal to -0.37 eV [37]. The value of E_{HO} can have slightly different values, depending on the experimental method.

Figure 2.2 shows the basic postulate of the DIGS model. It is the existence of a disordered quasi-amorphous layer in the semiconductor near the interface, build up by a formation of V-S, I-S and unoptimized S-S interfaces. The disordered quasi-amorphous layer is caused by different bonding configurations on each side of the interface (see Figure 2.3). These states are tail states analog-

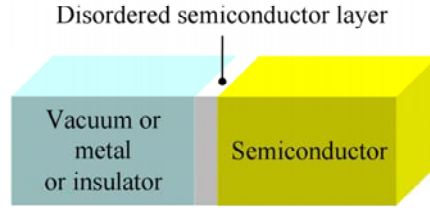


Figure 2.2: *Schema of the semiconductor interface corresponding to the DIGS model [37].*

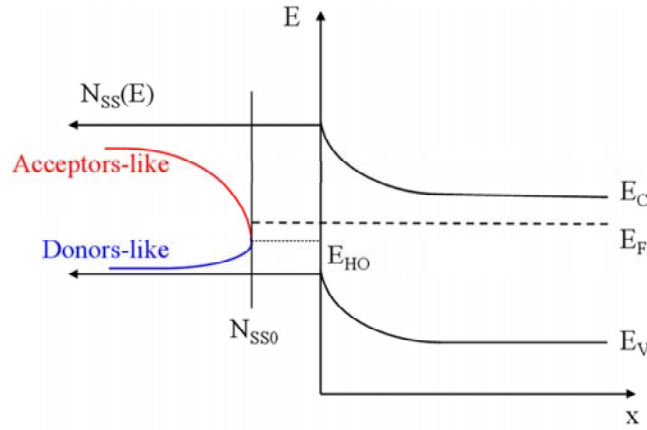


Figure 2.3: *U-shaped interface state distribution with characteristic E_{HO} according to DIGS model [29].*

ically like in amorphous semiconductors. Thus, their density is high at band-edges and decreases toward the midgap. States originating from the conduction band are anti-bonding (acceptor-like) ones (Eq. 2.11), whereas the states arising from the valence band are bonding (donor-like) ones (Eq. 2.12). Their density minimum in the energy gap falls at E_{HO} . For simplification and analytical description of the state density distribution, acceptor-like states below E_{HO} and donor-like states above E_{HO} may be neglected. Then, as it is shown in Figure 2.3, the E_{HO} energy separates two types of states in the energy gap [29,30]. The $N_{ss}(E)$ distribution is given by following expressions:

$$N_{ss}(E) = N_{ssc} \cdot \exp \left[\left(\frac{|E - E_{HO}|}{E_{0d}} \right)^{n_d} \right] \quad \forall E < E_{HO} \quad (2.11)$$

$$N_{ss}(E) = N_{ssc} \cdot \exp \left[\left(\frac{|E - E_{HO}|}{E_{0a}} \right)^{n_a} \right] \quad \forall E > E_{HO} \quad (2.12)$$

where (E_{0d}, n_d) and (E_{0a}, n_a) describe the curvature of donor-like and acceptor-like state density distribution, respectively [29,61].

The density of surface state distribution is measured by means of the Scanning Tunneling Spectroscopy (STS) or by C-V techniques for MIS structures

or by photoluminescence surface state spectroscopy (PLS³)[37,69]. The principle of the PLS³ is well described by T. Sawada et al. [69]. Generally, when a semiconductor surface is illuminated by excitation light, electron-hole pairs are generated. Then, they may migrate and eventually recombine through various recombination processes. Among these processes, the surface recombination process is greatly affected by band bending at the semiconductor surface. Then the measured photoluminescence efficiency versus excitation is compared with a theoretical one obtained from a rigorous computer simulation taking into account of all possible recombination processes, and finally $N_{SS}(E)$ distribution is obtained.

As it is previously written, the knowledge about the origin of surface states based on experimental data allows for the technology optimization. It is particularly important in the choice among passivation processes because of the minimum surface state density N_{SSc} changes as a function of the surface treatment, being $2 \cdot 10^{11} \text{ cm}^{-2} \text{ eV}^{-1}$ for chemically etched and $10^{12} \text{ cm}^{-2} \text{ eV}^{-1}$ for as-received wafers, these values are obtained by PLS³ method [37,69]. Thus, H. Hasegawa et al. [18,70] proposed, on the base of the DIGS model, one of the most efficient and sophisticated passivation approach for III-V surfaces using an ultra-thin silicon interface control layer (ICL). This layer should be inserted between the III-V based semiconductor and the insulator (or vacuum) to create a smooth structural transition at the interface, as it is shown in Fig 2.2.

2.3 Properties of InP surfaces

Indium phosphide crystallizes in zinc-blende structure, with a band-gap of 1.35 eV. The distance between the vacuum level and the valence band edge at the surface is about 5.75 eV. For n-type semiconductors, surface states lead to band bending in the surface region and a depletion layer is created [59].

The free InP surface after exposure to air atmosphere is totally covered by native-oxide layer, which is difficult to remove and has got a strong influence on electronic properties of the InP near-surface region. Thus, a wide range of surface sensitive spectroscopic techniques has previously been used to study indium phosphide surface both (100) and (110) with their native oxide layer. The main used techniques are Raman Spectroscopy, Low Electron Energy Diffraction (LEED), Auger Electron Spectroscopy (AES), Ultraviolet Photoelectron Spectroscopy (UPS), Electron Energy Loss Spectroscopy (ELS), X-ray Spectroscopy (XPS) and Angle-Resolved X-ray induced Photoelectron Spectroscopy (ARXPS) [59,71,72,73,74,75,76,77,78,79].

2.3.1 Native oxides

Possible chemical compounds created on the basis of indium-phosphorus-oxygen (In-P-O) system are In, InP, P, P_2O_3 , P_2O_5 , $In(PO_3)_3$, $InPO_4$ and In_2O_3 . The melting point values of these compounds are collected in Table 2.3. It should be noted that instead of P_2O_3 , they are very stable at high temperatures. G.P. Schwartz et al. have deduced from the phase diagram that $InPO_4$ is the only product resulting from the reaction between InP and O at equilibrium [76].

Table 2.3: *Melting points of In-P-O compounds [76].*

In-P-O Compound	P_2O_3	P_2O_3	$InPO_4$	$In(PO_3)_3$	P_2O_5	In_2O_3
Melting point (°C)	23.8	>173	>900	750	563	≈2000

According to J.F. Wager et al. [77], the InP (100) surface in ambient air and at ambient temperature is covered with native oxide layer. It consists predominantly of In-O compounds, tentatively identified as In_2O_3 with small amounts of P-O compounds, such as $InPO_4$. After reevaluated data [78], the oxide layer was identified as two different layers, the $InPO_4$ layer as a covering InP surface and In_2O_3 as an outer layer. These results were verified by A. Guivarc'h et al. [71], who studied electrical properties of InP anodic oxides. They estimated two separate regions of InP oxides. The first region was suggested to be an island structure with thickness ranging from 0.4 to 0.7 nm. The characterisation by XPS of this region showed that the surface peak was only due to In. The second region was presented rather as a continuous oxide layer with a thickness from 1 to 3 nm. The thickness estimated from 1 to 1.5 nm was a thickness where islands begin to coalesce into a continuous film.

2.3.2 Electronic properties of native oxides

J.F. Wager et al. [77,78] have investigated the chemistry and physics of the native oxide formation on InP, trying to correlate them with electrical instabilities in MIS, MOS and MISFET structures based on InP. From XPS, UPS and ELS data, they estimated the band gap of $InPO_4$. On the other hand, the band bending of In_2O_3 is well known from literature [8]. So, the energy diagram with the assumption that the InP surface is totally covered by alternate native oxide layer was obtained (see Figure 2.4). UPS studies were done for an $InPO_4$ sample with a thickness of 5.5 nm. It means that the presented band diagram in 2.4 represents the bulk oxides. In the case of very thin oxide layer the existence of traps and defects in the oxides is not negligible.

According to G. Hollinger et al. [72,73], below 350 °C the oxide layer is generally non-crystalline consisting of In, P and O. Thermal oxides at temperature between 300 and 450 °C were identified as an oxide mixture of In_2O_3 and $InPO_4$. These oxides were studied by means of C-V characteristics that strongly

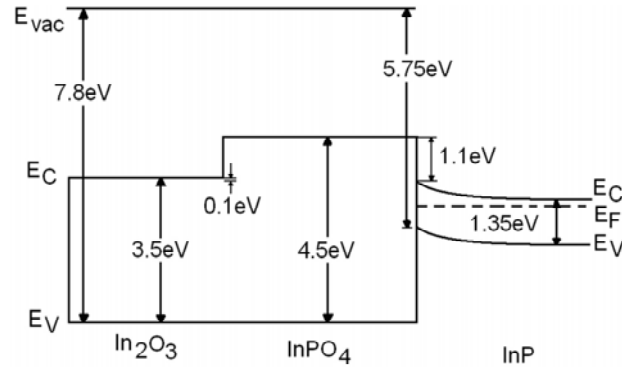


Figure 2.4: Schematic energy band representation of *InP* surface and related oxides [77].

depend on the indium or phosphorus-rich outer layer. If the outer layer was characterized as In-rich, C-V characteristics exhibited a very large counterclockwise hysteresis loop and strong frequency dispersion. It may indicate a strong pinning of the surface Fermi-level where the space charge region is in a depletion regime. It is possibly due to charge exchange between the semiconductor and traps located in the indium rich layer or to a negative fixed charge located in that region. Removal of the outer In-rich layer results in a dramatic improvement of electrical characteristics of MIS devices. No frequency dispersion is observable, neither in the depletion regime, nor in the accumulation regime that was readily reached. The P-rich inner layer probably allows for charge exchanges between the In-rich outer layer and the semiconductor. It seems to be a very good passivating layer because after removal of the outer In-rich layer an extremely small charge injection-like hysteresis can be noticed.

2.3.3 Chemical properties of native oxides

Indium in InPO₄ is coordinated to six oxygen atoms, each of them being the corner of a different PO₄ tetrahedron. Four of six oxygen atoms are associated with two indium atoms and one phosphorus, whereas two are associated only with one indium and one phosphorus. The InPO₄ as well as InPO₃ is a well insulator with the band gap more than 5.5 eV for InPO₃ and 4.5 eV for InPO₄. They are chemically stable. InPO₃ can be described as infinite chains of PO₄ tetrahedra interconnected by InO₆ octahedra. This suggests a rather rigid network and the existence of possible intrinsic defects at the oxide-InP interface, however no extensive work is presented on bulk InP_xO_y glasses. In such glasses, the existence of finite PO₄ chains or three bridging oxygen per PO₄ like in P₂O₅ (two in In(PO₃)₃) could vary in the composition. Figure 2.5 illustrates the local atomic order in crystalline InPO₄, In(PO₃)₃ and P₂O₅.

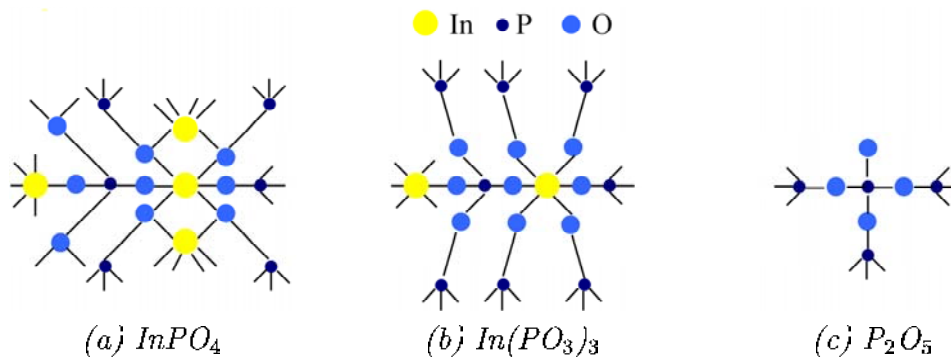


Figure 2.5: Local bonds in bulk crystalline InPO_4 , $\text{In}(\text{PO}_3)_3$ and P_2O_5 [73].

2.3.4 Native oxide formation

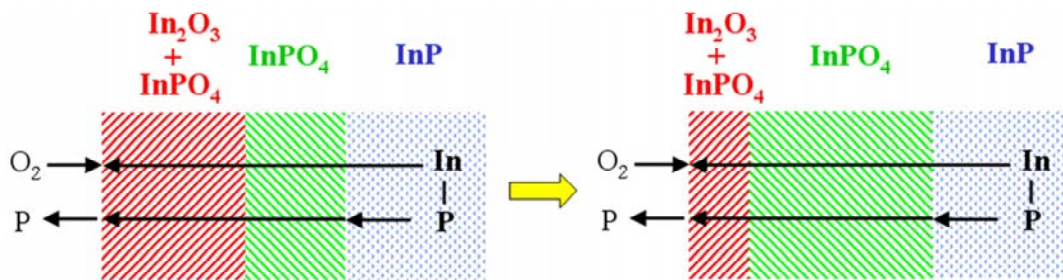


Figure 2.6: Growth model for thermal oxides of InP with $T < 600\text{ }^\circ\text{C}$ [74].

From literature [72,73,77,78], the reaction of the fresh InP surface with oxygen leads to loss of phosphorus and the formation of an oxide layer near the surface. The oxide layer thickness reaches up to 5 nm depending on the InP sample surface and ambient conditions. The behaviour of oxygen on the surface seems to be much more typical of a slow oxidation process in which oxygen species penetrate the bulk, rather than simple adsorption.

A. Nelson et al., inspired by previous works, has presented the model of the thermal oxide growth on InP [74]. In Figure 2.6, it is shown that all the phosphorus in the bulk of the oxide layer is bonded as a phosphate, probably InPO_4 independently of the rise of the temperature. With temperature increasing, but still under $600\text{ }^\circ\text{C}$, elemental phosphorous collects at the interface of In_2O_3 and InPO_4 . The outer oxide layer becomes a mixture of In_2O_3 and InPO_4 . They suggested that at temperature under $600\text{ }^\circ\text{C}$, the InPO_4 inner layer acts as a diffusion barrier for phosphorus. It does diffuse to the surface combining with In and O to form the equilibrium product InPO_4 (some of it may evaporate). However, in the same time, In also reaches the surface and therefore In_2O_3 formation also takes place. As mentioned before, InPO_4 is stable up to $900\text{ }^\circ\text{C}$ while In_2O_3 is stable to near $2000\text{ }^\circ\text{C}$. However, below $500\text{ }^\circ\text{C}$ no evidence for

crystalline In_2O_3 was found. The creation of cones or islands consisted of In is not neglected.

2.3.5 InP annealed surface

Annealing is one of the main techniques used to improve characteristics of electrical contacts on the InP surface. Thus, J. Zemek et al. [79] used the ARXPS to determine non-destructive concentration depth profiles for as grown and annealed oxides on (100) InP surfaces. The thickness of native oxides was estimated to 1.4 nm. Moreover, they remarked that this value changes very little with annealing up to 300 °C. Depth profiles calculated for samples annealed at 250 °C indicate rearrangement in favour of the phosphate(s). Annealing at temperature of 300 °C and higher caused a gradual decomposition of the phosphate(s) leaving carbon contaminations and traces of indium oxides on the surface. It should be mentioned that the studied InP surfaces were oxidized in the laboratory conditions and thus, the oxide layer thickness is expected to be smaller than the oxide layer thickness of samples used in real experimental conditions.

2.4 Adsorption in general

Usually, the gas molecule interaction with the semiconductor firstly takes place on the semiconductor surface. Thus, one of the most important issues determining control of the surface technology, in particular for gas sensors, is to understand the gas interaction with the semiconductor surface. The interaction between a gas molecule and a semiconductor surface is the adsorption process.

The adsorption involves the preferential partitioning of substances from the gaseous or liquid phase onto the surface of a semiconductor. Some of the partitioned molecules are bonded at the surface active site. The origin and nature of this active site depend on the energy released during the adsorption process:

- in the range from 0.1 to 0.25 eV the interaction is defined as **physisorption**;
- if the energy is superior to 0.25 eV, the creation of a chemical bonding is possible and the process is called **chemisorption** [60].

The created bonding can be of two types. The valence type is in the case of common pair of valence electrons and the ion one in the case when a molecule becomes a cation or an anion.

2.4.1 Physisorption

The physisorption is a reversible process characterized by a low temperature where no charge transfer between a particle and a solid surface is observed. It is described by the weak Van der Waals interaction between a particle and a substrate surface similar to intermolecular forces between two molecules observed in non-ideal gases [60,80,81] (see Figure 2.7, where E_P is the potential energy of molecules). The desorption energy is equal to the adsorption one (from 0.1 to 0.25 eV).

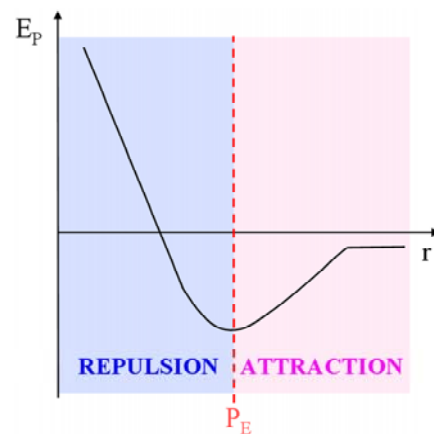


Figure 2.7: *Van der Waals interaction [60].*

Due to the non-directional character of Van der Waals interaction, the most stable configuration in solid phases is the one in which atoms are at the equilibrium distance between attractive and repulsive forces. It is the equilibrium point P_E . For a distance between interacting particles such as $r > P_E$ attractive forces are preponderant and at very short distance ($r < P_E$) repulsive forces are preponderant.

Weak low-temperature intermolecular forces produce only slight changes in the electronic structure upon molecular adsorption. In addition, molecules retain their individuality.

2.4.2 Chemisorption

The chemisorption process is characterized by a high temperature, the irreversibility and the charge transfer between a molecule and a solid. In general, it is a creation at high temperature of selective chemical bondings between an adsorbed particle and a surface atom, which leads to very specific changes in a variety of sensor responses such as their optical or electrical parameters. The simplest case of electronically conducting sensors is a charge transfer from the particle to the sensor or vice-versa [81]. As it is shown in

Figure 2.8, chemisorption is a two state process. In the first state, the distance r between the molecule and the semiconductor surface is equal to P_E . This is termed the precursor state; it is nothing more than physisorption process and it is still reversible. Then, when the molecule is closer and closer to the surface and the creation of chemical bonding has started, the process changes from reversible to irreversible. The second state is called the chemisorption state and the adsorption energy is called chemisorption one E_{CH} .

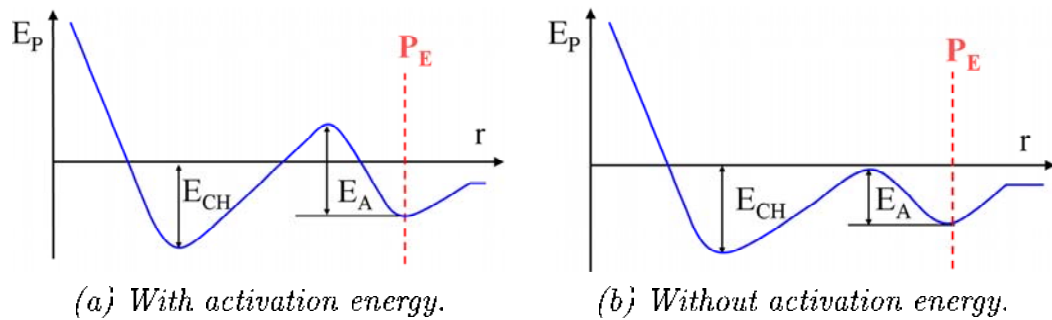


Figure 2.8: Schematic presentation of two chemisorption types [81].

In Figure 2.8, models of two different types of chemisorption are distinguished. These models were proposed by J.E. Lennard-Jones [82]. The first one is the chemisorption process with an activation energy E_A , while the second one is without activation energy.

2.4.3 Adsorption isotherms

Adsorption process can be considered in terms of two models: Langmuir and Freundlich isotherms, which are the trial approaches to the reality [83].

Langmuir isotherm

It is the first theoretical model of adsorption proposed by I. Langmuir in 1918 [84]. This isotherm was proposed with the following assumptions:

- the number of active sites at the solid surface is proportional to the surface area;
- one active site can adsorb only one molecule;
- the molecule from one active site cannot move to another active site;
- the distribution of active sites is at uniform rate;
- the bonding between the solid surface and molecule can have a physical or a chemical nature;

- the adsorption rate is equal to the desorption one.

The Langmuir isotherm is expressed by the relationship:

$$\Gamma = \frac{\Gamma_t \cdot P}{P + b^{-1}} \quad (2.13)$$

where:

- Γ and Γ_t are concentrations of adsorbate and active sites, respectively;
- P is the pressure;
- b is the constant given by the following equation:

$$b = \frac{k_2}{k_1} = B \cdot \exp\left(\frac{E_{ads}}{k \cdot T}\right) \quad (2.14)$$

where:

- k_1 and k_2 are coefficients of desorption and adsorption velocity, respectively;
- B is a constant;
- k is the Boltzmann constant;
- T is the temperature.

The adsorption of gas at the solid surface can be also described in terms of the degree of coverage θ . θ is defined as the ratio of the surface concentration of adsorbate Γ and the concentration of active sites Γ_t :

$$\theta = \frac{\Gamma}{\Gamma_t} \quad (2.15)$$

Freundlich isotherm

Freundlich isotherm is an empirical relation between the degree of coverage θ and the gas concentration that surrounds the solid surface C . This law is used practically for a theoretical analysis of gas action at semiconductor surfaces because in contrary to Langmuir adsorption, H. Freundlich assumed that the distribution of active sites is not uniform and active sites are not equivalent [85]. These assumptions make this law more realistic than Langmuir's one. The Freundlich isotherm is expressed as follows:

$$\theta = p \cdot C^m \quad (2.16)$$

where θ is the degree of coverage, p and m are characteristic constants for the discussed molecule/surface system. Parameters p and m are determined experimentally.

2.4.4 Adsorption on the semiconductor surface

The adsorption process leads to the change in the electronic response of a semiconductor, i.e., the electrical potential or conductivity/resistivity. In the case of a resistive semiconductor sensor, the measured conductance of the sample, usually between ohmic contacts, is the sum of the conductance in the bulk (G_{bulk}) and the conductance of the depletion layer ($G_{near-surface}$) [60]:

$$G_{sample} = G_{bulk} + G_{near-surface} \quad (2.17)$$

Assuming the existence of surface states, concentrations of electrons n and holes p will change from the surface to the bulk. So, the concentrations of n and p will be strongly dependent on the coordinate axis x and will change from the concentration in the space charge region Q_{sc} to the concentration in the bulk (see Figure 2.3). Thus, one can assume that the conductivity of the sample is a x -function $\sigma(x)$. Thus, σ is related to the charge carrier concentration profiles $n(x)$ and $p(x)$ and given by the following expression:

$$\sigma(x) = q \cdot (\mu_n \cdot n(x) + \mu_p \cdot p(x)) \quad (2.18)$$

In conclusion, the sample conductance G is given by the following integral:

$$G_{sample} = \int_0^d \frac{\sigma(x) \cdot c}{a} dx = \frac{q \cdot c}{a} \cdot \int_0^d (\mu_n \cdot n(x) + \mu_p \cdot p(x)) dx \quad (2.19)$$

where the following constants are as shown in Figure 2.9 and represent:

- d is the electronic active layer thickness;
- a is the distance between contacts;
- c is one of the device dimensions.

G of the sample is measured in siemens, however in most of the electrical sensor devices, measured changes are of the resistance R in ohms. The relation between G and R is as follows:

$$G = \frac{1}{R} \quad (2.20)$$

The chemical and physical adsorption on the surface depends not only on external parameters like pressure and temperature, but also on the electronic state of the surface. Moreover, from Equations 2.18, 2.19 and 2.20, the change in sample resistance due to adsorption will take place in the near-surface region, consequently in Q_{sc} charge.

The Q_{sc} charge is equal to the opposite sign charge located at the semiconductor surface. It depends on the concentration of adsorbed gas ions. Thus, the

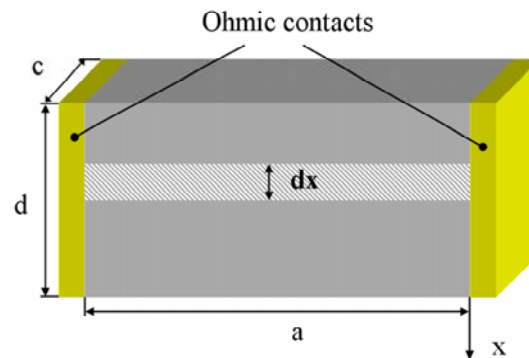


Figure 2.9: *Schema of a semiconductor sample with ohmic contacts.*

concentration of Q_{sc} should be a function of the gas pressure [86,87] and it will be some function of the gas pressure P :

$$Q_{sc} = -(Q_{sc} + q \cdot N_s(P)) \quad (2.21)$$

where $N_s(P)$ is the concentration of the adsorbed atoms on the surface and Q_{sc} is the charge density on the surface in the absence of adsorption.

2.5 Ohmic contacts

In the case of a resistive sensor device, the electronic signal is the sensor resistance. It is measured by means of low resistance contacts, usually ohmic ones. An ohmic contact is a region on the semiconductor device where the current-voltage characteristic curve is linear and symmetric [41]. Thus, the fabrication of high quality low-resistance and stable contacts is critical for the performance and reliability of the sensor device. Since a native oxide rapidly forms on the III-V semiconductor surface, the performance of a contact depends strongly on the way it has been realized.

2.5.1 Ohmic contact model

Ohmic contacts are realized by a noble metal deposition on the semiconductor surface. Metals and semiconductors differ in their work function φ_m and φ_s respectively. The Fermi level of semiconductors and metals are equal at the thermal equilibrium [58,50,88]. Thus, when two materials are in contact, electrons will flow from the one with the lower work function until Fermi levels equilibrate. As a result, the material with the lower work function will take on a slight positive charge while that with the higher work function will become slightly negative. The appeared potential is called the built-in field.

The built-in field causes band bending in the semiconductor near the junction. The schema of the metal-semiconductor junction is shown in Figure 2.10. In the metal-semiconductor junction, semiconductor carriers must gain enough energy to jump to the top of the conduction band. The needed barrier-surmounting energy for n-type semiconductor φ_b is equal to:

$$\varphi_b = \varphi_m - \chi_s \quad (2.22)$$

where χ_s is the semiconductor electron affinity defined to be the difference between the vacuum level and the conduction band.

When the excitation over the barrier is thermal, the process is the thermoionic emission. However, an equally important process exists in real contacts called quantum mechanical tunneling [50,88].

2.5.2 Ohmic contact technology

In real conditions, metal may react with semiconductor surfaces and form compounds with new electronic properties. Moreover, a contamination layer at the interface may effectively widen the barrier. The surface of the semiconductor may create a new electronic state. The dependence of contact resistance on details of the interfacial chemistry makes the reproducible fabrication of ohmic contacts a very serious manufacturing challenge [41]. Thus, the first step in the contact fabrication is the semiconductor surface cleaning. Surface cleaning may be performed by heating, sputter-etching, chemical etching, reactive gas etching or ion milling. After cleaning, ohmic contacts may be realized by sputtering, chemical vapour deposition (CVD) or thermal evaporation of noble metals. The sputtering is a faster method for metal deposition than the evaporation but the ion bombardment from the plasma may increase the surface state density or even invert the charge carrier type at the surface. Therefore, the gentler CVD or the thermal evaporation are increasingly preferred. Thermal evaporation and the CVD are realized through a mask to obtain the desired contact's shape. After the evaporation, annealing is used to relieve stress as well as to create an area more doped than in the semiconductor bulk.

To improve the technology of ohmic contact realization, contact resistance measurements are performed. They may be realized using a four point-probe

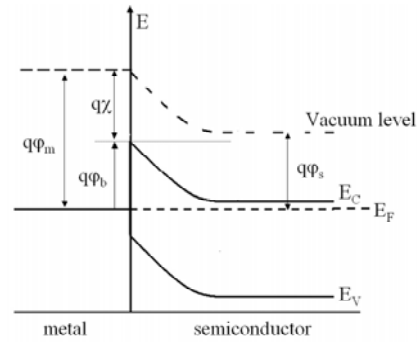


Figure 2.10: *Schema of the metal-semiconductor (type n) junction at thermal equilibrium [58].*

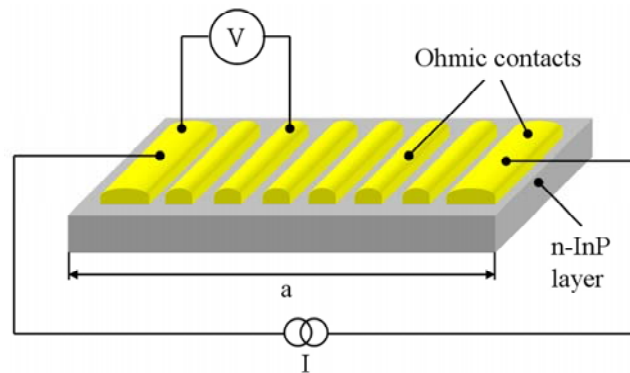


Figure 2.11: *Schema of the sample used for ohmic contacts resistance measurements [89].*

[50,91] or by measurements of tension as a function of the contact distance [89], as shown in Figure 2.11. This figure shows the structure with ohmic contacts based on the n-type InP layers prepared to measure the specific resistance of the contact. Measurements of the tension as a function of the following distance between contacts gives the distribution function of voltage. The estimation of contact resistance is given by the relation between the tension V_a for a distance equal to zero and the current:

$$R_s = \frac{V_{(a=0)}}{I} \quad (2.23)$$

Having presented, in this Chapter, InP semiconductor electronic and chemical properties (from the available literature), as well as the adsorption phenomena and the ohmic contacts realization, the next Chapter will deal with the realization of sensor structures based on n-InP epitaxial layers. Also, different techniques for sensing, chemical and electronic property investigations will be discussed. Finally, the principles and layouts of the measuring set-ups used in this work will be presented in detail.

Chapter 3

Experimental

This Chapter deals with the experimental methods used in the investigations of sensing, electrical and chemical properties of InP based gas sensor structures. In this work, the tested devices as well as measurement set-ups were created or adapted by the author to realize the systematic study of sensing mechanism of n-InP. Therefore, sensor devices as well as sensor fabrication and experimental techniques are presented. These techniques allow for the investigation of the action of oxidising gases (like nitrogen dioxide and ozone) on n-InP active epitaxial layers. Also, the Van der Pauw effect measurement technique allowing to investigate the charge carrier concentration, the mobility and the layer resistivity of the thin layers is presented. Moreover, in this Chapter, the principles of the different surface spectroscopy techniques used, as well as the experimental set-ups and analysis approaches based on spectroscopic data are detailed.

3.1 Sensor device

The realization of a sensor structure comprises a sequence of technological steps. Firstly, the InP wafer is cleaned and cleaved into the rectangular samples. Afterwards, the ohmic contacts on n-InP are realized. Finally, the complete sensor device is mounted in the measuring cell. In this section, the realization of a sensor device from cleavage through ohmic contact fabrication to mounting into the measuring cell, as well as the sensor structure are presented.

3.1.1 n-InP epitaxial layers

The gas active epitaxial n-InP layers were produced in the Institut Electronique et Microelectronique du Nord (IEMN) located in Lille, France. The n-type InP epitaxial layers were grown by molecular beam epitaxy on a semi-insulating, iron-compensated (100) InP substrate. They were doped by silicon; the donor concentration N_D given by the producer is $2 \cdot 10^{16} \text{ cm}^{-3}$. Thicknesses of the epitaxial layers used in experiments are 0.2, 0.3 and 0.4 μm . The 3 different

series of wafers with epitaxial layers were used, all wafers were coming from the same producer: IEMN. This gave us a possibility to realize around 30 structures tested in terms of their reproducibility of the sensing, electronic and chemical properties.

3.1.2 Ohmic contacts

Ohmic contacts are realized on n-InP epitaxial layers by thermal evaporation of noble metal gold (Au) and germanium (Ge). Before thermal evaporation, the n-InP sample is cleaned in ethanol and methanol. After cleaning, the sample is mounted in the evaporator chamber (see Figure 3.1). Once the sample mounted, it is heated from ambient temperature to 120 °C by steps of 10 °C in order to desord any adsorbed gases. Finally, evaporation of contact metals is done through a stainless steel mask. Evaporated metals and their thickness are as follows: Au (10 nm) / Ge (35 nm) / Au (150 nm), these thicknesses were already chosen in previous work [19,26].

After the evaporation process, the sample is annealed under an hydrogen atmosphere with sequences of 200 °C (for 3 min), 250 °C (for 1 min) and 300 °C (for 10 s). Then, it is cleaved and the obtained surface area is 121 mm² (Hall effect measurements) and 16 mm² for an investigation of sensing parameters. Finally, to measure the sensitive n-InP epitaxial layer resistance, copper wires screened by Sn are stuck on ohmic contacts using tin balls and silver (Ag) paste. The structure wire/tin ball is shown in Figures 3.2 and 3.3, where the detailed sensor structure as well as photos of sensors with different n-InP layer thicknesses are presented.

3.1.3 Sensor structure

The last step of the sensor fabrication consists in the realization of a temperature regulation system. As electrical characteristics of III-V compounds based semiconductors strongly depend on temperature, interactions between gas and sensitive material strongly depend on the work temperature of this material, too. Each sensor is glued onto an alumina heating substrate fitted with a screen-printed platinum resistor on its backside. The heating substrate resistance is in the configuration of a 'Wheatstone bridge' that allows for heating and temperature control.

The working temperature is varied between 20 °C and 120 °C to investigate the sensor characteristics including the sensitivity of the layer resistance, the response time and the reproducibility of results with temperature.



Figure 3.1: *Evaporator chamber used in ohmic contact fabrication.*

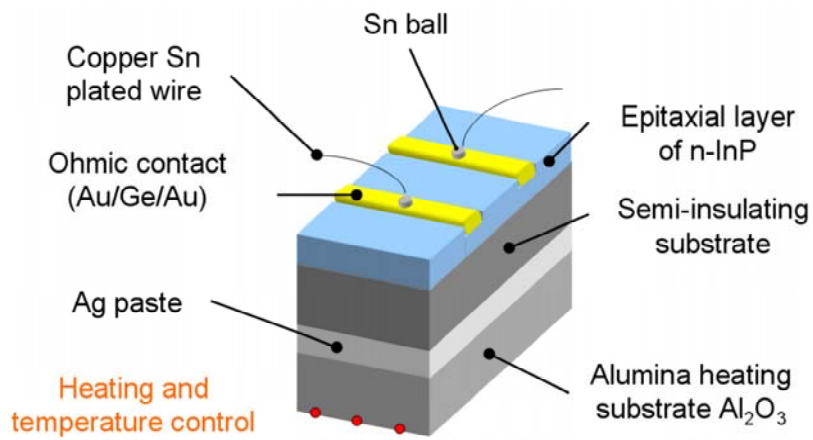
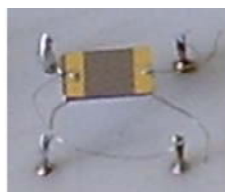


Figure 3.2: *Schematic picture of a resistive sensor device.*



(a) $0.2 \mu\text{m}$.



(b) $0.3 \mu\text{m}$.



(c) $0.4 \mu\text{m}$.

Figure 3.3: *Resistive sensor devices used in experiments.*

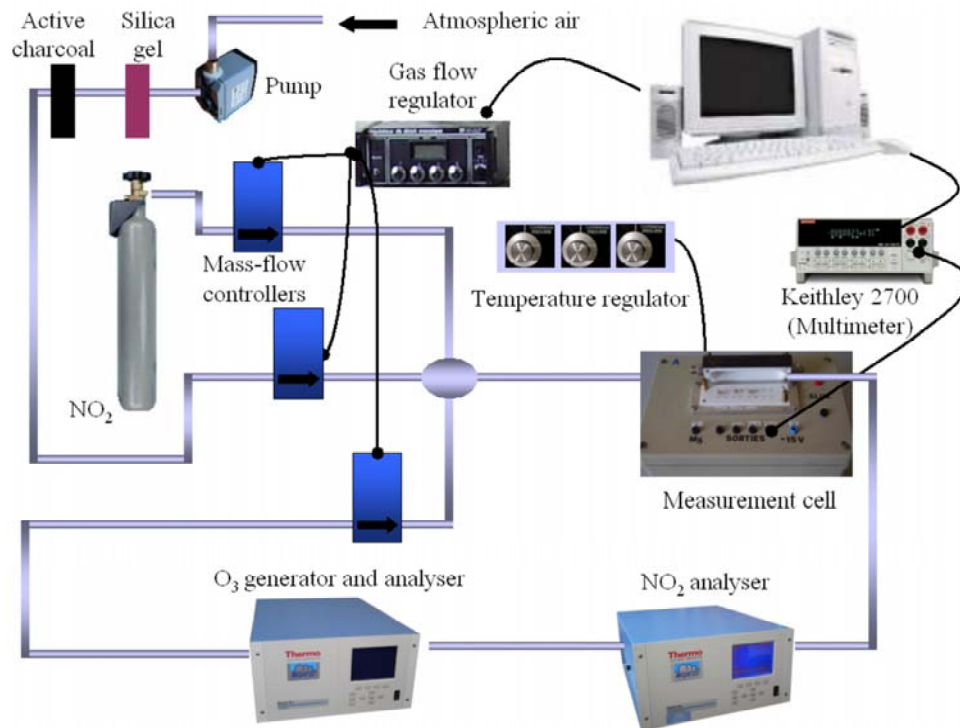


Figure 3.4: Schematic drawing of measurement set-up.

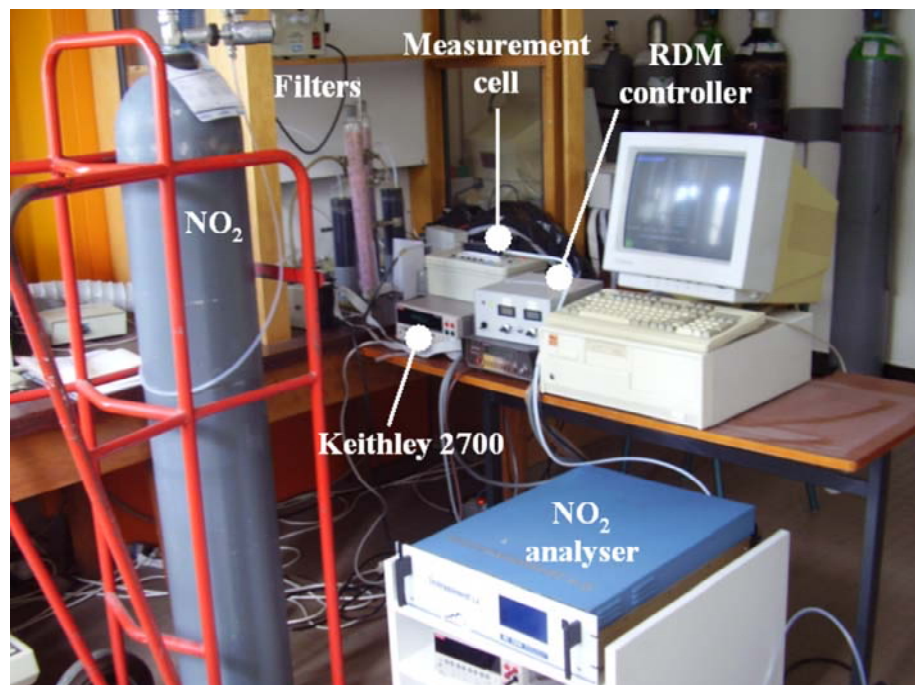


Figure 3.5: Measurement set-up used in sensing experiments in the gas sensor group in laboratory LASMEA, Clermont Ferrand (France).

3.2 Gas measurement set-up

For n-InP sensing properties investigations, tests with oxidising gases are realized. For sensing experiments, sensor devices are placed in a measuring cell, in darkness and exposed to cycles of NO₂ diluted in pure dry air. The flow is kept constant at 50 l/h. Gas flow and oxidising gas concentration are computer controlled. Rate diluting mass (RDM) controllers are used to obtain oxidising gas concentrations of less than 50 ppb (see Figure 3.4).

After being delivered from the bottle, NO₂ is diluted in dry and pure air to obtain the desired gas concentration and finally, passes through the measurement cell. Its concentration is checked at the output of the measurement cell by a chemiluminescent NO_x monitor (42i Megatec Thermo Electron Corporation). Experiments have included various sequences of gas exposures. All these sequences start and finish with exposure of the gas sensor to pure and dry air. Dry, pure air is obtained by filtering atmospheric air through silica gel and active charcoal.

The output signal is monitored through the recording of the sensor resistance changes (between two ohmic contacts) using a Keithley 2700 digital multimeter. In conclusion, as it is shown in the Figure 3.5, the set-up for sensing properties measurement is equipped with:

- the measurement cell connected with a temperature regulator and a Keithley 2700 multimeter;
- a computer to control sequences of the gas exposure and gas flow;
- filters to obtain pure and dry air;
- the RDM configuration to control the gas concentration;
- the NO₂ analyser to check the gas concentration.

Measurement cell

The measurement cell is designed to allow gas flow and avoid any photo-conduction effect. Its design allows to accommodate up to 4 sensors during the same experiment. It is made of Teflon, rectangular in shape and protected from ambient light by a coating of black material. It is connected on one side with the gas source (gas inlet) and with the gas analyser to check the gas concentration (gas outlet) on the other one. Figure 3.6 shows a schema and a photo of measurement cell.

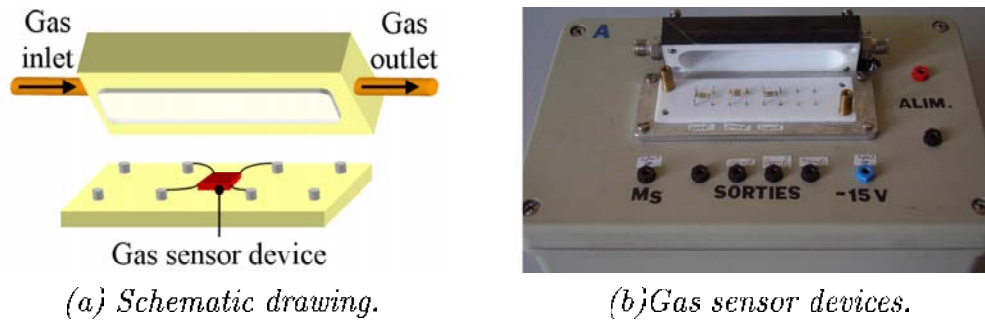


Figure 3.6: *Rectangular measurement cell.*

3.3 Electronic properties characterization

To characterize n-InP electronic properties in terms of charge carrier concentration, mobility and sample resistivity, the Van der Pauw method was introduced. Hall effect measurements give results of ρ , μ_H and n , but require a thick sample with electrical contacts on its sides, in contrary to Van der Pauw measurement method that can be performed for any thin sample of whichever geometry [90,91]. Therefore, for the n-InP samples with thicknesses in the sub-micrometer range the Van der Pauw method is introduced in Hall effect measurements. The Hall effect principle is given in Appendix G. This method of characterization was used not only to estimate the electronic base state of the examined InP sensing layers but also to estimate the changes in the electronic state under gas action, it was possible by introducing modifications in Hall measurement cell.

3.3.1 The Van der Pauw method

In the Van der Pauw measurements the n-InP samples with thicknesses of the 0.2 and 0.4 μm were used. However, the measurements of ρ , μ and n for thin sample with thicknesses in the sub-micrometer range is possible, but few following conditions must be fulfilled [90]:

- contacts are at the circumference of the sample;
- contacts are sufficiently small and situated at the corners of the sample;
- the sample is homogeneous in all its thickness;
- no holes in the sample between contacts.

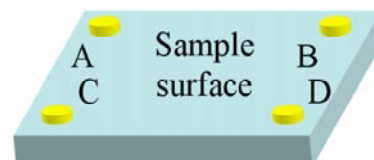


Figure 3.7: *Sample used in Van der Pauw method.*

Thus, to fulfil the conditions for using this method, the ohmic contacts are realized in corners of the n-type InP rectangular sample. Ohmic contacts (A, B, C, D) are situated as shown in Figure 3.7.

Once the current I_{BD} is injected between contacts B and D, the resistance $R_{(BD,AC)}$ is measured. The resistance $R_{(CD,AB)}$ is defined for the current I_{CD} injected between contacts C and D.

$$R_{(BD,AC)} = \left| \frac{V_A - V_C}{I_{BD}} \right| \quad (3.1)$$

$$R_{(CD,AB)} = \left| \frac{V_A - V_B}{I_{CD}} \right| \quad (3.2)$$

When the thickness of the sample d is known, the resistivity of the sample is given by the following formula [90]:

$$\rho = \frac{\pi \cdot d}{\ln(2)} \cdot \left[\frac{R_{(BD,AC)} + R_{(CD,AB)}}{2} \right] \cdot f \left(\frac{R_{(BD,AC)}}{R_{(CD,AB)}} \right) \quad (3.3)$$

where f is a function dependent on the ratio $\frac{R_{(BD,AC)}}{R_{(CD,AB)}}$ and supposed to satisfy the following relation:

$$\left[\frac{R_{(BD,AC)} - R_{(CD,AB)}}{R_{(BD,AC)} + R_{(CD,AB)}} \right] = f \cdot \text{Arccosh} \left[\frac{1}{2} \cdot \exp\left(\frac{\ln 2}{f}\right) \right] \quad (3.4)$$

In conditions where $R_{(BD,AC)}$ and $R_{(CD,AB)}$ are different, f is given by Equation 3.5. Its graphical representation can be found in Appendix C.

$$f = 1 - \left[\frac{R_{(BD,AC)} - R_{(CD,AB)}}{R_{(BD,AC)} + R_{(CD,AB)}} \right]^2 \cdot \frac{\ln 2}{2} - \left[\frac{R_{(BD,AC)} - R_{(CD,AB)}}{R_{(BD,AC)} + R_{(CD,AB)}} \right]^4 \cdot \left(\frac{(\ln 2)^2}{4} - \frac{(\ln 2)^3}{12} \right) \quad (3.5)$$

The measured $R_{(AD,BC)}$ is equal to:

$$R_{(AD,BC)} = \left| \frac{V_B - V_C}{I_{AD}} \right| \quad (3.6)$$

Additionally, it is needed to estimate R_H . This constant is determined by the difference in $R_{(AD,BC)}$ measured with and without magnetic field \vec{B} applied perpendicular to the sample surface:

$$\Delta R_{(AD,BC)} = R_{(AD,BC)}_{\vec{B}=\vec{0}} - R_{(AD,BC)}_{\vec{B} \neq \vec{0}} \quad (3.7)$$

Then, the Hall constant, the Hall mobility and the charge carrier concentration are given by following equations:

$$R_H = \frac{|\Delta R_{(AD,BC)}| \cdot d}{B} \quad (3.8)$$

$$\mu_H = \frac{|\Delta R_{(AD,BC)}| \cdot d}{\rho \cdot B} \quad (3.9)$$

$$n = \frac{B}{q \cdot d \cdot |\Delta R_{(AD,BC)}|} \quad (3.10)$$

3.3.2 Hall measurement cell

Hall effect measurements are done in a special cell allowed for experiments in the electromagnetic field. The standard measurement cell is modified to one connected with the gas inlet and its outlet to allow for gas flow (see Figure 3.8.a). To obtain the desired gas concentration configurations of filters (to obtain pure and dry air) and the RDM system (to obtain the desired gas concentration) used are the same as presented in section 3.2. The tested samples series were n-InP epitaxial layers with thicknesses of 0.2 and 0.4 μm and surface areas of 121 mm^2 . The configuration of ohmic contacts was as in Figure 3.8.b.

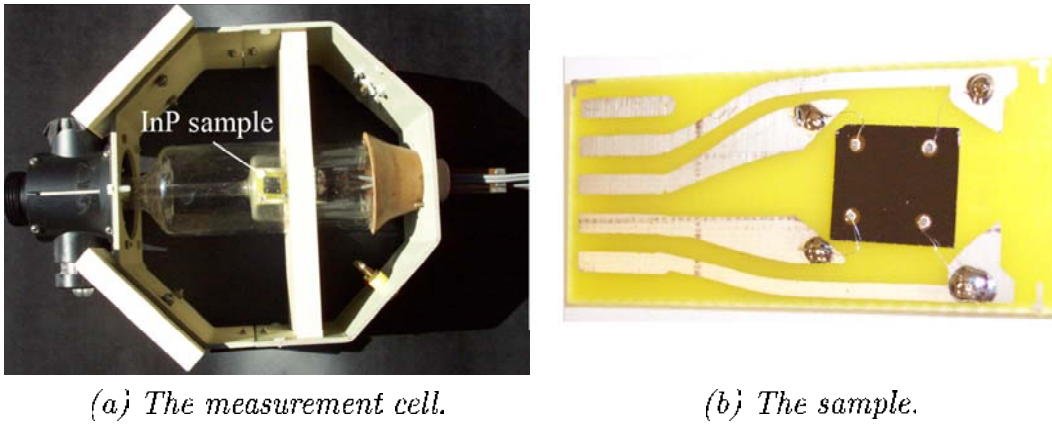


Figure 3.8: Hall effect sample and cell used in measurements.

3.4 Chemical properties of InP surface

For a good comprehension of the sensor behaviour, the knowledge of electronic properties combined with chemical ones is needed. Thus, the investigation of InP surface chemical status and its changes due to gas action is realized

by means of photoelectron (XPS) and electron (AES) spectroscopic techniques. The principle of these techniques is to collect electrons excited and emitted from the surface substrate. On the base of collected electrons, the chemical characterization is done. In this section, spectroscopic studies as well as their principles and the measurement set-ups used are described.

3.4.1 Secondary electrons

XPS and AES techniques are based on the analysis of energy of secondary electrons which come from inelastic collisions between the primary beam (photons or electrons) and the atom. When bombarding a solid surface with a monoenergetic beam characterized by its kinetic energy E_0 and its intensity I_0 , one gets the spectrum of secondary electrons. Figure 3.9 shows the contribution of emitted secondary electrons $N(E)$. In the spectrum, four different regions can be identified:

1. the elastic peak that corresponds to the energy E_0 of bombarding electrons;
2. the intermediate region of energy loss peaks where electrons have lost their energy due to the interaction with plasmons or ionisation;
3. the secondary electron peaks or Auger electron peaks that are used in Auger electron spectroscopy analysis;
4. the region of secondary electrons that are emitted in an inelastic way.

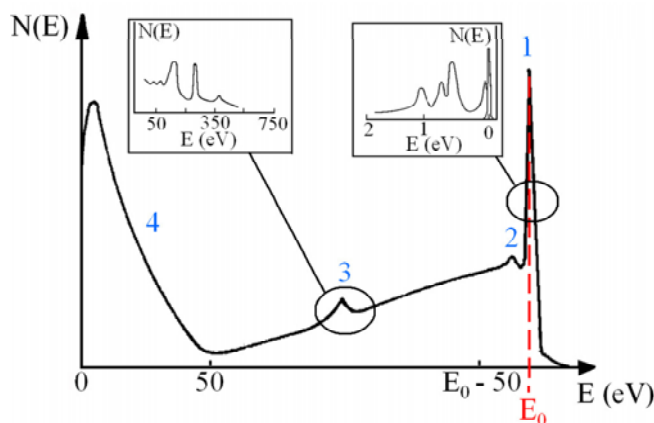


Figure 3.9: *Distribution of emitted electrons from the solid surface under an electron beam excitation [92,93].*

3.4.2 Attenuation length of electrons in solids

An inelastic scattering of the electron in the solid may be characterized by an inelastic mean free path IMFP. Often, in the spectroscopic analysis the attenuation length is measured because it is equal around to the mean free path of electrons that is the average distance at which the number of electrons escaping without energy loss due to an inelastic scattering decreases to $\frac{1}{e}$ (around 36.8 %) [94,95]. There exists also the escape depth of electrons that is called the information depth. The value of the attenuation length λ_i of electrons depends on both the material and the electron energy. For electrons emitted at an angle θ to the normal from a solid surface, the unscattered intensity $I(x)$ from a source at a depth x below the surface follows the approximate relation [79,96,97]:

$$I(x) = I_0(x) \cdot \exp\left(\frac{-x}{\lambda_i \cdot \cos(\theta)}\right) \quad (3.11)$$

Thus, in Auger and X-ray photoelectron spectra from solid surfaces, the average information depth is characterized by λ_i and $\cos(\theta)$. For elements, an empirical and approximative description of λ_i in nanometers is given by M.P. Seah [98]:

$$\lambda_i = 538 \cdot a \cdot E^{-2} + 0.41 \cdot a^{\frac{3}{2}} \cdot E^{\frac{1}{2}} \quad (3.12)$$

where E is the electron energy (in eV) and a^3 is the volume of one atom of the element in the solid state (in nm^3).

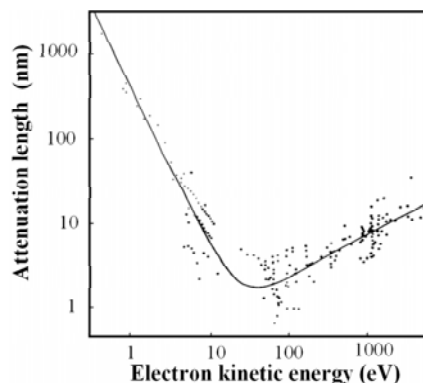


Figure 3.10: *Attenuation length versus kinetic energy of electrons.*

This description fits the experimental data on average to a standard deviation of 30% (see Figure 3.10). The attenuation length is responsible for the escape depth of emitted electrons that, in the case of AES and XPS spectroscopy (the energy of primary beam from 20 to 2000 eV), limits the analytical region to depths ranging between 2 and 5 nm [99].

3.4.3 X-ray photoelectron spectroscopy

K. Siegbhan and his research group at the University of Uppsala, Sweden developed the first X-ray Photoelectron Spectroscopy (XPS) in the mid-sixties [100]. The technique was first known by the acronym ESCA (Electron Spectroscopy for Chemical Analysis) [101]. Surface analysis by XPS involves irradiating a solid in vacuum with monoenergetic soft X-rays and analysing emitted electrons by their energy. The spectrum is obtained as a plot of the number

of detected electrons per energy interval versus their kinetic energy. Each element has an unique spectrum, which is approximately the sum of the peaks of the individual constituents. X-rays usually used are MgK $_{\alpha}$ (1253.6 eV) or AlK $_{\alpha}$ (1486.6 eV). These photons have limited penetrating power in solids of the order 10 μm .

Principle of XPS techniques

The principle of photoelectron spectroscopy is based on the interaction between an electromagnetic wave and atoms in matter. The process of photoelectron emission from solids consists of three steps [102]:

1. X-rays are adsorbed by atoms and photoelectrons are emitted (photoelectron process);
2. a part of the electrons generated within the solid moves toward the surface (electron attenuation length);
3. photoelectrons, which have reached the surface, are emitted into vacuum.

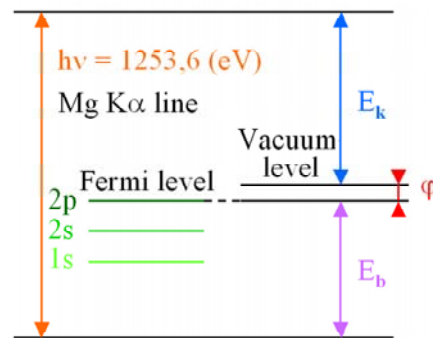


Figure 3.11: *Energy diagram of photoelectron emission [102].*

As it is shown in Figure 3.11, the energy conservation rule holds for the following parameters: energy of the excitation X-rays that is equal to $h \cdot \nu$, the electron binding energy E_b , the kinetic energy of emitted photoelectrons E_k and the work function φ depending on both material and spectrometer. Therefore, emitted photoelectrons have got the kinetic energy given by the following equation:

$$E_k = h \cdot \nu - E_b - \varphi \quad (3.13)$$

where the Fermi level corresponds to zero binding energy. E_b is defined by the difference between the total energy at the initial state and that at the final state of the photoelectron emission process. The binding energy slightly differs depending on the chemical environment of atoms, so XPS can be used for the chemical state analysis of the material.

3.4.4 Auger spectroscopy

Auger Electron Spectroscopy (AES) has been named after French physician P. Auger (1899-1993) who discovered this phenomenon in 1923 [103]. The emission process is commonly referred to as an Auger emission and the emitted electron is called an 'Auger electron'. AES is a fast and non-destructive analytical technique used to determine the elemental composition of a few atomic layers of a surface or exposed interface in a solid material.

Principle of the Auger technique

AES is a technique generally using an electron beam for electron excitation. In the Auger process, three levels of atom energy are involved. The primary beam causes an ionisation of a core level K by the emission of an electron. The core hole is produced and the electron from the more external energy level L fills up this hole. Eventually, losses of potential energy due to the filling this core level may appear as a photon (X-ray generation, fluorescence) or as kinetic energy given to another shallowly bound electron (emission of the Auger electron). These competing processes are dominated by the photon emission only when the initial core hole is deeper than about 10 keV. In Figure 3.12, the relaxation process by Auger electron emission is shown. In this schema, the initial vacancy appears in the K shell.

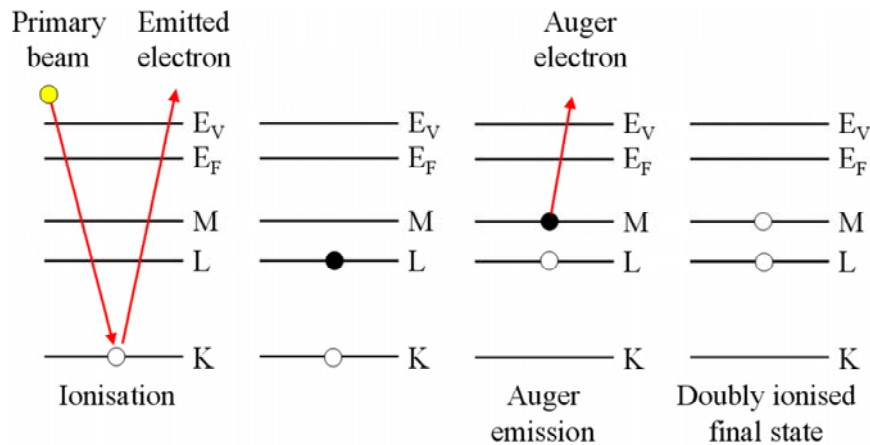


Figure 3.12: *Schema of the Auger process [104].*

The kinetic energy of the Auger electron E_{KLM} is equal to the energy difference of the singly ionized initial state and the doubly ionized final state. This energy can be estimated by the difference in binding energy of the three energy levels within which the Auger process takes place:

$$E_{KLM} = E_K - E_L - E_M \quad (3.14)$$

M.F. Chung and L.H. Jenkins have determined the empirical equation of the kinetic energy of Auger electrons [105]. They proposed that the effective

binding energy for the doubly ionised state is equal to the average value of binding energies corresponding to elements of atomic levels Z and $Z + 1$:

$$E_{KLM} = E_K(Z) - \frac{1}{2} \cdot [E_L(Z) + E_L(Z + 1)] - \frac{1}{2} [E_M(Z) + E_M(Z + 1)] \quad (3.15)$$

So, this energy does not depend on the energy of the primary beam and is characteristic of the emitter atom. Then, in AES, the identification of elements is determined by the energy position of Auger peaks.

3.4.5 Surface spectroscopy analysis

Once the electrons have been collected, they are the source of the chemical status knowledge of the investigated semiconductor near-surface region. There are two types of analyses. The first one is qualitative and it determines existing atoms on the surface. The second is quantitative and it theoretically gives the quantitative data of found elements. The quantification of observed elements is determined from relative intensities of electron peaks. However, the measured intensity of an arbitrary peak is a complicated function of a large number of factors, both instrumental and related to the nature of the sample [104], such as:

- the number of atoms of the element per unit volume;
- the primary electron current;
- the Auger transition probability for the element;
- the element ionization cross section by incident and scattered electrons;
- the mean free path of the emitted Auger electron;
- the angle between collected electrons and the normal to the surface;
- the analyser solid angle of acceptance;
- the analyser transmission function;
- the electron detector efficiency;
- the surface roughness;
- the backscattering factor.

So, the elemental quantification from first principles is nearly impossible using AES and XPS method. Thus, commonly used approaches to quantification involve different assumptions and approximations.

Qualitative analysis

In the case of Auger and X-ray spectroscopy, collected electrons are characteristic of the emitter atom. A XPS spectrum has Auger electron peaks (KLL, LMM, etc.) as well as photoelectron peaks corresponding to various energy levels (1s, 2s, 2p, etc.), AES spectrum consists only of AES peaks. Photoelectrons as well as KLL, LMM and MNN Auger electrons produce observable peaks, which allow for identification of all elements above helium by scanning an energy range from 20 to 2000 eV. The identification of peaks is collected in the charts of the Handbook of Auger Electron Spectroscopy for Auger peaks and in the Handbook of X-ray photoelectron spectroscopy for XPS ones [102,106]. These charts give the relationship between electron energies and atomic number. In the case of XPS technique, the peaks are sometimes shifted, i.e., variations in the elemental binding energies is observed. These variations depict chemical bondings of compounds existent on the solid surface.

Although, peaks from different elements can sometimes overlap, a complete obliteration from a trace impurity by another dominant species seldom occurs in practice.

Quantitative analysis

XPS peak quantitative analysis is based on the photoelectron peak intensity I_i , emitted from element i . The number of photoelectrons originating from a depth x below the surface and emerging at an angle θ to the normal to a solid surface, is proportional to the peak intensity I_0 . It also depends on the electron attenuation length λ_i and by $\cos(\theta)$ [79,96,97]. While the peak intensity of non-scattered electrons I_i is defined by Equation 3.11, I_0 is proportional to the element concentration and depends also on the following factors: photoionization cross section, instrumental factors (like analyser transmission), efficiency of the detector and sample area analysed by the photoelectron flux. Thus, the peak intensity coming from the analysed solid surface is described by following integral:

$$I_i = T_i \cdot A_i \cdot \phi_i \cdot \sigma_{cs_i} \cdot \int_0^{d_{XPS}} s_i \cdot C_i(x) \cdot \exp\left(\frac{-x}{\lambda_i \cdot \cos(\theta_i)}\right) dx \quad (3.16)$$

where:

- T_i is the analyser transmission;
- A_i is the efficiency of detector;
- ϕ_i is the number of photons per second sent to the investigated element;
- σ_{cs_i} is the photoionization cross section;

- s_i is the sample area analysed by photoelectron flux;
- $C_i(x)$ is the concentration of elements i located at the depth x from the sample surface;
- λ_i is the electron attenuation length;
- θ_i is the take off angle of electrons;
- d_{XPS} is the XPS information depth.

As for XPS peaks, the measured Auger intensity I_i is a value proportional to the concentration to the analysed element i . In contrary to XPS analysis, a common AES quantitative analysis involves defining sensitivity factors S_i . S_i are normalized to the reference material and can be tabulated for different voltages of the incident electron beam.

For two pure elemental samples defined by:

$$\frac{I_1}{S_1} = \frac{I_2}{S_2} \quad (3.17)$$

each sensitivity factor is related to the reference sample sensitivity factor as follows:

$$S_1 = \left(\frac{I_1}{I_{ref}} \right) \cdot S_{ref} \quad (3.18)$$

The expression for the atomic concentration X_i of every element i can be written as:

$$X_i = \left(\frac{\frac{I_i}{S_i}}{\sum_j \frac{I_j}{S_j}} \right) \quad (3.19)$$

where the summation is over all observed elements.

This expression can be used for all homogeneous samples if ratios of sensitivity factors in the matrix are constant. However, it minimizes the effect of the surface roughness. Table 3.1 gives the sensitivity factors for different energies of the incident electron beam [106].

Table 3.1: *Sensitivity factors used in AES analysis, for different energies of incident electron beam [106].*

Atom	$E_p = 3 \text{ keV}$	$E_p = 5 \text{ keV}$	$E_p = 10 \text{ keV}$
P	0.65	0.45	0.3
In	0.95	0.975	0.65
C	0.2	0.14	0.08
O	0.5	0.4	0.35
Au	0.018	0.35	0.0525
Ge	0.1	0.14	0.125

3.4.6 Electron analysers

Electrons emitted from the surface are accompanied by a noise signal, that can obliterate the information regarding the chemical status of the surface. To separate electrons emitted from the surface of the solid from the noise level and to separate the electron energies coming from different element electron energy analysers are used in surface spectroscopy techniques. Thus, the analysis of the desired electron signal is possible because only electrons with a certain kinetic energy pass through analysers. The current at the exit of the analyser is given by the Equation 3.20 [92]. The detector used (a 'channeltron', comprised of several electron multiplying electrodes) is situated at the exit plane of the analyser. The channeltron amplifies the current of a single electron/ion with a factor 10^8 but, even so, the resulting current pulse has a very small amplitude. Thus, at the output of the channeltron, the current passes into preamplifier. The signal is then processed by means of a pulse counter which delivers the electron/ion energy spectrum.

$$I(E) = \int_{E - \frac{\Delta E}{2}}^{E + \frac{\Delta E}{2}} T(E) \cdot N(E) dE \approx T(E) \cdot N(E) \cdot \Delta E \quad (3.20)$$

where $N(E)$ is the energy distribution of collected electrons and $T(E)$ is one of the parameters that characterise the emission process. It is called 'transmission' of analyser and is equal to:

$$T(E) = A \cdot E^{-k} \quad (3.21)$$

where:

- A is a constant;
- E is the kinetic energy of electrons;
- k is the constant depending on the analyser.

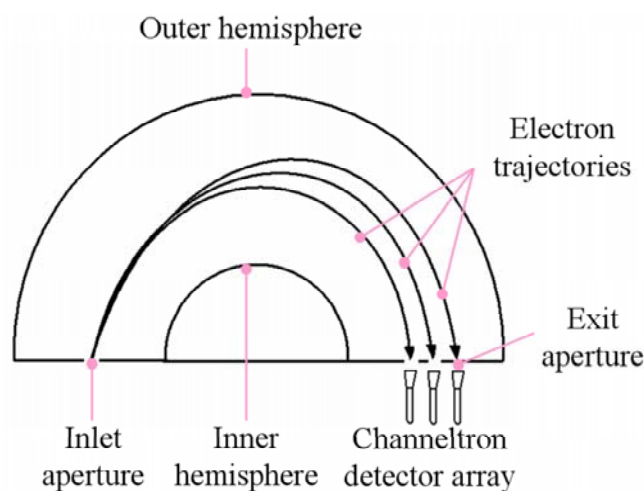


Figure 3.13: *Schematic diagram of a hemispherical analyser [104].*

Among all existant analysers, the Hemispherical and Cylindrical Mirror Analysers are the most used ones. Therefore, the following section deals with the description of electron analysers of this kind used for XPS and AES measurements.

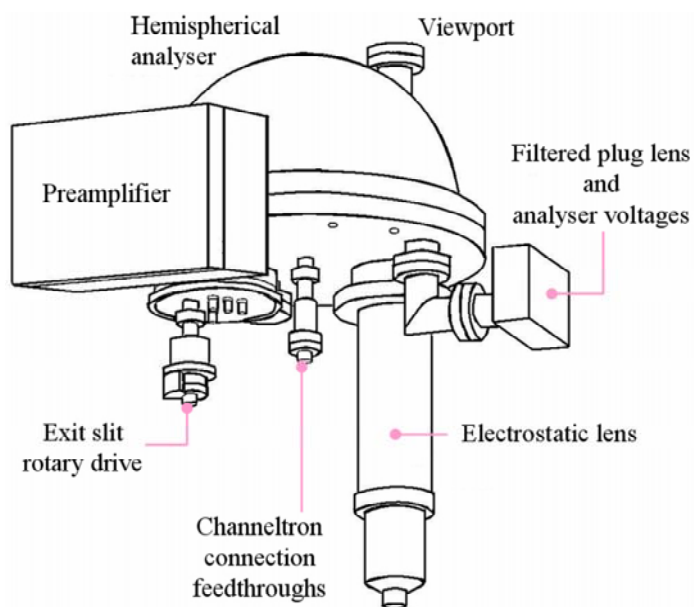
Hemispherical analyser

The hemispherical analyser is comprised of two concentric hemispherical electrodes, respectively biased with opposite potentials (see Figure 3.13). This analyser disperses electrons according to their energy across the exit plane (between the two hemispheres) and focuses them from the entrance to the exit plane. Only electrons with a certain energy pass from entrance to output of the analyser.

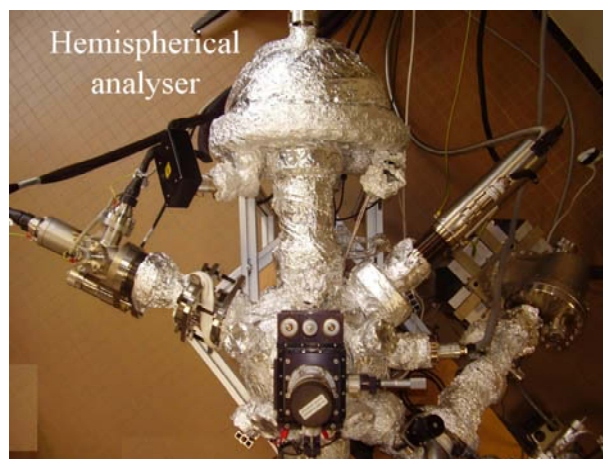
The analyser used in experiments is a commercial Electron Analyser 125 produced by OMICRON electronics GmbH (Germany). It is based on a 125 mm mean radius electrostatic hemispherical deflection. The schematic picture of the equipment of the EA 125 hemispherical analyser is shown in Figure 3.14. It consists of:

- a hemispherical analyser;
- an electrostatic lens;
- filtered power supplies to provide analyzer and lens voltage;
- channeltron connection feedthroughs;
- a preamplifier;
- an entrance slit rotary drive;

- an exit slit rotary drive;
- a viewport.



(a) Major component schema.



(b) EA 125 analyser.

Figure 3.14: Hemispherical analyser used in XPS set-up (the laboratory of LASMEA in B. Pascal University, France).

As it is shown in Figure 3.14, the input lens collects electrons from the source and focuses them onto the entrance aperture of the analyser while simultaneously adjusting their kinetic energy to match the analyser pass energy. The lens is also designed to define the analysis area and the angular acceptance of electrons that pass through the hemispherical analyser. The lens design employs

a double lens concept whereby one is stuck above the other. The first lens is an Einzel lens that selects the analysis area (spot size) and the angular acceptance. The second lens retards or accelerates electrons to match the pass energy and uses a zoom lens function to ensure that the focal point remains on the analyser entrance aperture.

CMA analyser

The other largely used analyser is the 'Cylindrical Mirror Analyser' (CMA). The basic analyser consists of two cylinders; the inner one is at the ground potential and the outer one at a negative potential. These potentials determine the pass energy. As it is shown in Figure 3.15, an electron detector is positioned behind an aperture placed in the focal plane of the CMA. The CMA mean acceptance angle α is defined by an entrance slit position in the inner cylinder. The energy resolution is primarily determined by the chosen value of the acceptance half angle $\Delta\alpha$ that is defined by its width and size of the exit aperture. In common practice where α is equal to 42.31° and $\Delta\alpha$ equal to $\pm 6^\circ$, it allows for a transmission T of around 7% and energy resolution $\frac{\Delta E}{E}$ from 0.3 to 0.6% [104]. Advantages of the CMA method are a good resolution, a high transmission and a short working distance. Moreover, it has the strong geometric advantage of collecting electrons uniformly around 360° angle around the horizontal axis.

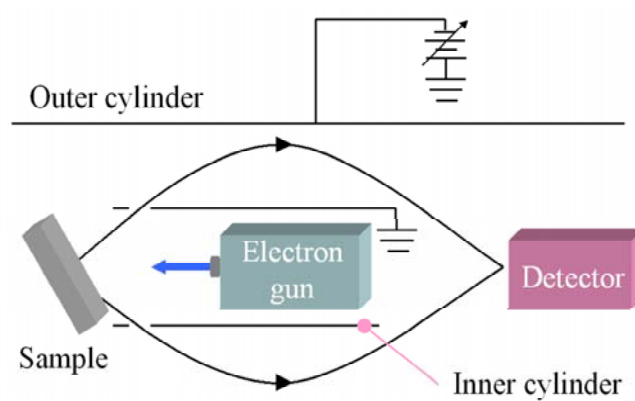


Figure 3.15: *Schema of CMA [104].*

3.4.7 Measuring set-up

This section deals with measuring set-ups used for spectroscopic analysis. The XPS spectrometer as well as the AES microprobe are detailed. Measurement aspects and experimental conditions are also presented.

XPS experimental set-up

For our studies, the LASMEA (Blaise Pascal University, Clermont-Ferrand, France) spectrometer shown in 3.17 was used. It is equipped with:

- a X-ray source MgK_α with an energy of 1253.6 eV;
- a hemispherical analyser for photoelectron energy analysis that allows to adjust the constant pass energy at 20 eV for high-resolution narrow scans and 50 eV for low-resolution wide scans[107].
- an analysis chamber with a pressure in the range below 10^{-10} Torr (see Figure 3.16);
- an introduction chamber with a sample introduction system;
- a sample positioning system (manipulator) allowing displacement along the x , y , z axes as well as rotation;
- a computer for instrument control, data acquisition and data analysis.

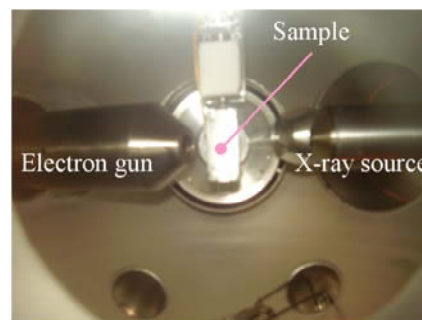


Figure 3.16: *Analysis chamber.*

AES experimental set-up

For AES studies, a PHI 600 Scanning Auger Microprobe (Physical Electronics, USA) in the laboratory of Applied Physics Department, Institute of Physics, Silesian University of Technology was used. The owner of the PHI 600 SAM system is the High-Tech International Services, Rome (Italy). The PHI 600 SAM system allows for collection of the AE spectra under pressures of about $4 \cdot 10^{-8}$ Torr. The primary electron energy was of 10 keV with an incident angle of about 30° . The sample current was 10 nA. The PHI 600 SAM system is shown in Figure 3.18 and it is equipped with:

- an electron optical column for generating, focusing the electron beam as well as scanning samples with this beam. The beam current is variable over a range from 1 to 100 nA and beam diameter from 30 to 100 nm;
- a Secondary Electron Detector (SED) for doing secondary electron imaging of the sample;
- a single pass Cylindrical Mirror Analyser (CMA) for Auger electron energy analysis with multi-channel detection;

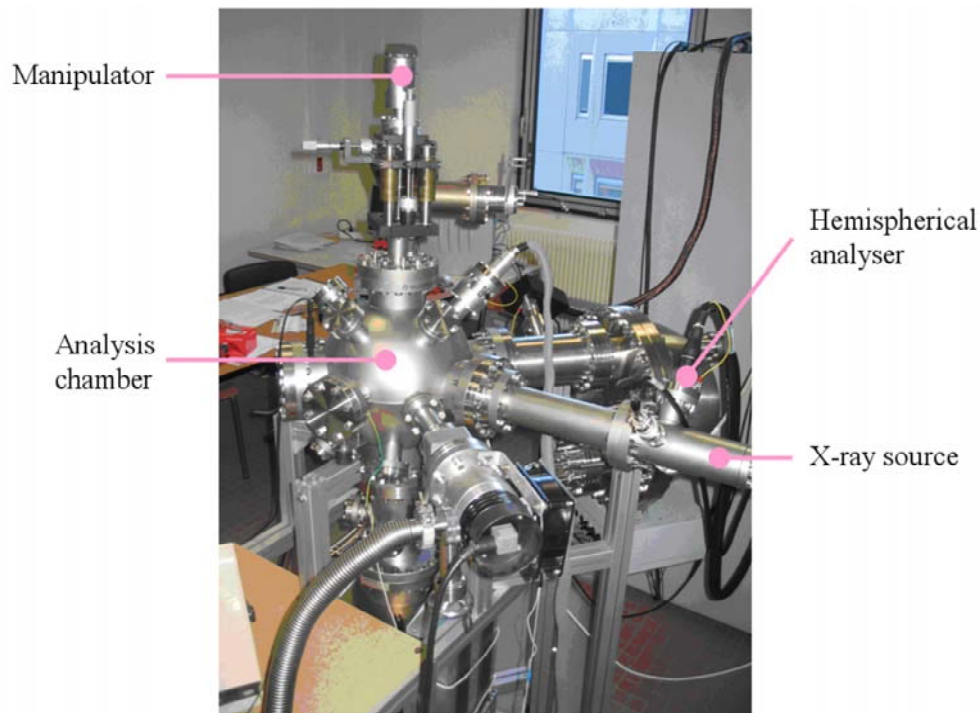


Figure 3.17: XPS measurement set-up (the laboratory of LASMEA, France).

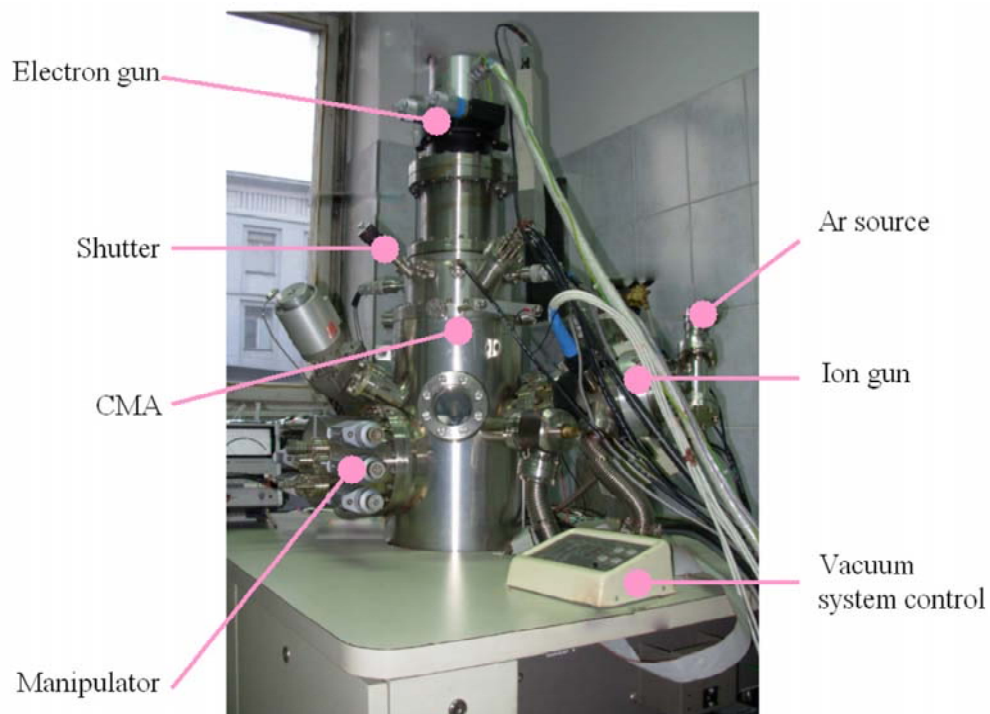


Figure 3.18: PHI 600 SAM system (Institute of Physics in Silesian University of Technology, the owner is High-Tech International Services, Rome).

- a scanning argon ion gun with a differential pumping for in-situ sample cleaning and sputter depth profiling;
- an analysis chamber with a base pressure in the range below 10^{-9} Torr and with a load locked sample introduction system;
- a sample positioning system with five axes of x , y , z , tilt and rotation;
- a computer for instrument control, data acquisition and data analysis.

Scanning argon ion gun

The PHI 600 Scanning Auger Microprobe is also equipped with an Ar^+ ion gun with a differential pumping for sputtering the sample. The sputtering is a destructive method used to obtain in-depth profiles of a sample (elemental composition) and analyse possible buried interfaces by erosion of the covering material, as shown in Figure 3.19. It is done by ejecting atoms from a solid targeted material into the gas phase due to energetic ions bombarding of the sample surface. These collisions cause a momentum exchange between ions and atoms in the sample. To measure the efficiency of the sputtering process, the sputtered rate has to be defined. The sputtered rate depends on the energy of incident ions, their masses, masses of targeted atoms and also on the binding energy of atoms in the material.

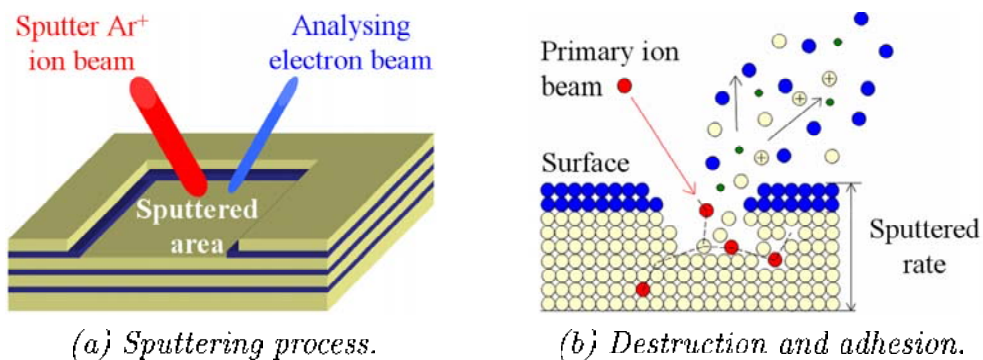


Figure 3.19: *Anisotropic destruction in sputtering process and adhesion of bombarded ions and electrons (green circle).*

In the in-depth profiling analysis, the source of quantitative information like thickness of analysed layers is the sputtered depth characterized by sputtering rate. For estimation of the sputtering rate, the sputtering depth for the reference sample and the material hardness data are needed. In this Thesis the reference sample was a well-defined 100 nm thick SiO_2 layer grown on a Si substrate. In order to estimate the sputtering rate for the InP material, first the sputtering rate of SiO_2 was determined from the elemental depth profile, and then the

sputtering rate for InP was estimated using the hardness coefficients of these materials.

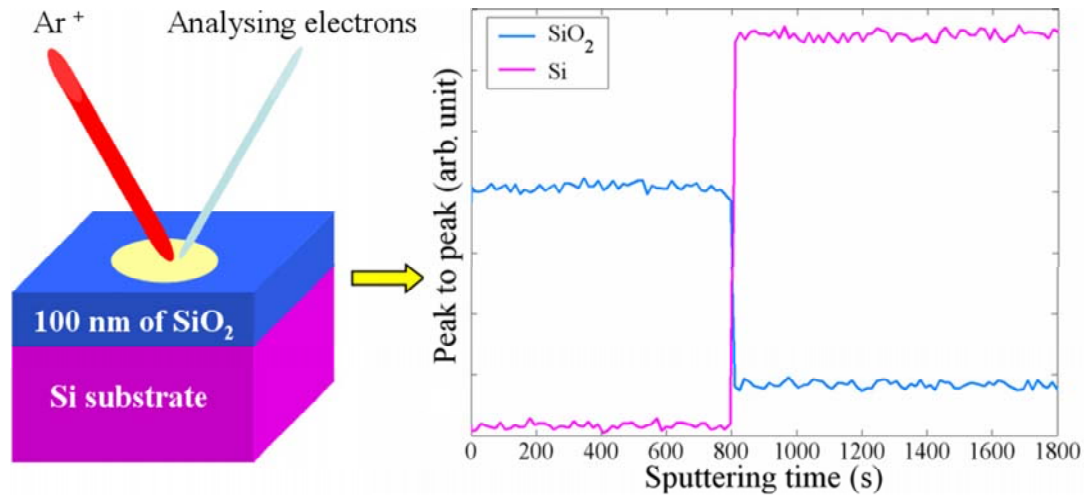


Figure 3.20: *Sputtering rate estimation for the reference 100 nm SiO₂ sample for an incident beam energy of 3 keV.*

The quality index of depth profiles and sputtering rate is the depth resolution Δx [109]. In practice, Δx corresponds to the complete disappearance of SiO₂ counting from the beginning of the Si substrate appearance (see Figure 3.20) [108]. The estimated sputtering rate is approximately 8 nm per minute with $\Delta x \approx 4$ nm, for an incident beam energy of 3 keV. The estimation of sputtering rate was done also for an incident beam energy of 1 keV, for this beam energy the sputtered rate is approximately 1.5 nm per minute.

In this Chapter a short presentation of experimental conditions and the characterization of measuring set-ups used in determining sensing, electronic and chemical properties has been given. The next Chapter will deal with the results of chemical status investigations as well as the results of rigorous analysis of electronic properties. Results of the study of sensor behaviour and characteristics will be also presented. Additionally, investigation results of the quality of ohmic contacts will be shown.

Chapter 4

Results and discussion

In this Chapter the results of studies performed within the presented Thesis are given and discussed. Firstly, the standard approach for quantitative analysis of gas action on n-InP is presented with its advantages and simplifications. The fundamental limitation is a simplified assumption about the negligible influence of the initial chemical and electronic state of the semiconductor surface on the adsorption process [23,27]. Therefore the main target of this Thesis is thorough study of the chemical and electronic properties of the n-type InP epitaxial surfaces to better understand the mechanism of gas action on these surfaces.

In this work, the electronic parameters of n-InP epitaxial layers, i.e., the charge carrier concentration and mobility, both before and under oxidizing gas action (NO_2 , O_3) are studied by means of the adapted Van der Pauw method in Hall effect measurement. Furthermore, the theoretical analysis based on rigorous computer calculations are carried out in order to characterize the influence of surface states on the near-surface region and layer conductivity. The chemical properties are studied by means of surface techniques, i.e., X-ray photoelectron spectroscopy and Auger electron spectroscopy combined with ion sputtering. The Atomic force microscopy of the n-InP and ohmic contact surface is used to establish their roughness. The scanning electron microscopy images of the contact region are also given. The sensing properties have been tested in terms of sensitivity, response time, influence of active layer thickness, influence of temperature, sensor response stabilization at very low gas concentrations (less than 50 ppb).

4.1 NO_2 action on InP surface

In previous works Talazac et al. [26,27,32,33,34,35] proposed that as NO_2 is an oxidizing gas having one unpaired electron, so, its action consists of a capturing electrons by gas molecules from the semiconductor bulk and creation of the depletion layer. The action of NO_2 at the semiconductor surface is described

by the adsorption law (see Section 2.4). If one assumes that the distribution of active sites is not uniform and that active sites are not energetically equivalent, then the adsorption process may be described by the Freundlich isotherm empirical law (see Equation 2.16). After gas desorption, the layer resistance goes back to its initial stable level, so that the gas desorption may be considered as complete.

In conclusion, when the adsorbed gas molecules and the semiconductor are in thermal equilibrium, the depletion layer W may be described as a function of coverage rate of gas molecules Θ and it is given by Equation 4.1. To obtain the relationship between W and gas concentration C the Freundlich isotherm (see Section 2.16) is used as follows:

$$W = f(\Theta) \quad (4.1)$$

$$W = f(p_1 \cdot C^m) \quad (4.2)$$

which gives:

$$W = p_2 + p_3 \cdot \ln(C) \quad (4.3)$$

where p_1 , p_2 and p_3 are the constants.

Furthermore, in this model it was assumed that the changes in conductance, due to gas action, are caused by changes of the active layer thickness d due to a creation of the depletion layer with a thickness W . Taking into account Equation 2.19, the InP layer relative conductance changes are as follows:

$$\frac{\Delta G}{G_{initial}} = \frac{W}{d} \quad (4.4)$$

where ΔG is given by Equation 4.5; $G_{initial}$ is the initial conductance of the sample and G_{gas} is the conductance under gas adsorption.

$$\Delta G = |G_{gas} - G_{initial}| \quad (4.5)$$

$$G_{initial} = \frac{\sigma \cdot c \cdot d}{a} \quad (4.6)$$

$$G_{gas} = \frac{\sigma \cdot c \cdot (d - W)}{a} \quad (4.7)$$

where c and a are sample dimensions as it is shown in Figure 2.9.

It may be assumed that the creation of the depletion layer, resulting from the gas adsorption, can be considered as a limited process. From this conclusion, the relation between W and C can be given by the logarithmic function:

$$\frac{\Delta G}{G_{initial}} = \frac{p_2 + p_3 \cdot \ln(C)}{d} \quad (4.8)$$

$$\frac{\Delta G}{G_{initial}} = A + B \cdot \ln(C) \quad (4.9)$$

Therefore, taking into account Equation 2.20 the relative resistance changes as a function of gas concentration are expressed by the following relationship:

$$\frac{R_{gas} - R_0}{R_{gas}} = A + B \cdot \ln(C) \quad (4.10)$$

where A and B are characteristic parameters of the system under consideration (an adsorbed gas molecule and a semiconductor surface).

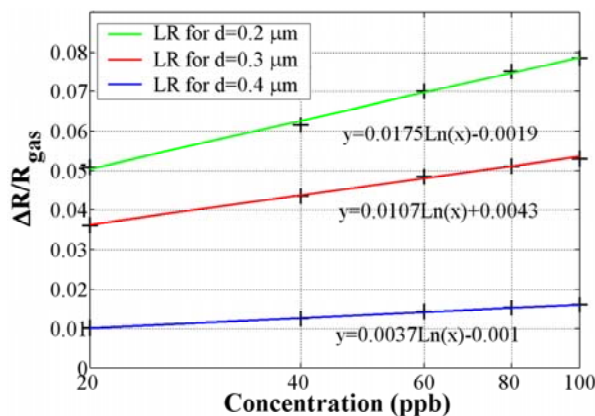


Figure 4.1: *Measured sensitivity (points) of InP sensors with different active layer thickness (d) to NO₂ action at 80 °C and best-fit curves (linear regression).*

This approach has been used in this Thesis for the quantitative description of the results of measurements of the stabilized InP sensor responses to NO₂ at 80 °C versus gas concentration for different InP layer thickness. The measured dependencies of the sensor sensitivity versus NO₂ concentration are shown in Figure 4.1. They are compared with the best-fit logarithmic curves calculated from Equation 4.10, which describes phenomenologically the character of changes in the experimental data. The values of the A and B constants appearing in Equation 4.10 are given in Table 4.1.

The applied phenomenological model of the resistance changes upon gas action is largely used in gas sensor research [24,27,32]. However, this model is very simplified and does not take into account such an important factor like the initial chemical and electronic state (native oxides, surface states) of the

surface before gas adsorption. According to literature, e.g., H. Hasegawa et al. [37], the semiconductor surface covered by native oxides is characterized by a high density of surface states, which are responsible for many undesirable effects like Fermi level pinning and existence of depletion layer on n-InP. Thus, in this work the chemical and electronic properties of the InP surface are studied to get more realistic characterization of the active layer and to understand better the gas action on InP surface. Also, the investigation of ohmic contact quality and possible influence on the sensing n-InP mechanism are studied in this work.

Table 4.1: *A and B characteristic constants for adsorption process.*

Thickness (μm)	A	B
0.2	- 0.0019	0.0175
0.3	0.0043	0.0107
0.4	- 0.001	0.0037

4.2 Ohmic contacts

Ohmic contacts were realized as explained in Section 3.1.2. To eliminate the influence of contacts on sensing mechanism of InP, the contact were covered by varnish. The structure with covered contacts was exposed to gas and its response was registered as previously explained. Experimental results show that sensors with varnished or unvarnished contacts exhibit the same sensitivity and response time.

Despite the fact that the gas does not react directly at the ohmic contact, the process of contact fabrication and the quality of its results strongly affects the sensor characteristics. High quality ohmic contacts are needed during the sensing parameters tests, especially when performing Hall effect measurements. To assess quality of ohmic contacts, their specific resistance was estimated (see Section 2.5.2). The estimation of the resistance of our contact is done using a sample with a n-InP layer thickness of $0.2 \mu\text{m}$ with contacts evaporated as shown in Figure 3.2. The estimated contact resistance is equal to 270.6 Ohm.

4.2.1 AES in-depth profile

The quality of ohmic contact realization is also tested in terms of the chemical composition of the contact by means of depth profiling. Figure 4.2 shows the depth profile of the contact as a function of a sputtering time. This Figure depicts the component relative concentrations versus sputtering time. It can be seen that our contact consists mainly of gold and germanium and the signals of carbon and oxygen contaminations are negligible. This gives complementary evidence of the high quality of the contacts.

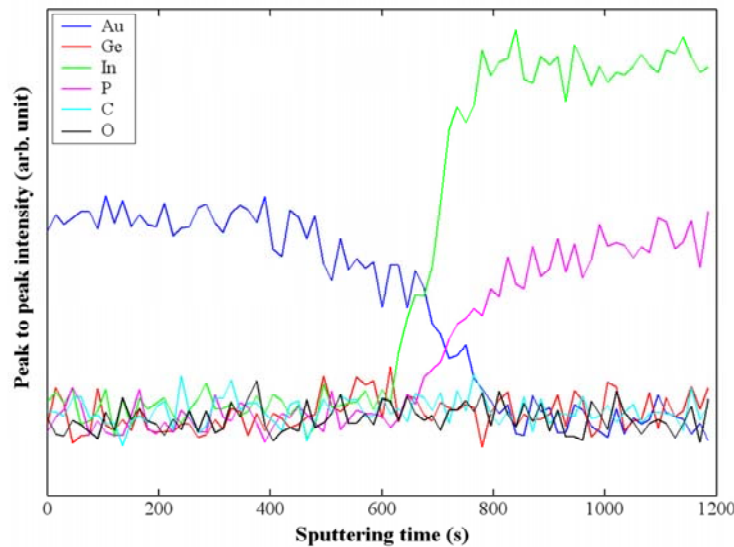


Figure 4.2: *Ohmic contact elemental composition in-depth profile from AES analysis.*

4.2.2 AFM image analysis

Using Atomic Force Microscopy analysis, the height of ohmic contact on the n-InP surface is estimated to 135.7 nm (see Figure 4.3). From this Figure it may be found that around 45 % of the evaporated metal thickness diffuses into the InP layer, however this value can vary with the contact area. This diffusion is possible by implicating annealing process in the contact realization. The contact metal diffused into the sample creates in the semiconductor an area more doped than that the bulk, which is a principle of ohmic contact fabrication.

Since the annealing process seems to be very important in ohmic contact technology, its influence on the surface RMS (RMS: Root Mean Square) roughness of ohmic contact surface is also investigated. In Figure 4.4 a sample before annealing is compared with one after annealing. The contact surface RMS roughness for the non-annealed sample is equal to 9.4 nm and for the annealed one to 3.9 nm. These results show that annealing ameliorates the diffusion of the deposited metals in the InP layer and homogenize the surface of the ohmic contact.

4.2.3 SEM image analysis

Figure 4.5.a. is a SEM photo of our contact showing the boundary between the sample and the contact surface. The existence of evaporated metals is only observed on the contact surface and the contact-InP boundary is well marked. This shows that the metal evaporation and deposition process resulted in the

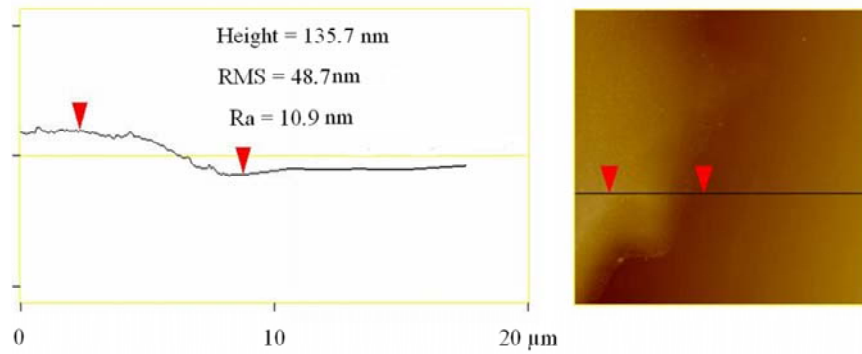


Figure 4.3: *AFM image of the boundary between n-InP surface and contact area.*

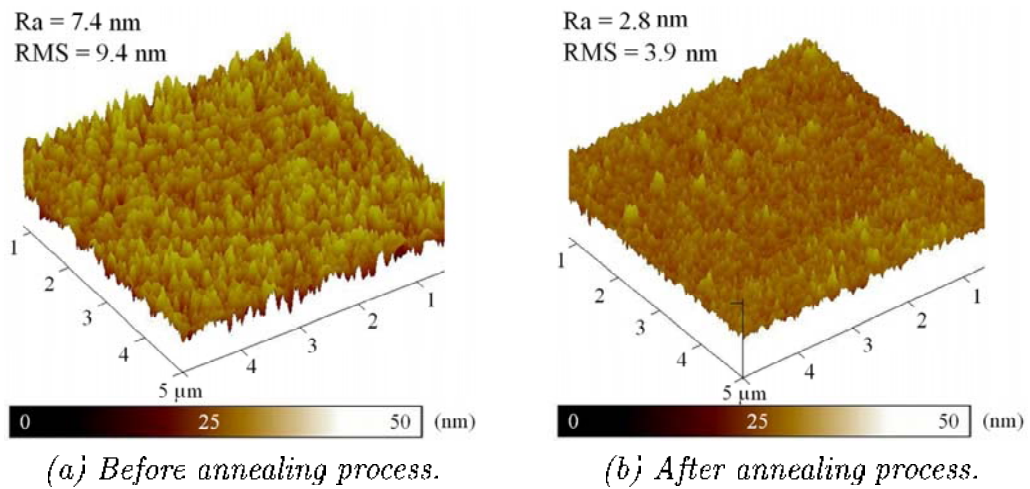
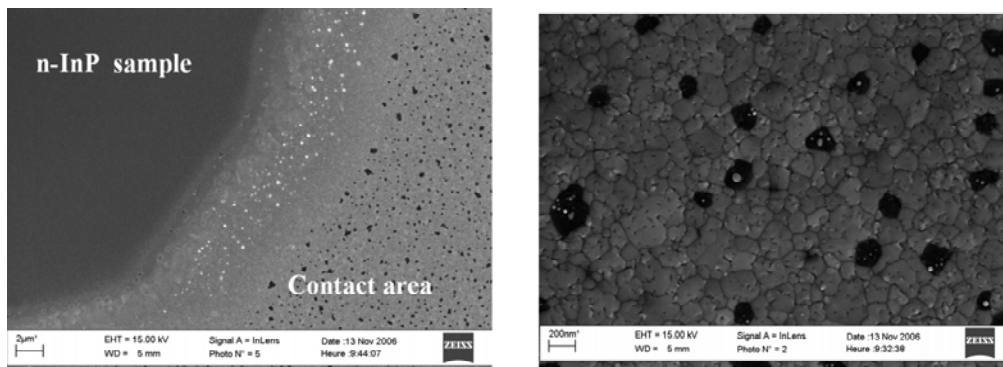


Figure 4.4: *AFM images of ohmic contact surface.*



(a) *Boundary between contact and n-InP surface.* (b) *Morphology of the contact surface.*

Figure 4.5: *SEM images.*

desired contact geometry and that the stainless steel mask used during this process was well adapted to the task. Moreover, the image of contact morphology was realized as it is shown in Figure 4.5.b. The obtained morphology image well shows that our contact surface is uniform.

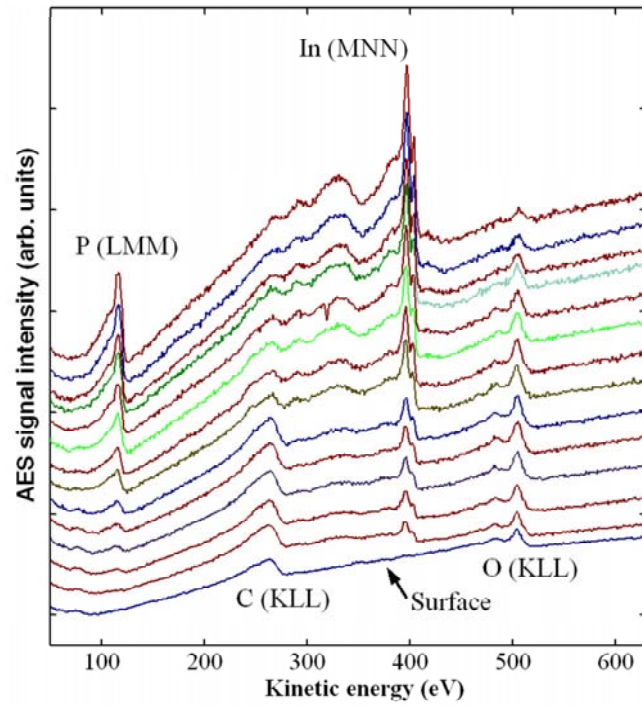
4.3 Chemical properties of n-InP surfaces

The aim of the chemical analysis is to estimate the chemical state of the n-InP surface before and under gas action. It should be noted that the studied surfaces are affected during the ohmic contacts fabrication by annealing process (in vacuum, at temperature of 300 °C). The analysis of annealing influence on the chemical state is already well studied [28,74,79], but the analysis of annealing process influence was never performed on our samples (n-InP epitaxial layer from IEMN). According to literature, during the annealing process the carbon contamination appears on the pure InP layer and the layer of phosphorous oxides develops. Thus, the XPS and AES analysis of the InP based sensor surfaces after annealing process are carried out. Moreover, the Ar⁺ ion sputtering technique combined with AES spectra registration is used to obtain in-depth elemental composition profile of InP near surface region.

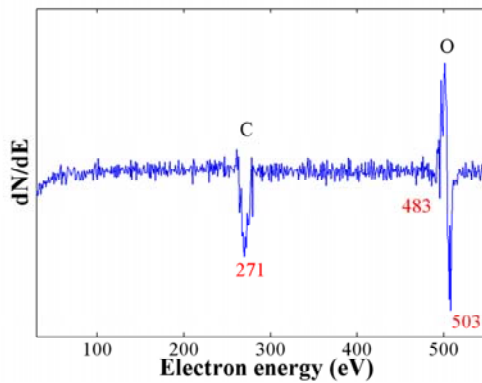
4.3.1 Auger results

The AES microscopy study, combined with in-depth profiling was performed in terms of both qualitative and quantitative analysis of the chemical composition of InP epitaxial surfaces and near-surface region. For AES experiment, as it is written in Chapter 3, the Physical Electronics PHI 600 Scanning Auger Microprobe was used. The base pressure in the analysing chamber during collecting the AES spectra was $4 \cdot 10^{-9}$ Torr. Experiments were done for different primary electron energies from 3 to 10 keV that allowed to obtain the best results and minimize artifacts of artifacts. The incident angle of the electron beam with respect to the normal to the surface was 30 ° and the sample current was 10 nA. The in-depth profiling of InP epitaxial layers was realized using the scanning Ar⁺ ion gun with an energy of 3 keV and 1 keV, for result comparison. The ion gun was inclined at about 50 ° with respect to the normal.

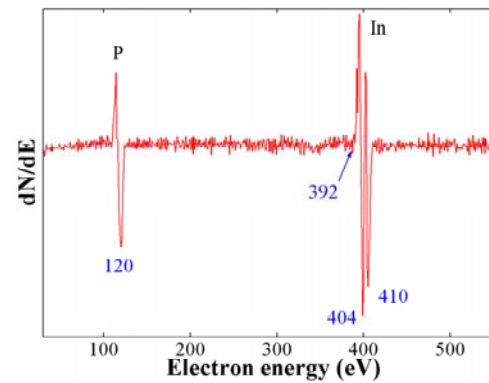
AES spectra registered from InP sensor surfaces after ohmic contact fabrication and before gas action are summarized in Figure 4.6. These spectra consist of P peak (LLM transmission), In peak (MNN), C and O peaks (KLL). Figure 4.6.a depicts the Auger spectra as a function of the progressive surface sputtering (duration of 1.2 s). The first spectrum (at the bottom) represents the sample surface before the sputtering process. Then, the sample is submitted to sputtering cycles 1.2 s each, and after each an Auger spectrum is taken. From the first sample spectrum, it can be observed that the InP surface is initially totally covered by carbon and oxides. Then, after 1.2 s of Ar⁺ sputtering, the



(a) AES spectra versus Ar^+ ion sputtering time.

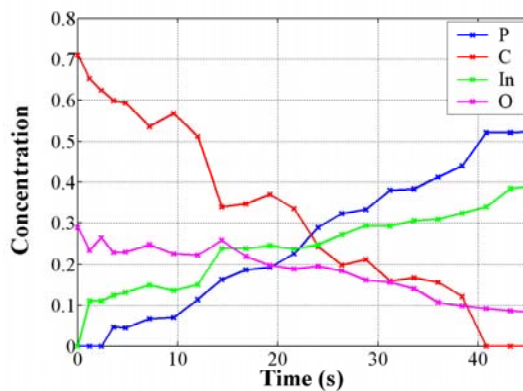


(b) Before the Ar^+ sputtering.

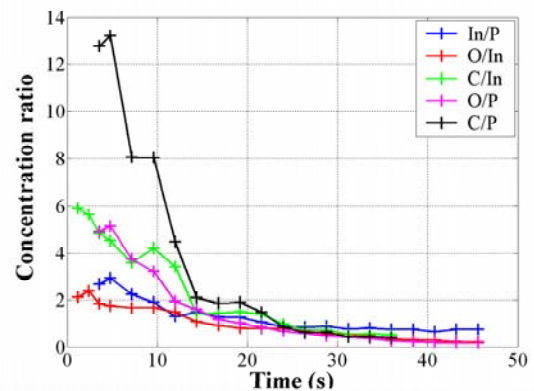


(c) After the Ar^+ sputtering cycle.

Figure 4.6: Measured AES spectra versus Ar^+ ion sputtering.



(a) Relative concentrations.



(b) Concentration ratios.

Figure 4.7: Relative concentrations and concentration ratios for different elements as a function of InP sputtering time.

indium peak appears. After around ten sputtering cycles, the phosphorus peak can be observed while the C peak almost disappears.

For quantitative analysis of the surface chemical composition a derivation of the measured AES spectra was made, which results in what is termed 'peak-to-peak' graphs. In Figures 4.6.b and 4.6.c, examples of peak-to-peak graph are shown. Thus, using data from these Figures, Equation 3.19 and Table 3.1 relative concentrations of each element may be estimated. Figure 4.7.a displays the relative concentrations of atoms for each sputtered spectrum. It may be observed quite clearly, that on the InP surface there is only oxide and carbon contamination layer and after 25 s of sputtering, relative concentrations of P and In are much bigger than the ones of other components. It can be observed that at the surface, the In concentration is much bigger than for P with a coefficient 3. However, after a number of sputtering cycles the peak of P atom evidently appears.

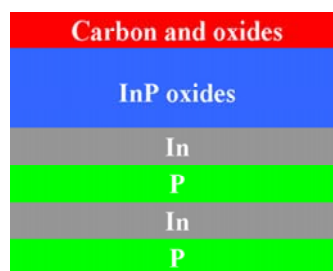


Figure 4.8: *Layered model of InP sample.*

In Figure 4.7.b, the concentration ratios of components are presented. In this Figure three areas can be estimated, the first one with a great amount of carbon (the range from 0 to 15 s of sputtering), the second one (from 15 to 24 s) where after the fast disappearance of carbon, its quantity is much smaller and the third one (< 24 s) where the ratio of the In/P tends toward 1 that is the normal value for the InP bulk. Therefore, in Figure 4.8, the assumed from the AES results, layered model of a sample structure is presented. It consists of a carbon and oxide contamination layer, a continuous layer of InP oxides and non-continuous alternate layers of In and P from InP. It should be stressed here again that InP oxides layer starts with In oxides what is evident from Figure 4.6.a. Using the information from the Figures 4.6 and 4.7, the average concentration after a sputtering time of 45 s can be obtained, they are collected in Table 4.2.

Table 4.2: *Average atomic concentration for 45 s of sample sputtering.*

Atom	Concentration (%)
In	20
P	24
O	21
C	35

4.3.2 XPS results

The XPS spectrometer used in this study and described in Chapter 3 is equipped with a MgK α X-ray source (1253.6 eV) and a hemispherical analyser.

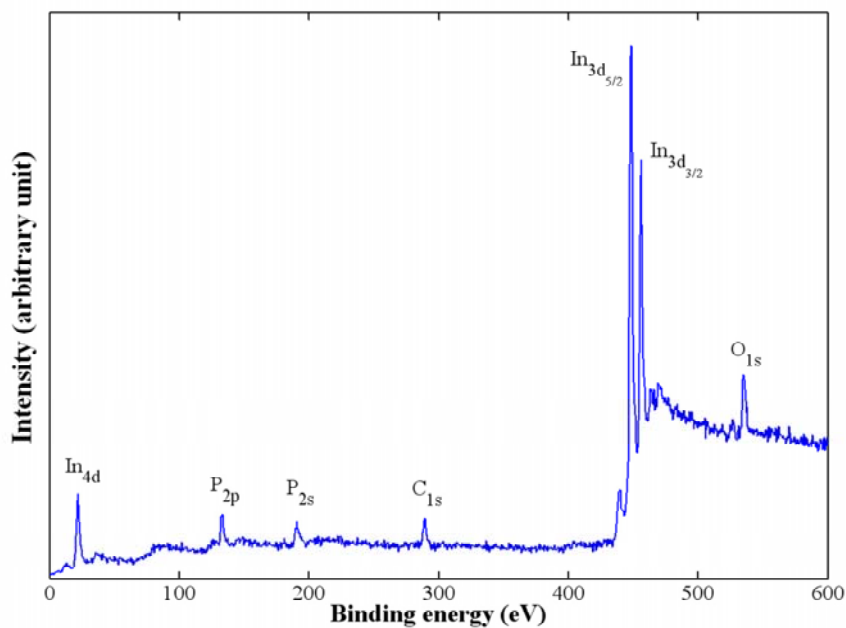


Figure 4.9: General spectrum.

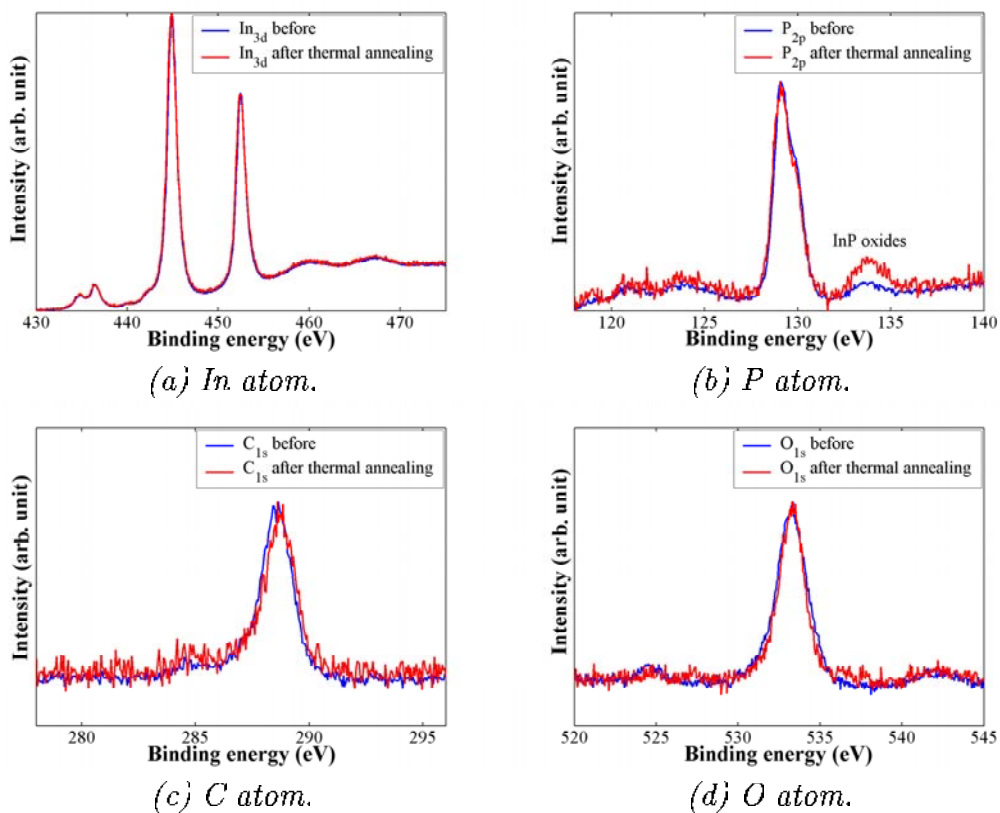


Figure 4.10: Changes in peaks after the annealing process.

The constant pass energy used was of 20 eV for high-resolution narrow scans and 50 eV for low-resolution wide scans [93,107]. The n-InP spectra have been collected for an active layer thickness of 0.2 μm . The collected general spectrum from (100) n-InP epitaxial surface is typical of the ones obtained from (100) InP surfaces. Figure 4.9 shows the general spectrum from n-InP that consists of peaks of phosphorus (P_{1p} , P_{2p}), indium (In_{3d} , In_{4d}), oxygen (O_{1s}) and carbon (C_{1s}). From the zoom on certain peaks show that after thermal annealing in hydrogen, changes in XPS peaks are observed. In Figure 4.10, it can be observed that significant changes appear in InP oxide peak from zoom on P_{2p} ; it means that probably the P oxide layer develops due to annealing. The shift of the C_{1s} is also due to annealing process. The peak O_{1s} seems to be thinner after annealing, but the decomposition of this peak did not give a strong prove that it is only due to P oxides development. No significant changes in peak In_{3d} are observed.

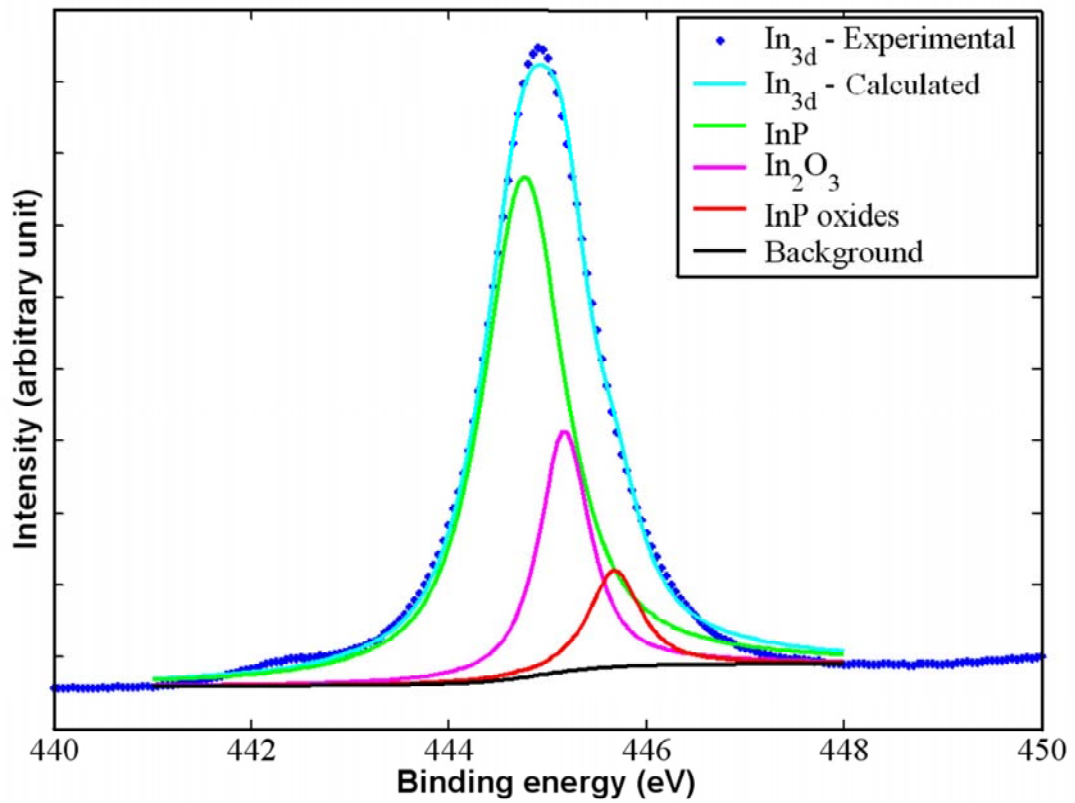
From Figure 4.10, the existence of the well developed oxide layer is evident. Therefore, a detailed analysis of the chemical composition of In and P peaks has been performed. Figure 4.11 gives the detailed deconvolution spectra analysis of the P_{2p} and In_{3d} , collected from as received InP sensors (i.e., the surface has not been exposed to gases). The P_{2p} core level spectra exhibit two pairs of peaks:

- the peaks at low binding energy (BE–129.15±0.2 eV, FWHM=1.2±0.1 eV) consists of the spin-orbit splitting and branching ratio $2p_{3/2}/2p_{1/2}$ being fixed respectively at 1.2 eV and 2.2.
- the peaks at high binding energy (BE–133.85±0.2 eV, FWHM=1.4±0.1 eV) can be assigned to an InP peak, and a mixture of surface InP oxides (mostly P_2O_5).

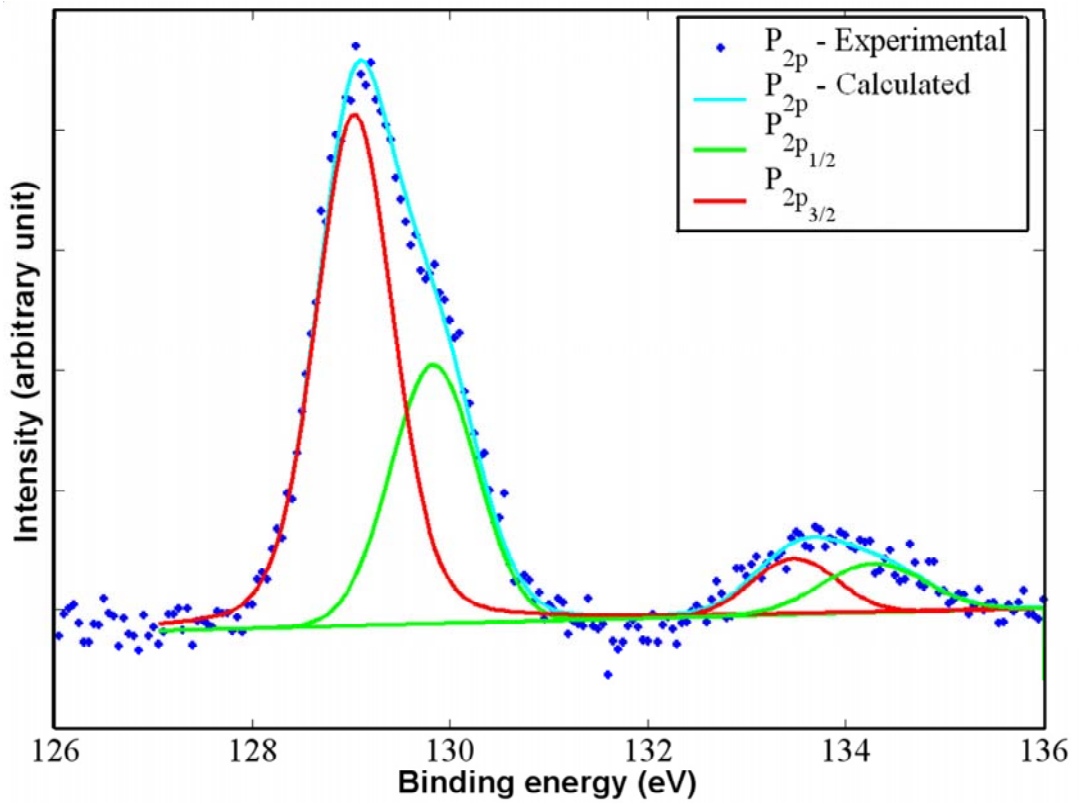
The $In_{3d_{5/2}}$ core level spectra can be fitted with two peaks assigned to:

- InP (BE–444.76±0.2 eV, FWHM=0.98±0.1 eV);
- In_2O_3 (BE–445.17±0.2 eV, FWHM=0.61±0.1 eV);
- InP oxides (BE–445.7±0.2 eV, FWHM=0.61±0.1 eV); it can be assigned to all the other existent oxides on the InP surface.

So, the XPS results in terms of peaks position are in good accordance with literature [110]. Moreover, the oxide layer was characterized as In_2O_3 (probably on the top, see results of AES in Figure 4.6.a.), InP oxides (a mixture of In and P oxides), P_2O_5 .



(a) $In_{3d_{5/2}}$ peak.



(b) P_{2p} peak.

Figure 4.11: Decomposition of chosen XPS spectra.

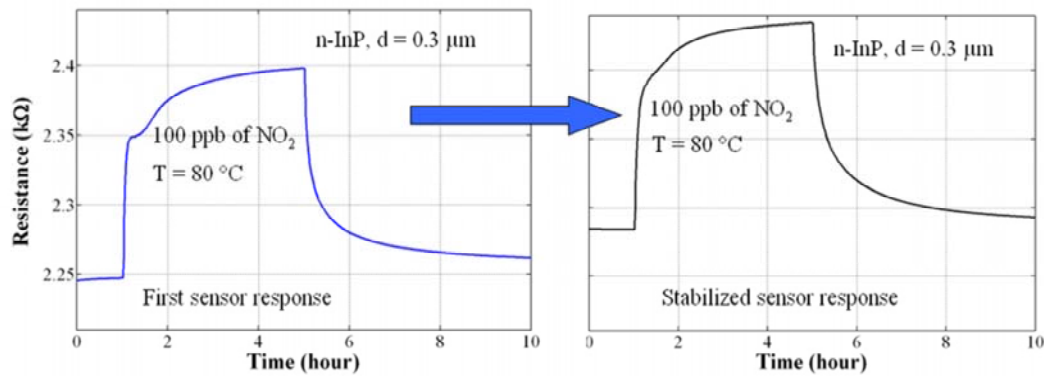


Figure 4.12: Gas sensor response stabilization phenomena, due to 100 ppb of NO_2 , at 80°C for the epitaxial layer thickness of $0.3\ \mu\text{m}$.

4.3.3 Quantitative analysis of XPS

As NO_2 is a strongly oxidizing gas, it can provoke changes in chemical surface state. During our studies, it was observed that the sensor response develops up to the stabilization as a function of NO_2 exposures. Figure 4.12 displays two sensor responses of the same gas sensor device of epitaxial layer thickness equal to $0.3\ \mu\text{m}$, working at 80°C . The first graph represents the sensor response due to first gas exposure, while the second one represents the stabilized gas sensor response due to 6 exposures of 100 ppb of NO_2 , every exposure durated 4 hours. This phenomenon may be explain by the surface state stabilization in terms of native oxide layer changes. Thus, to estimate its changes, a procedure based on the quantitative XPS analysis (see Section 3.4.5) and the Auger results was developed.

From the obtained AES and XPS results it follows that the sensor structure consists of the outer layer (a carbon and oxide contamination layer), a continuous layer of InP oxides and non-continuous alternate layers of In and P (see Figure 4.8). Thus, taking into account attenuation layers for following components and Equation 3.16, the photoelectron path can be determined. Namely, In and P peaks originate partly from InP and InP oxide layers; detected photoelectrons of these peaks are attenuated by the continuous layer of InP oxides and by the carbon and oxide layer. The oxygen

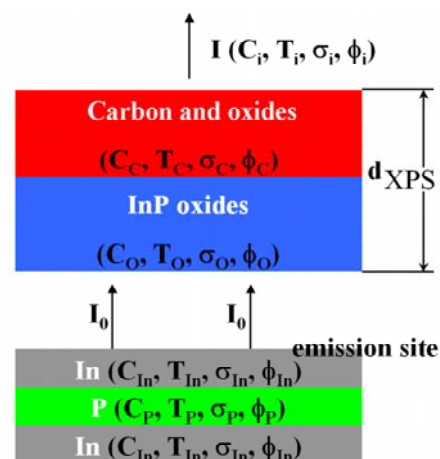


Figure 4.13: Schema of the XPS analysis principle.

peak originates from the continuous layer of InP oxides and is attenuated by the carbon layer. Finally, the carbon peak results from the surface layer emission. Figure 4.13 displays the path of the photoelectrons from the emission site to the surface, where they are collected. In conclusion, peak intensities of In and P consist of the signal coming from the alternate In-P layer. In addition, they are attenuated by a continuous layer of oxides and carbon. The peak intensity of O consists of the signal coming from continuous oxide layer and is attenuated by the carbon layer. The peak intensity of C is coming from the top of the surface. So, photoelectron peak intensities I (Equation 3.16) for every constituents are given by following equations:

$$I_{In} = \phi_{In} \cdot \frac{\delta_{monolayer} \cdot T_{In} \cdot \sigma_{cs_{In}}}{1 - e^{\frac{-d_{XPS}}{\lambda_{In/InP}}}} \cdot e^{\frac{-d_{XPS}}{\lambda_{In/InP}}} \cdot e^{\frac{-d_C}{\lambda_{In/C}}} + \phi_{In} \cdot C_{In} \cdot T_{In} \cdot \sigma_{cs_{In}} \cdot \lambda_{In/InP} \cdot \left(1 - e^{\frac{-d_{XPS}}{\lambda_{In/InP}}}\right) \cdot e^{\frac{-d_C}{\lambda_{In/C}}} \quad (4.11)$$

$$I_P = \phi_P \cdot \frac{\delta_{monolayer} \cdot T_P \cdot \sigma_{cs_P}}{1 - e^{\frac{-d_{XPS}}{\lambda_{P/InP}}}} \cdot e^{\frac{-d_{XPS}}{\lambda_{P/InP}}} \cdot e^{\frac{-d_C}{\lambda_{P/C}}} + \phi_P \cdot C_P \cdot T_P \cdot \sigma_{cs_P} \cdot \lambda_{P/InP} \cdot \left(1 - e^{\frac{-d_{XPS}}{\lambda_{P/InP}}}\right) \cdot e^{\frac{-d_C}{\lambda_{P/C}}} \quad (4.12)$$

$$I_O = \phi_O \cdot C_O \cdot T_O \cdot \sigma_{cs_O} \cdot \lambda_{O/O} \cdot \left(1 - e^{\frac{-d_{XPS}}{\lambda_{O/O}}}\right) \cdot e^{\frac{-d_C}{\lambda_{O/C}}} \quad (4.13)$$

$$I_C = \phi_C \cdot C_C \cdot T_C \cdot \sigma_{cs_C} \cdot \lambda_{C/C} \cdot \left(1 - e^{\frac{-d_C}{\lambda_{C/C}}}\right) \quad (4.14)$$

where $\delta_{monolayer}$ is the thickness of one monolayer and d_{XPS} can be described by the layer thickness that attenuates the signal (like d_C is a thickness of carbon layer) or by the information depth. In addition, σ is the cross section and T is the analyser transmission.

For the simplification of the analysis, the following assumptions are made:

$$\phi_i = \phi \quad \forall i \quad (4.15)$$

$$\Theta_i = \Theta \quad \forall i \quad (4.16)$$

The other data used in the analysis are given in Table 4.3. To establish this model, ratios between the signal peak area of all the elements constituting our

structure (In/P, In/O, P/O or In/C, P/C, etc.) are used. These ratios are given in Table 4.4. The signal depends strongly on the depth of the emission site d . Therefore, simulated signal ratios are for different depths, ranging from 0 to 5 nm. Through comparison of experimental ratios of signal peak area with results of simulations, the element concentrations used in simulations was as from AES measurements (In - 20%, P - 24%, O - 21%, C - 35%). So, the evaluation of the depth for which all theoretical ratios are in agreement with experimental ones was done. This depth corresponds to the sum of thicknesses of the InP-oxide layer and carbon and oxide contamination layer. It should be noted, that from AES profiles the oxide and carbon layer seems to disappear continuously with the sample depth while in our modelling a layered near-surface structure to make the calculation possible was assumed. The chemical composition

Table 4.3: *Data used in XPS analysis for each near-surface constituent.*

Constituent	σ_{cs}^*	λ (nm)	$T \cdot 10^{-3}$ (eV ^{-1.5})
In/InP	22.43	1.85	4.48
P/InP	1.35	2.46	2.67
O/O	2.85	1.78	5.14
C/C	1.00	2.00	3.29
In/C	22.43	2.26	1.36
P/C	1.35	3.09	0.81
O/C	2.85	2,25	1.56

*photoionization cross section for MgK α
in units of the C_{1s} cross section of 22000 barns

Table 4.4: *Experimental peak ratios used in XPS analysis.*

Constituents	Peak ratio before	Peak ratio after NO ₂
In/P	26.75	22.38
In/O	9.97	7.45
P/O	0.37	0.33
In/C	41.18	31.61
P/C	1.59	1.41
O/C	4.13	4.24

changes due to the gas action were observed to be over when a stable gas sensor response was obtained. The experiment with gas was realized in cycles of gas exposures of 10 hours each. After every exposures the XPS study was performed. The obtained changes in component thicknesses and concentrations were observed to be over after 50 hours of gas action at ambient temperature, that is in good accordance with gas sensor response stabilization observed at 80 °C (temperature may improve the process). The results of the XPS analysis are given in Tables 4.5 and 4.6. Table 4.5 presents the constituents concentration for

Table 4.5: *Results of concentration changes due to gas action.*

Constituent	Concentration %	
	before	after NO ₂
In	20	23
P	24	30
O	21	25
C	35	22

Table 4.6: *Results of thickness changes due to gas action.*

Constituent	Thickness (nm)	
	before	after NO ₂
InP oxides	3	3.3
C	1.4	0.7

as-received sample and working as a gas sensor one. In Table 4.6 the thickness changes in oxide and carbon contamination layers before and after gas action are collected. Before gas action, the XPS analysis gave us the thickness of oxide layer around 3 nm, with the depth of carbon and oxide contamination layer equal to 1.4 nm, which seems to be in agreement with AES measurements, on 'as-received' samples. In simulations of the XPS signal intensity for the sample after the gas action, assumed component concentrations change being as following: In 23%, P 30%, O 25%, C 22%. For these concentrations found, the oxide layer thickness is about 3.3 nm. Furthermore, after exposure to gas, the carbon layer seems to be twice smaller than that before (around 0.7 nm) [22]. It should be mentioned here that the same results of native oxide layer thickness (around 3 nm) was found by the elipsometry technique [non published results realized by Dr M. Mihailovic in LASMEA]. Also by elipsometry after exposure to ozone, we did not observed the great change in oxide layer thickness, it also proves the stability of the InP oxide layer.

4.3.4 AFM images

Changes in the native oxide layer were also studied in terms of surface RMS roughness. In Figure 4.14, images of the InP surface and characteristic parameters for AFM analysis like RMS and average surface roughness (Ra) are presented. These Figures show the n-InP surface before and after gas action. The surface RMS roughness analysis evidently shows the changes in surface roughness due to the gas action. Before the gas action, the RMS roughness is equal to 0.430 nm. After gas exposures up to the sensor response stabilization, the RMS roughness is equal to 0.771 nm. These results also verify the assumption that the oxidizing gas exposure causes changes in the surface structure.

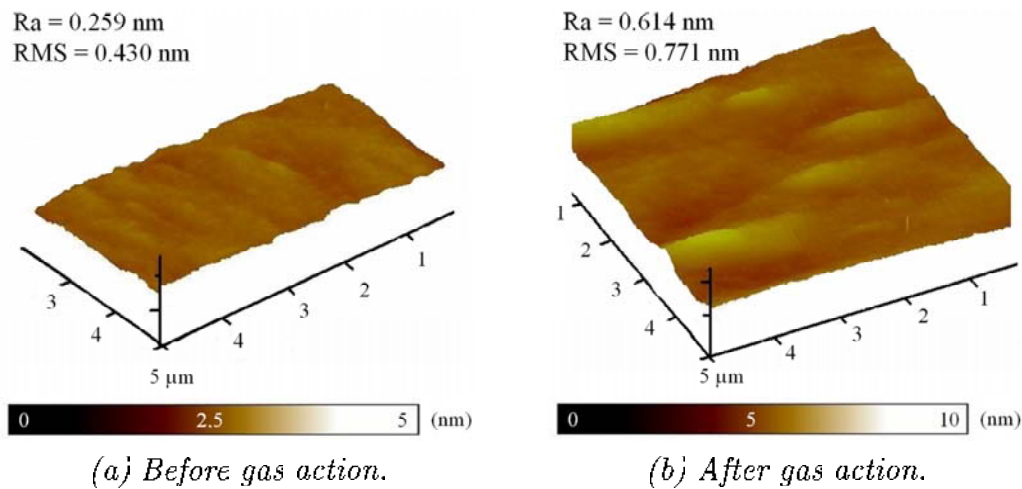


Figure 4.14: AFM images of the n-InP surface.

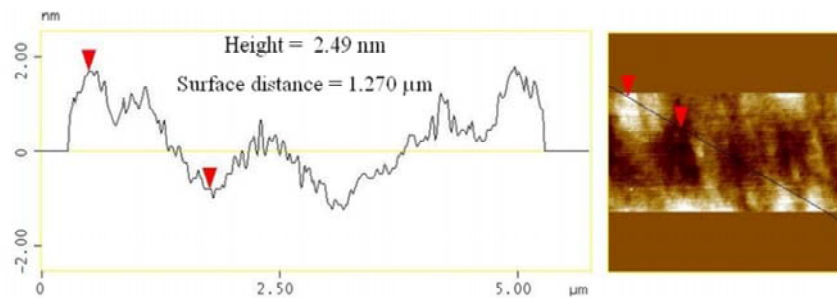
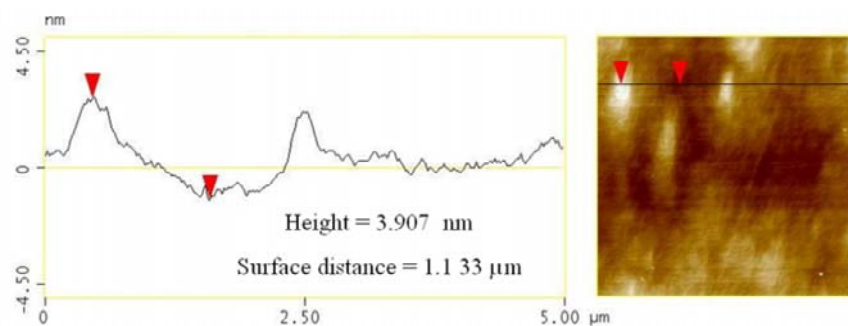
Figure 4.15: AFM image of the n-InP surface before NO_2 action.

Figure 4.16: AFM image of the n-InP working sensor.

Figures 4.15 and 4.16 display the additional analysis of the n-InP surface before and after gas action. From these Figures the existence of sloped objects on the InP surface is observed. Changes in the surface of an as-received sensor and already working one can be also observed. The changes are visible in the heights of the sloped objects and in their forms being smoother for the structure exposed to NO_2 .

4.4 Studies of electronic properties

In the previous section the existence of a complex system of InP-related native oxides on InP epitaxial surface was proved. From literature the existence of oxide layer causes the high density of surface states that was found to be equal (in the minimum) about to $10^{12} \text{ eV}^{-1} \text{ cm}^{-2}$ in the case of InP [28]. The U-shaped continuum of surface states related to structural disorder, which is distributed at the native oxide-InP interface determines the amount of charge captured at the interface from the InP bulk and thus, the initial surface band bending and the depletion layer width. On the other hand, the electrically active interface influences the gas molecule adsorption. Therefore, it is important to characterize the surface electronic properties in order to understand better the mechanism of the epitaxial n-InP layer conductivity and the gas sensing process. Furthermore, from the studies of the influence of surface states on the electronic properties of InP epitaxial layer, i.e., interface band bending and Fermi level position, as well as on layer resistance with respect to the layer thickness, doping and temperature, the important information for sensor technology can be obtained.

Within this Thesis, the electronic properties of InP layers were studied by means of rigorous calculations and Hall effect measurements. In the calculations, the system consisting of the native oxide thin film and InP epitaxial layer is represented by the continuous interface states with the density distribution $N_{SS}(E)$ as described in Chapter 2 (DIGS model).

4.4.1 Principle of rigorous analysis

Calculations were performed using a computer simulator developed by T. Saitoh et al. [31,111]. This simulator uses a one dimensional Schrodinger-Gummel-type vector matrix algorithm, for self-consistent solving of Poisson's equation, current equations and continuity equations for electrons and holes. As a result, the electron $n(x)$ and hole $p(x)$ concentrations as well as potential $V(x)$ as a function of the distance from the surface x are obtained. The surface position of the Fermi level E_F as well as the layer resistance are also calculated.

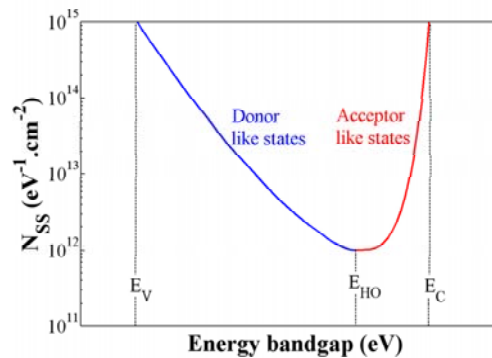


Figure 4.17: Surface state energy distribution $N_{SS}(E)$ at InP surface assumed in calculations.

In these calculations, the boundary conditions are defined by the surface electric field that depends on the

surface state energy contribution $N_{SS}(E)$ and the surface fixed charge Q_{FC} :

$$E_s = f(N_{SS}(E), Q_{FC}) \quad (4.17)$$

For modelling the interface states energy distribution, the U-shaped DIGS spectrum in the energy gap is assumed. It is calculated from Equations 2.11 and 2.12. Its graphical representation is shown in Figure 4.17. The data used in calculation are given in Table 4.7. It consists of the donor-like surface states (positively charged if they are empty, and neutral if occupied) distributed below the so-called ‘charge neutrality level’ E_{HO} and the acceptor-like surface states (neutral if empty, and negatively charged by electrons taken from the conduction band if occupied). The position of the E_{HO} level in the energy band gap does not depend on surface treatments or the type of adsorbed molecules. For InP, the E_{HO} level lies 0.37 eV below the bottom of the conduction band E_C [29,37].

Table 4.7: *n-InP bulk and surface parameters at 300 K used in simulation [29].*

Parameter	InP
Band gap E_g (eV)	1.35
Electron effective mass m_n/m_0	0.077
Hole effective mass m_p/m_0	0.64
Dielectric constant	12.4
Charge neutrality level $E_{HO} - E_C$ (eV)	-0.37
Donor distribution parameters E_{0d} (eV); n_d	0.26; 1.4
Acceptor distribution parameters E_{0a} (eV); n_a	0.22; 3.8
Surface states cross section electrons and holes	10^{-16}

4.4.2 In-depth profiles

Results of simulations as well as previous experimental results show that the sensor sensitivity increases with the decrease of the InP active layer thickness [20,23,26]. It means that for thin sample the near-surface region may play a great role in sensing mechanism. The InP surface is characterized by the high density of surface state mostly related to the native oxide-InP interface which is responsible for creation of the depletion layer with a width W in InP. Therefore, samples used as a gas sensor suppose to be rather sensitive to the surface state and as following to the depletion layer width. This is one of the reasons why simulations taking into account the layer thickness d and the doping level N_D have been realized. The other reason is that the results of such analysis can provide important information for InP sensor optimization in terms of d and N_D parameters.

The simulations of the charge carrier profiles in the near-surface depletion region were performed for the n-InP layers with different doping, in dark conditions that corresponds to the experiment. The calculations were done for the n-InP sample with N_{SSc} equal to 0 and for the samples covered by native oxide layer with a typical value of N_{SSc} equal to $10^{12} \text{ eV}^{-1} \text{ cm}^{-2}$. The results of simulations are summarized in Figure 4.18. It is clear that the thin sample with a small doping level will be very sensitive to the depletion layer W . On this basis we are able to determine the thickness of the InP layers for further electrical experiments to avoid a total depletion. In addition, the depletion layer width was calculated using Equation 2.10 (see Chapter 2). The results of calculations are given in Table 4.8. The value of the surface potential V was caused by N_{SSc} of $10^{12} \text{ eV}^{-1} \text{ cm}^{-2}$ and calculated using the simulator.

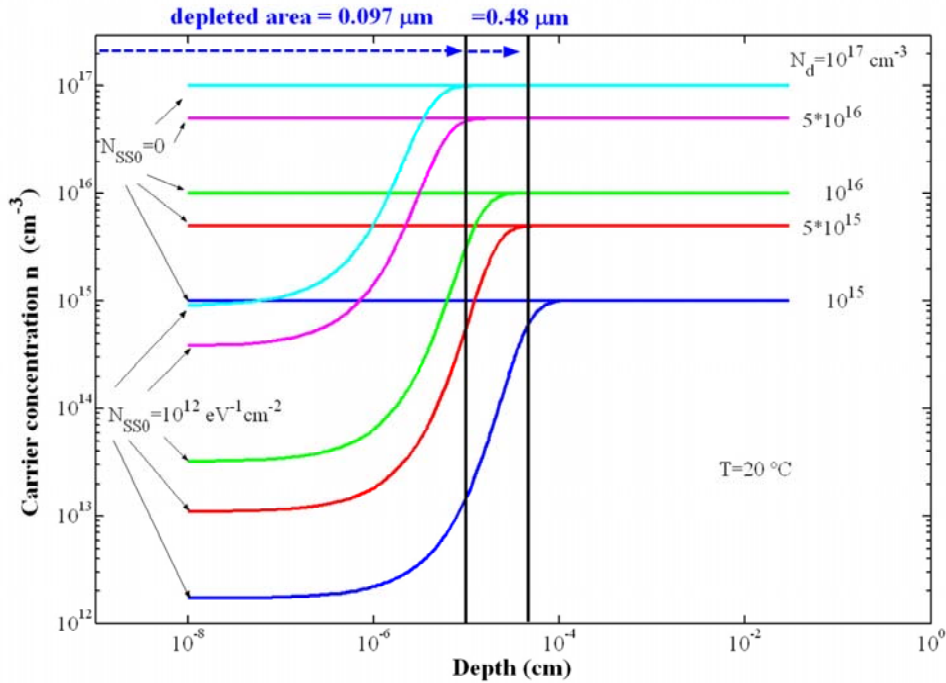


Figure 4.18: Calculated in-depth profiles of the charge carrier density in n-InP layers for different doping level in the case of flat band condition (N_{SSc} equal to 0) and under depletion due to surface states (N_{SSc} of $10^{12} \text{ eV}^{-1} \text{ cm}^{-2}$).

Table 4.8: Calculated W caused by N_{SSc} of $10^{12} \text{ eV}^{-1} \text{ cm}^{-2}$ for different N_D .

N_D (cm^{-3})	W (μm)	$ V_s $ (V)
$1 \cdot 10^{15}$	0.48	0.16
$2 \cdot 10^{16}$	0.097	0.14
$1 \cdot 10^{17}$	0.041	0.12

From this Table one can note that the thickness W changes with N_D by

about one order of magnitude when N_D changes by two orders of magnitudes. Thus, for the further sensor studies samples with the layer thickness from 0.2 to 0.4 μm and the doping level equal to $2 \cdot 10^{16} \text{ cm}^{-3}$ were chosen. For this doping level, the sample thickness should be equal or superior to 0.2 μm , otherwise the depletion layer takes more than 50 % of the active layer thickness.

4.4.3 $N_{SS}(E)$ influence on sensor electronic characteristics

In the case of III-V semiconductors, surface/interface states are responsible for the Fermi level E_F pinning. The barrier height, in the case of strong pinning, is almost insensitive to surface phenomena like ion/gas molecule adsorption. Thus, surface states with a high density may even dominate the phenomenon of resistance changes due to gas action. In conclusion, it seems evident that in gas sensor technology, the key issue in optimization III-V based sensor devices is the control of the density of surface states, Fermi level position and band bending [29]. Therefore, the influence of surface states on the sample resistance R in terms of ratios between R with and without surface states was investigated. Moreover, a rigorous theoretical analysis of the surface Fermi level behaviour as a function of N_{SS_0} was performed. The Fermi level position is calculated as a function of the N_{SS_0} changed from 0 to $2 \cdot 10^{13} \text{ eV}^{-1}\text{cm}^{-2}$.

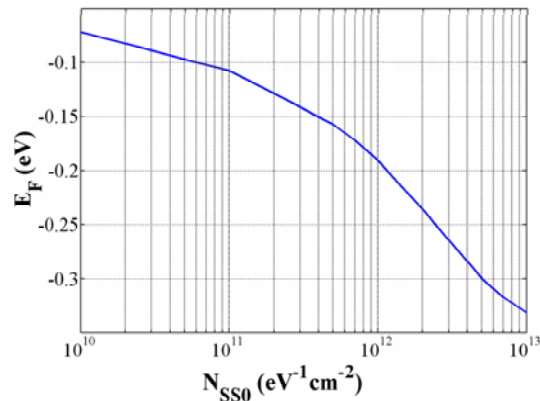


Figure 4.19: *Calculated Fermi level position at InP surface versus minimum density of U-shape surface states (N_{SS_0}) at n-InP surface for $N_D = 2 \cdot 10^{16} \text{ cm}^{-3}$.*

In Figure 4.19, the calculated Fermi level position is presented. As N_{SS_0} increases from low values to $10^{11} \text{ eV}^{-1}\text{cm}^{-2}$, E_F moves from the bulk position towards the charge neutrality level E_{HO} . The energy band bending increases more and more that creates a depletion layer. In the range of N_{SS_0} equal to $10^{12} \text{ eV}^{-1}\text{cm}^{-2}$, a weak inversion develops. Thus, the shift rate of E_F is weaker for small values of N_{SS_0} and E_F approaches asymptotically E_{HO} . This means that the surface Fermi level is strongly pinned around E_{HO} , even if the surface state density increases.

The results of calculations of the relative resistance $R/R_{N_{SS_0}=0}$ versus N_{SS_0} and n-InP film thickness, presented in Figure 4.20, give evidence for the strong influence of surface states on the electronic characteristics for d in the sub-micrometer range. The impacts of the charged surface states give rise to the

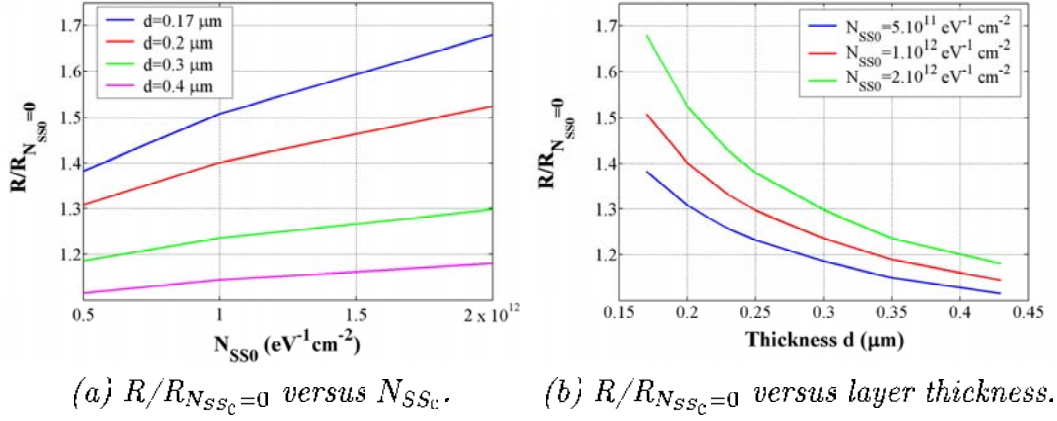


Figure 4.20: Calculated ratios of resistances for different *n-InP* layer thicknesses d and for different minimum density of U-shape surface states N_{SSc} .

$R/R_{N_{SSc}=0}(N_{SSc})$ plots for the thinnest layers (Figure 4.20.a). On the other hand, the curves shown in Figure 4.20.b are much better resolved with respect to N_{SSc} in the case of thinner layers compared to thicker ones. In conclusion, for thicker samples, the influence of surface states on electronic characteristics is observed to be much smaller than for thin samples. As, the sample with the biggest sensitivity to $N_{SSc}(E)$ will be characterized by a high sensitivity to change in these states and as following to surface phenomena as adsorption process, thus the most sensitive samples will be characterized by the smallest active layer thickness.

4.4.4 Q_{FC} impact on electronic properties of InP

Simulations of the band bending modification due to the introduction of the surface fixed charge Q_{FC} taking either positive and negative values were also realized. Such a charge represents the effects of adsorbed ionised molecules that electrostatically change the band bending and the Fermi level position at the semiconductor surface. It can also be defined as a δ -doping that is commonly used for optimization of devices electronic properties. Values of Q_{FC} are chosen to change band bending from inversion to accumulation.

In Figure 4.21, the calculated changes in the surface Fermi level position as a function of the Q_{FC}/q (where q represents an elementary charge) are presented; the value of N_{SSc} is fixed and equal to $10^{12} eV^{-1} cm^{-2}$. The movement of E_F with respect to Q_{FC} shows the range where the InP surface/interface is particularly sensitive to the negative or positive fixed charge. The presented dependence of E_F versus Q_{FC}/q can be used for the optimization of MIS based sensors, by means of shifting the working point along $E_F(Q_{FC})$ curves, resulting in modifying sensing properties [29]. Particular important in this curve is a midpoint,

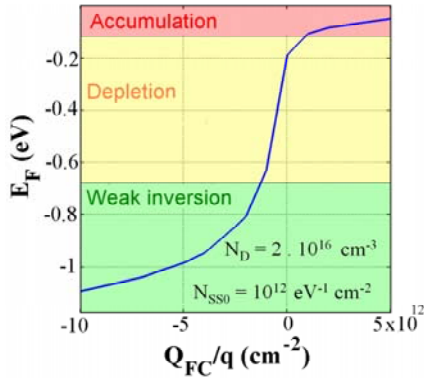


Figure 4.21: Calculated values of Fermi level position versus Q_{FC}/q .

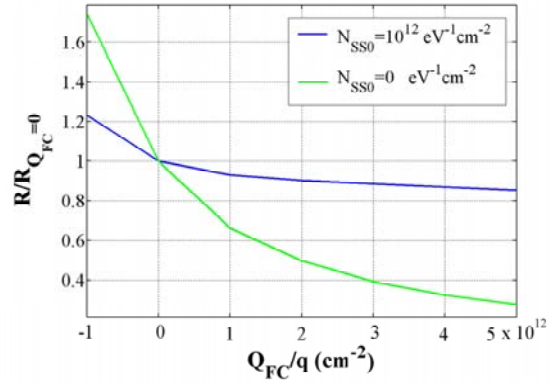


Figure 4.22: Dependences of the InP layer resistance ratio versus Q_{FC}/q .

where the surface Fermi level crosses the Fermi level in an intrinsic semiconductor. It means the sensor structure becomes sensitive to negative as well as positive charges. Moreover, in the linear part of this graph, the surface Fermi level will be the most sensitive to any changes on the surface due to adsorption of ions.

Figure 4.22 represents calculated changes in InP layer resistance as a function of Q_{FC}/q for different minima of the surface state density. It is evident that surface states strongly reduce dynamics of the InP sensor sensitivity towards ionic species in terms of Q_{FC} . In Figure 4.23, the profile of the electric potential $V(x)$ is shown. Presented curves are for the surface band bending induced by both surface states N_{SSc} equal to $10^{12} \text{ eV}^{-1} \text{ cm}^{-2}$, and the surface fixed charge. The existence of surface fixed charge caused the strong change in surface potential. Moreover, the potential value at the surface without surface fixed charge is smaller than zero. This supports the assumption that surface states create the depletion layer in the near-surface region even before surface adsorption.

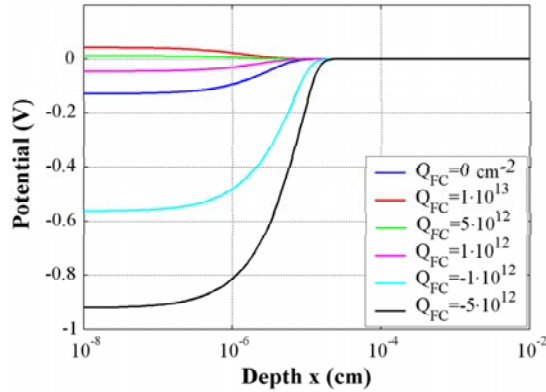


Figure 4.23: Potential in-depth profiles as a function of Q_{FC}/q .

4.4.5 Temperature influence on electronic properties

In addition, the rigorous calculations regarding the influence of temperature on sample resistivity and depletion layer have been performed. The theoretical calculations of the in-depth profiles of the electron concentration $n(x)$ and of

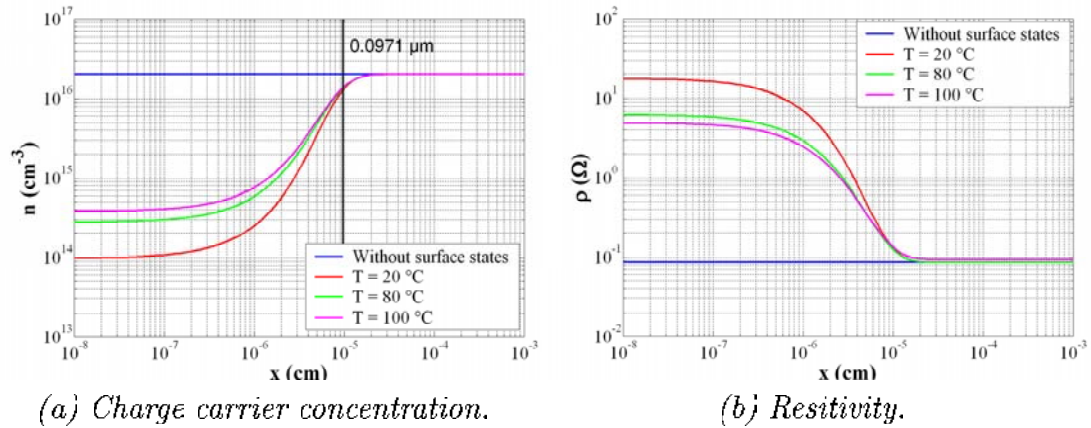


Figure 4.24: Influence of temperature on *n*-InP electronic parameters.

the resistivity $\rho(x)$ of InP sample as a function of temperature was computed (see Figure 4.24). In Figure 4.24 the $n(x)$ and $\rho(x)$ profile versus depth for different temperatures from 20 to 100 °C are presented.

From Figures 4.24 it is shown that changes in the profiles of $n(x)$ and $\rho(x)$ are rather moderate versus temperature. For the initial InP surface, the influence of the temperature on the depletion layer in the studied range is rather slight. However, from the same Figure, the resistivity and charge carrier concentration of the near-surface region are rather affected by temperature. In conclusion the electronic properties of the sample with a thickness in the range of the depletion layer width may be modified by the temperature.

4.5 Studies of InP gas sensor

Once, the sensor device is characterized in terms of its chemical properties and the strong influence of surface states on electronic properties is shown, the experimental study of sensor electronic properties in terms of the Hall effect measurements combined with rigorous calculations is performed. Based on the results presented in this Chapter, a probable mechanism of NO₂ action on the *n*-InP surface is proposed.

4.5.1 Electronic properties

In simulations, a number of parameters are used to get the $p(x)$ and $n(x)$ profiles as a function of the surface conditions regarding the surface states. These parameters are collected in Table 4.7. In order to determine the various electronic characteristics, including the sample resistance from Equations 2.19 and 2.20, one needs to know the mobility of charge carriers. Therefore, electronic properties in terms of the Hall mobility and density of charge carriers as well

as the resistivity of active layers were investigated by means of Van der Pauw measurements.

The experiments were realized on the samples with epitaxial layer thicknesses of 0.2 and 0.4 μm . The results were elaborated using an approach based on assumption that the layer thickness is constant. In the calculations of the electronic parameters it was assumed that the active layer thickness is equal to the InP epitaxial layer thickness after the subtraction of depleted layer thickness (0.097 μm). The sample resistivity was obtained from the Hall effect measurements without magnetic field, while the mobility and the charge carriers density were measured under a 0.3 T magnetic field. Measured values and their uncertainty values are collected in Tables 4.9 and 4.10. It is not surprising that the uncertainty of certain measurements are rather big, especially in the case of the Hall mobility: it is often the case when the layer thickness is in the sub-micron range. The uncertainty values are calculated as indicated in Appendix F.

Table 4.9: *Electronic properties of n-InP active layer $d = 0.2 \mu\text{m}$.*

ρ ($\Omega\cdot\text{cm}$)	μ_H ($\text{cm}^2(\text{V}\cdot\text{s})^{-1}$)	n (cm^{-3})
0.187 ± 0.004	1214 ± 232	$2.7 \cdot 10^{16} \pm 0.1 \cdot 10^{12}$

Table 4.10: *Electronic properties of n-InP active layer $d = 0.4 \mu\text{m}$.*

ρ ($\Omega\cdot\text{cm}$)	μ_H ($\text{cm}^2(\text{V}\cdot\text{s})^{-1}$)	n (cm^{-3})
0.257 ± 0.005	2732 ± 204	$1.4 \cdot 10^{16} \pm 0.2 \cdot 10^{12}$

Table 4.11: *Examples of literature electron mobilities for InP at 300 K.*

μ ($\text{cm}^2(\text{V}\cdot\text{s})^{-1}$)	InP	References
3670	MBE layers	[119]
4000 – 5000	MOVPE layers	[112]
4000	single crystal	[114]
4600	single crystal	[91,116,117]
5400	single crystal	[122]

For the sample layer thickness of 0.2 μm , the Hall mobility was equal to $1214 \text{ cm}^2(\text{V}\cdot\text{s})^{-1}$ while for the sample with layer thickness of 0.4 μm equal to 2732 μm . The impact of the surface is well observed for the thinnest sample its electronic properties will be very different than that for the same material in its bulk. That was already observed in the literature; in the case of thin layers the near-surface region strongly affects the mobility of electrons as well as the other electronic characteristics [114,115,116,117,118,120]. Therefore, it

is not surprising that the samples with layer thickness of $0.2 \mu\text{m}$ exhibited low mobility. It verifies again the influence of the near surface region on the mobility. From the Hall mobility, the electron mobility may be obtained using Equation G.12 (see Appendix G). The value of electron mobility μ was estimated at around $1600 \text{ cm}^2(\text{V.s})^{-1}$ (sample thickness of $0.2 \mu\text{m}$) and for around $3600 \text{ cm}^2(\text{V.s})^{-1}$ (sample thickness of $0.4 \mu\text{m}$). The μ value of the thickest sample corresponds well to the literature data of K. Radhakrishnan et al. for the MBE InP samples, doped by Si ($3.5 \cdot 10^{16} \text{ cm}^{-3}$) with layer thickness between 1 and $2 \mu\text{m}$ [119]. In Table 4.11, examples of electron mobilities for different structure of InP are collected, none of the sample thickness was thinner than $1 \mu\text{m}$.

According to what is previously shown and written, it seems to be a necessity to investigate simultaneously the influence of the surface state distribution and electron mobility variations on the surface resistance. Therefore, the calculations of the resistance as a function of these two parameters were performed; in these simulations, the $N_{SS}(E)$ distribution with a minimum of N_{SSc} that varies from the value equal to 0, 'flat band' case, to $2 \cdot 10^{12} \text{ eV}^{-1}\text{cm}^{-2}$ was used. The values of electron mobility μ were taken as obtained from our experiment and literature data. To simplify the calculations in Equation 2.19, the sample dimensions are assumed to be equal, however the thickness of the sample changes.

Table 4.12: *Measured resistances R (in $k\Omega$) for different sensor devices with their uncertainty values.*

R for $d=0.2 \mu\text{m}$	R for $d=0.3 \mu\text{m}$	R for $d=0.4 \mu\text{m}$
5.4 ± 0.6	2.0 ± 0.3	1.0 ± 0.2
5.7 ± 0.6	1.9 ± 0.3	1.1 ± 0.2
5.6 ± 0.6	2.0 ± 0.3	0.9 ± 0.2

The results of calculations of the n-InP layer resistance versus layer thickness d for different electron mobilities and N_{SSc} as well as experimental data are summarized in Figure 4.25. It is clear that both theoretical and measured values of the InP resistance markedly increase versus decreasing layer thickness because of a gradual increase of the near-surface depletion region. Furthermore, from the comparison of the experimental and calculated resistance values (for different electron mobilities) it follows that for the thinnest sample with $0.2 \mu\text{m}$, the mobility amounts to about $1600 \text{ cm}^2(\text{V.s})^{-1}$, while for thicker samples of d equal to $0.3 \mu\text{m}$ mobility increases to about $3000 \text{ cm}^2(\text{V.s})^{-1}$ and for the sample with d equal to $0.4 \mu\text{m}$ to about $3600 \text{ cm}^2(\text{V.s})^{-1}$. This result corresponds very well to experimental values of mobility obtained from the Hall effect measurements. The observed low mobility value in the thinnest layers (thickness compared to the depletion layer width) we attribute to the enhanced impact of the surface

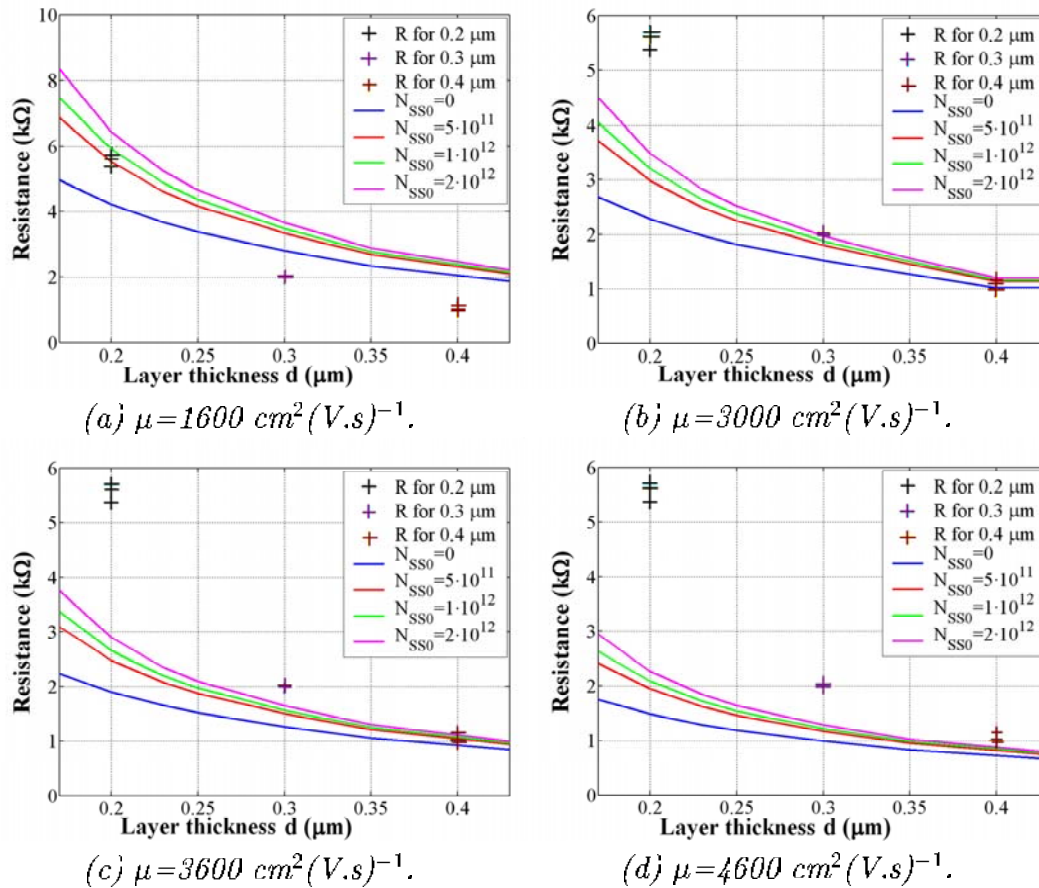


Figure 4.25: Calculated dependencies of *n*-InP layer resistance versus layer thickness *d* for different electron mobilities and N_{SSc} (solid lines) compared with experimental data (crosses).

scattering of electrons. On the other hand, the mobility values achieved in the thicker samples correspond to the values reported by Radhakrishnan et al. [119].

Moreover, from the theoretical calculations is evident that the ‘flat band’ assumption for modeling of the III-V semiconductor surface phenomena is not realistic because the experimental resistance values correspond well to theoretical ones obtained for the surface state density minimum equal to $2 \cdot 10^{12} \text{ eV}^{-1} \text{ cm}^{-2}$ what is in good agreement with literature data [37]. In addition from Figure 4.25 it can be noted that the thickest sample are not sensitive to a small thickness change. Therefore, the uncertainty value of the layer thickness (about 20 %) will not have great influence on electronic properties of these sample, contrary to the case of the thinnest ones. This is the reason why in the further simulations of InP electronic properties for thick samples we used the electron mobility value of $3600 \text{ cm}^2(\text{V.s})^{-1}$, because this mobility value is in a good accordance with the mobility of the layer thickness of $0.4 \mu\text{m}$.

As previously discussed, the surface states density with minimum at about $2 \cdot 10^{12} \text{ eV}^{-1} \text{ cm}^{-2}$ corresponds to the native oxide-InP layer interface [37]. Therefore, from the results of our analysis we have found that the studied InP epitaxial surfaces are well characterized by the same density of surface state as reported in the literature. It is important to note that for this density of surface states the Fermi level is placed (weakly pinned) at -0.2 eV with respect to the bottom of the conduction band (see Figure 4.19). This weak pinning of E_F allows for the surface sensitivity towards adsorbed ionized species in terms of the negative Q_{FC} : E_F can move along the linear sloped part (depletion) of the S-like plot in Figure 4.21. On the other hand, we have previously observed that the oxide layer stabilizes well the sensor characteristics. This means that such a weakly pinned surface is advantageous for InP sensor structures.

4.5.2 NO₂ action on electronic properties of InP

In conclusion, the outer layer of InP sensor device is covered by InP-related oxide film (predominately In₂O₃ and other oxides) containing carbon contaminations that provokes the surface states with their density minimum estimated to be equal around $2 \cdot 10^{12} \text{ eV}^{-1} \text{ cm}^{-2}$. From the references [59,72] the transfer of electrons from InP bulk to InP surface oxides is possible, thus, as NO₂ is a molecule of oxidizing gas having one unpaired electron it will react with the charges from the native oxide and interface region. As the native oxide layer remains in equilibrium with n-InP, NO₂ action will result in the enhancement of the depletion region in the InP bulk. A study of the development of the depletion layer due to gas adsorption was realized using Hall effect measurements.

Figure 4.26.a. shows the changes in the electron concentration of a n-InP epitaxial layer as a function of NO₂ concentration. It can be noted that an increase in gas concentration from 0 to 200 ppb causes a decrease in the electron concentration due to the development of the depletion layer. Therefore, the active layer thickness as a function of following gas concentration was computed. The results of this calculation are collected in Figure 4.26.b. This Figure illustrates the development of the surface depletion layer as a function of gas concentration from 0 to 200 ppb. It can be observed that an exposure of 40 ppb already causes visible changes in the electronic parameters of the n-InP layer, such as modifications of the charge carrier concentration and width of depletion layer (200 ppb caused a 4.7 nm increase in the depletion region width). It can be also seen that for concentrations of 100 ppb and higher, the changes are very small.

Since the adsorbed ionized gas species can be represented by the surface fixed charge, the theoretical analysis of the influence of Q_{FC} on the depletion layer development was carried out. The results of this analysis are shown in Figure 4.27. From this Figure it follows that the changes in the depletion layer due

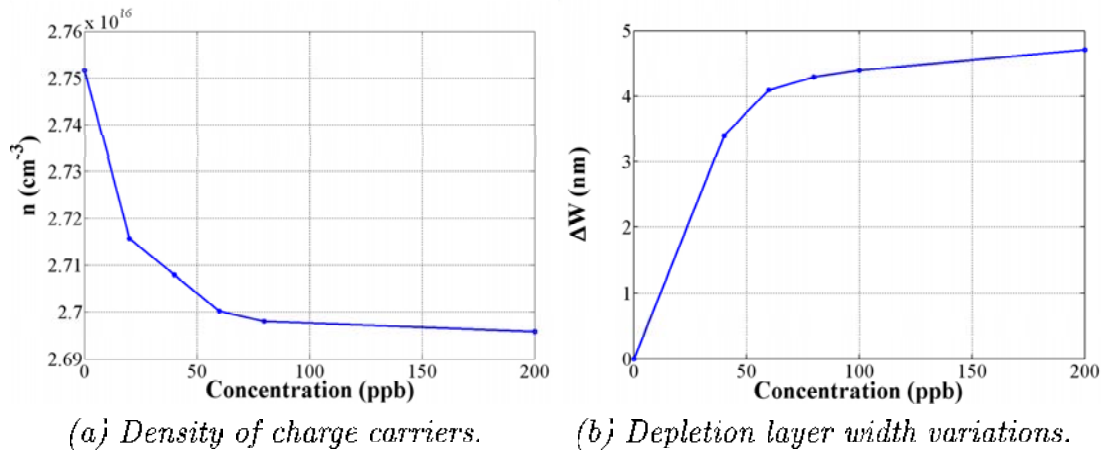


Figure 4.26: Hall effects results.

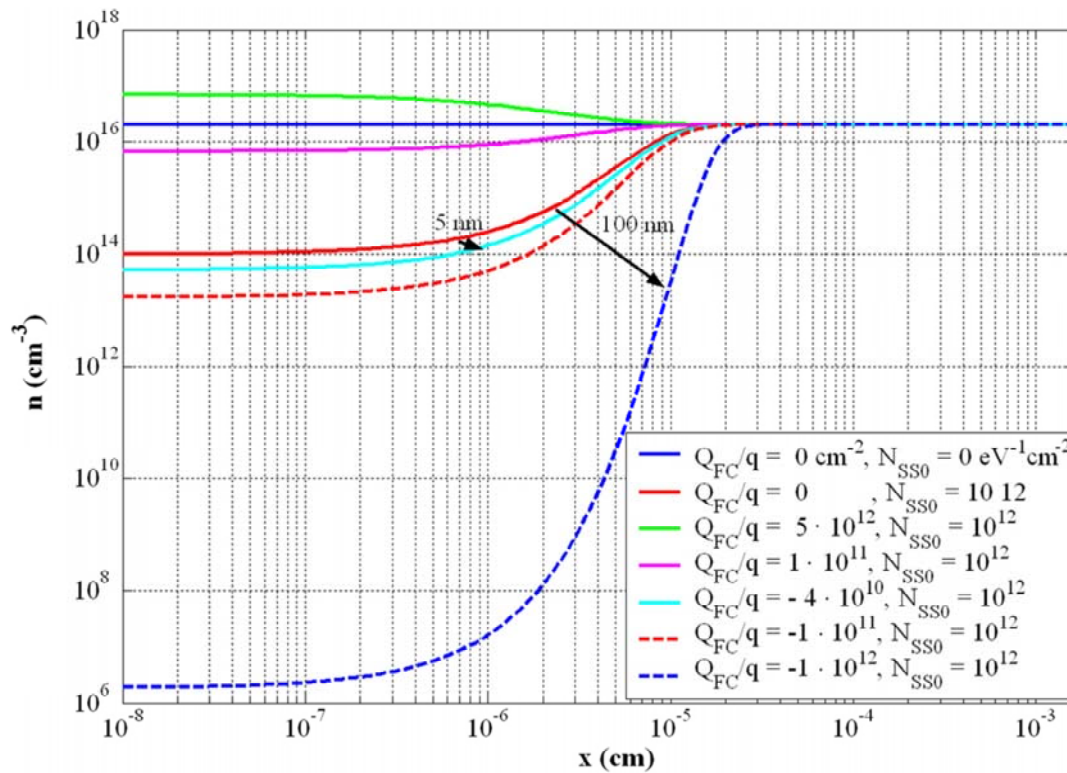


Figure 4.27: In-depth profiles of charge carrier concentrations as a function of Q_{FC}/q .

to Q_{FC} vary as a function of the value of the negative Q_{FC} charge. Under the assumption that all NO_2 molecules adsorbed at the n-InP surface are ionized, they become NO_2^- , because they captured an electron from the semiconductor. Once the equilibrium between gas and semiconductor surface is obtained, NO_2^- ions repulse other electrons and the development of the depletion layer (width W) takes place. Therefore, it may be approved that adsorbed ions of NO_2^-

give the similar charging result in the InP near-surface region as the negative surface fixed charge Q_{FC} . On this basis it was estimated that Q_{FC}/q equal to $-4 \cdot 10^{10} \text{ cm}^{-2}$ provokes the development of the same depletion layer width (around 5 nm) as 200 ppb of NO_2 . The change in the depletion layer may reach even to 100 nm due to $-1 \cdot 10^{12} \text{ cm}^{-2}$ of Q_{FC}/q . The calculations of the depletion layer width were done using the approach described in Section 4.4.2. In Table 4.13 the depletion region width of samples with N_D equal to $2 \cdot 10^{16} \text{ cm}^{-3}$ are calculated for different Q_{FC}/q values.

Table 4.13: *Calculated W caused by N_{SSc} of $10^{12} \text{ eV}^{-1} \text{ cm}^{-2}$ and Q_{FC}/q for N_D equal to $2 \cdot 10^{16} \text{ (cm}^{-3}\text{)}$.*

W (μm)	Q_{FC}/q (cm^{-2})	$ V_s $ (V)
0.097	0	0.14
0.103	$-4 \cdot 10^{10}$	0.15
0.104	$-5 \cdot 10^{10}$	0.16
0.112	$-1 \cdot 10^{11}$	0.18
0.202	$-1 \cdot 10^{12}$	0.59

4.5.3 Mechanism of NO_2 action

Once a stable gas sensor response to NO_2 is obtained, a tentative model of the gas action on the n-InP surface can be built basing on the microscopic and spectroscopic studies as well as Hall effect measurements and theoretical simulations. Figure 4.28 shows the probable mechanism of the gas action on the n-InP surface. NO_2 adsorbs at the native-oxide layer; when adsorbed becomes negatively charged NO_2^- due to a transfer of electrons from the InP bulk to outer oxide layer, the development of the depletion layer in the InP bulk takes place. Subsequently, after capturing electrons by the gaseous species equilibrium between ionized adsorbed gas molecules and a native oxide layer and a semiconductor is reached. In consequence, an increase in the InP resistance, compared to the initial one R_0 , is observed.

4.6 Sensor characteristics

From the previous works of the gas sensor group from LASMEA, the gas sensor devices based on epitaxial n-InP layers exhibit great sensitivity toward oxidizing gases in the range of ppm [14,15,20,21,22,23,24,25,26,27]. One of the main aims of this Thesis was to extend sensing characteristics of these devices over ultra-low gas concentrations in the ppb range. In this section, the results of experiments realized for NO_2 concentrations from 20 to 100 ppb are presented. The sensor response was studied in terms of the resistance changes of the active layer ΔR ; on the other hand gas sensor stabilization was investigated. Moreover,

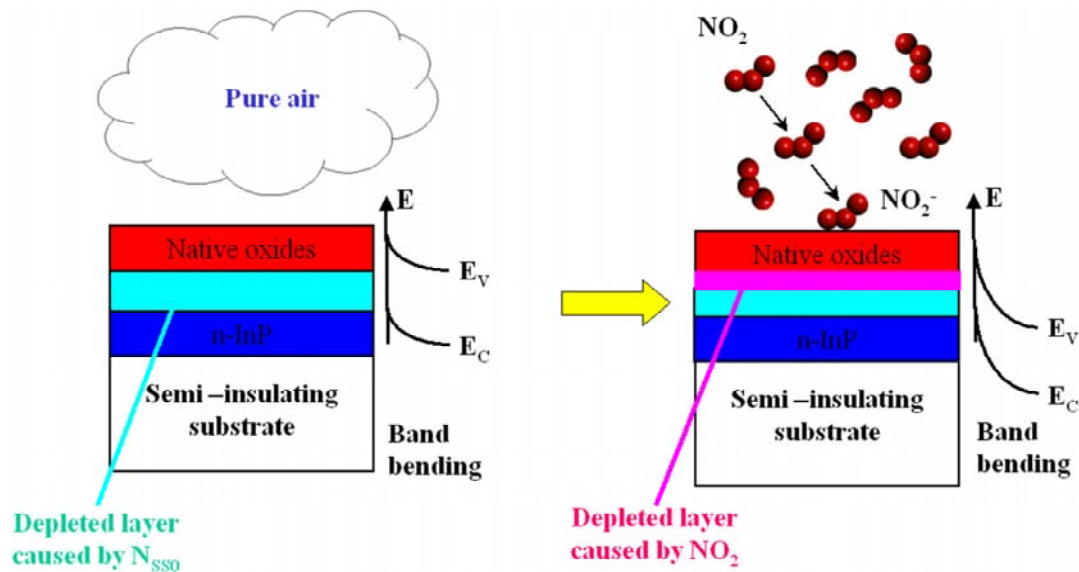


Figure 4.28: *Schema of the gas action.*

the sensor devices were examined from the point of view of their characteristics, i.e., selectivity, sensitivity, reproducibility, response time, etc. A comparison of the characteristics of sensor structures with different n-InP layer thicknesses was carried out so as to optimize the sensor devices.

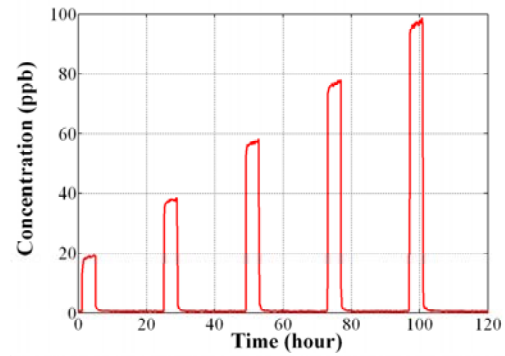
4.6.1 Sensor response

In order to test ΔR , different sequences of gas exposures were realized ranging from 20 to 100 ppb. These very low concentrations were obtained using the measurement set-up described in Section 3.2. In experiments, the gas concentration was verified by a NO_2 analyser. The concentration data and examples of the gas exposure sequences used are shown in Figures 4.29, 4.30 and 4.31. The corresponding resistance changes are also presented in these Figures. In all gas exposure experiments, sensor devices with different layer thicknesses (from 0.2 to 0.4 μm) were used. This experimental configuration allowed us to characterize the sensors in terms of their selectivity, sensitivity and the response time as a function of the gas concentration.

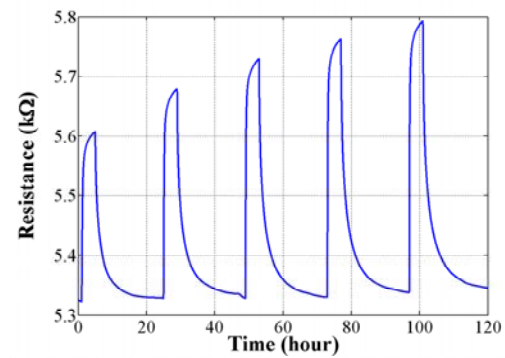
Presented sensor responses were for a working temperature of 80 °C. This temperature was chosen to improve the response time of the InP sensors. It should be noted that the temperature value was limited enough not to destroy the sensor structure. This problem was studied in Section 4.6.5.

Figure 4.29 represents the sensor resistance changes due to step exposures to different gas concentrations. Each step of gas exposure stopped and started with exposure to air. Each gas exposure lasted 4 hours, while in Figure 4.30 each gas

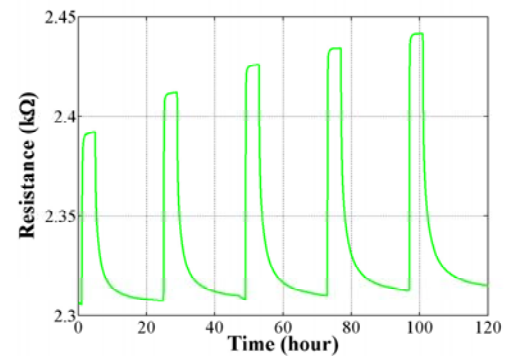
(a) NO_2 concentration.



(b) ΔR for $d=0.2 \mu\text{m}$.



(c) ΔR for $d=0.3 \mu\text{m}$.



(d) ΔR for $d=0.4 \mu\text{m}$.

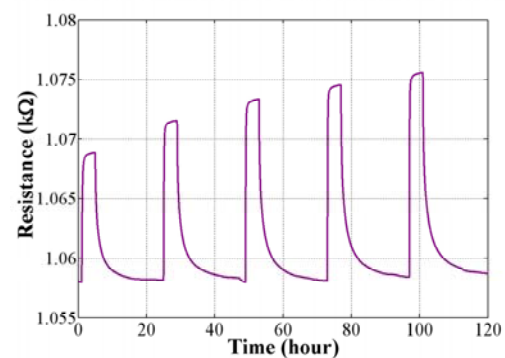


Figure 4.29: Resistance changes towards various gas concentration exposures with duration of 4 hours each, 80°C

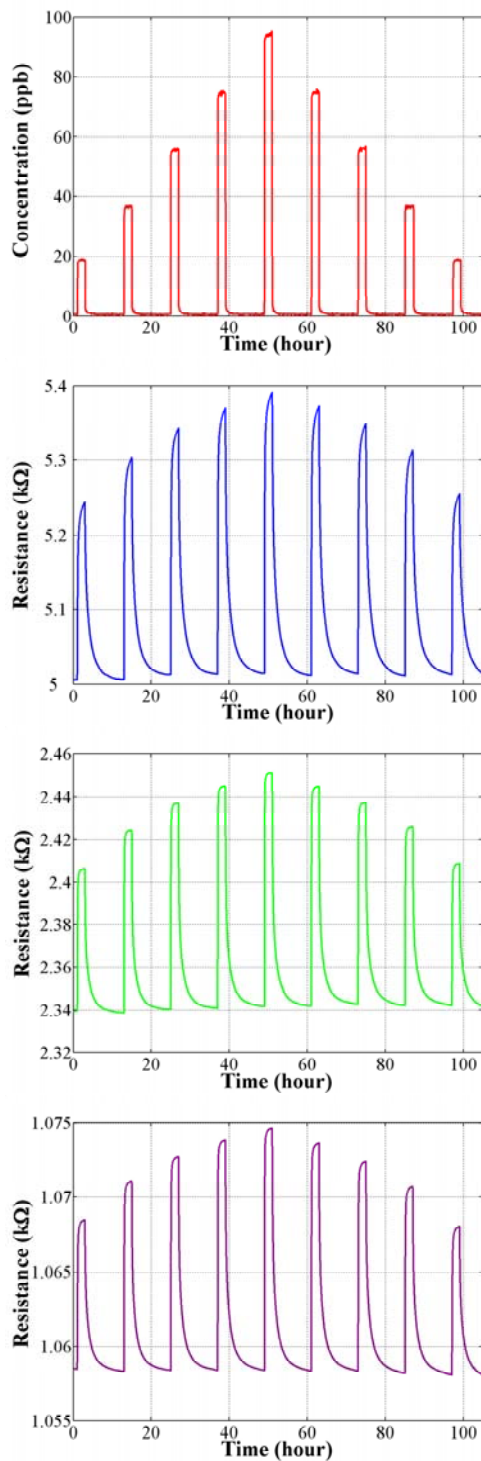


Figure 4.30: Resistance changes towards various gas concentration exposures with duration of 2 hours each, at 80 °C.

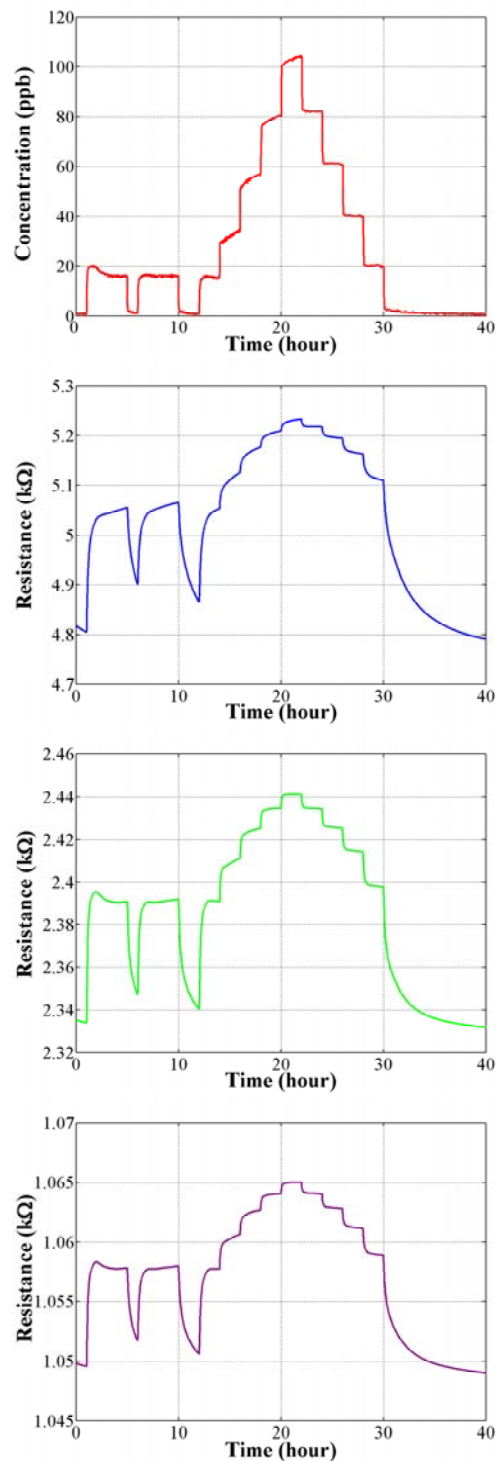


Figure 4.31: Resistance changes due to different gas exposure sequences with and without exposure to air, at 80 °C.

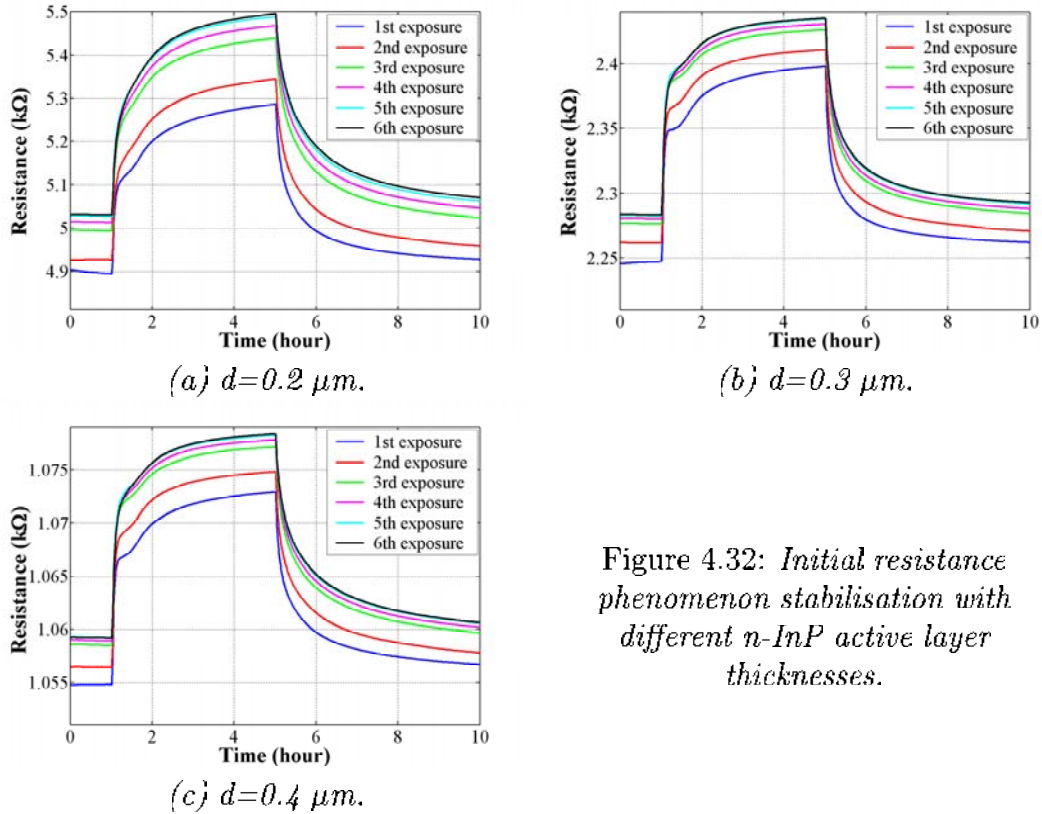


Figure 4.32: *Initial resistance phenomenon stabilisation with different n-InP active layer thicknesses.*

exposure was only 2 hours. In Figure 4.31, tested sensors were exposed to the gas in 2 different sequences: in the first one, the sensors were exposed twice to 20 ppb of NO_2 , with an air flushing after each exposure to the gas, before being exposed to gas concentrations going from 20 ppb to 100 ppb in steps of 20 ppb. In the second case, air flushing was omitted. From the presented figures, it is evident that our gas sensors followed well concentration changes of NO_2 , even for decreasing steps.

From Figures 4.29, 4.30 and 4.31, it is clear that each device was characterized by a quite good sensitivity to very low NO_2 concentrations of 20 ppb. The sensitivity of the sensors was also improved for higher concentrations. In addition, sensors reacted rather fast for small changes in the gas concentration, which is particularly visible in Figure 4.31. Moreover, they worked at rather low temperatures for a gas sensor technology of 80°C .

4.6.2 Response stabilization

As it was mentioned before and from our previous results verified by the systematic work, it was observed that the InP response towards NO_2 evolves from the first exposure up to the stable and reproducible response. In Figure 4.32, the gas sensor response evolution to 100 ppb of NO_2 is shown, tested

devices differing by the active layer thickness ranging from 0.2 to 0.4 μm . The working temperature is 80 $^{\circ}\text{C}$. From Figure 4.32, it is observed that for different sensor structures with different n-InP active layer thicknesses and for the same working conditions like temperature, sensors behave similarly. During the first hour of the first gas exposure, the phenomenon of fast increase in the sensor resistance is observed. After, changes in layer resistance are much smaller. Following this initial phase, sensor exposures cause the initial resistance increase and the response stabilization is observed. Once the stabilization was obtained, sensor responses were reproducible (see 5th and 6th exposures in Figure 4.32).

This phenomenon of n-InP sensor response stabilization was never investigated before by means of surface spectroscopy. From the spectroscopic studies presented in Section 4.3.3, the response stabilization can be understood in terms of the native oxide layer and interface structure transformation. Thus, the sensor stabilization response in terms of its initial resistance development can be explained by the stabilization of the surface chemical state and as following the changes in surface state density.

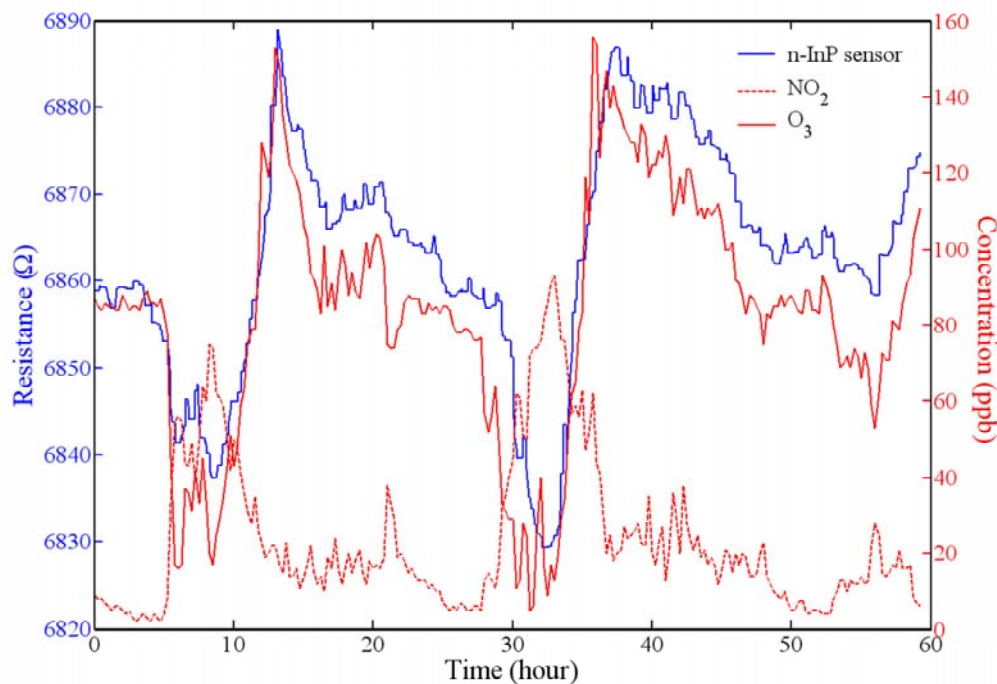


Figure 4.33: *n-InP* sensor response towards gaseous mixture of NO_2 and O_3 , at 80 $^{\circ}\text{C}$.

4.6.3 Selectivity

From our previous results it was assumed that in presence of reducing and oxidizing gases, the n-InP sensor device is selective to oxidizing ones [26,27]. InP sensors were already tested in outdoor conditions. The results of these tests, in terms of the resistance changes due to gaseous mixture versus exposure time, are presented in Figure 4.33. The gaseous mixture was composed of NO_2 and O_3 . The gas concentrations were measured by gas analysers and the resistance by a multimeter. The device was kept at 80°C . The results show that the sensor response followed the concentration changes of ozone, which is one of the strongest oxidizing gases among air pollutants.

4.6.4 Sensitivity

Sensitivity of n-InP epitaxial layers is characterized by the relative resistance $\Delta R/R_0$. In Figure 4.34 the relative resistance change comparison between the samples with different layer thickness is presented. The resistance changes are due to 100 ppb of NO_2 , working temperature was 80°C . From this Figure it can be observed that the sample with the thinnest layer thickness are the most sensitive one. In Figure 4.35 relations between $\Delta R/R_0$ for different active layer thickness and different NO_2 concentration ranging from 20 to 100 ppb are shown. As from theoretical calculations and now from Figures 4.34 and 4.35, it is clearly shown that the structure response to NO_2 is strongly influenced by the thickness of the active layer. In the range of thickness from 0.2 to $0.4\ \mu\text{m}$, the relative resistance is the highest for an active layer thickness of $0.2\ \mu\text{m}$.

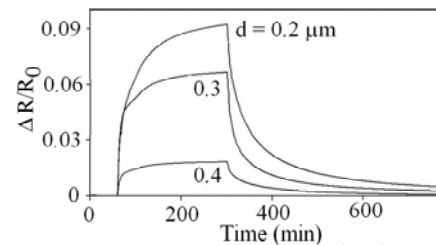


Figure 4.34: *Relative resistances for gas sensors with different d , for 100 ppb of NO_2 , at 80°C .*

4.6.5 Response time

The response time is defined in Section 1.3.1. Figure 4.36 shows the calculated average response times for different series of sensor devices, with different thickness of the n-InP layer, versus NO_2 concentration from 20 to 100 ppb, at different working temperatures from 80°C to 100°C . From this Figure it can be observed that the response time is strongly influenced by gas concentration being the highest for the smallest concentration, and by the active layer thickness. In addition, a small increase in temperature (of 20°C) ameliorates the response time. The response time towards 20 ppb of NO_2 for a sensor with active layer thickness of $0.2\ \mu\text{m}$ is equal to about 60 minutes while for a sensor with active

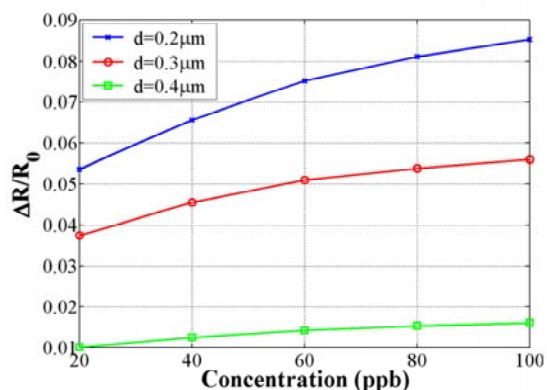


Figure 4.35: Measured relative resistance for three sensors versus NO_2 concentration, at 80 °C.

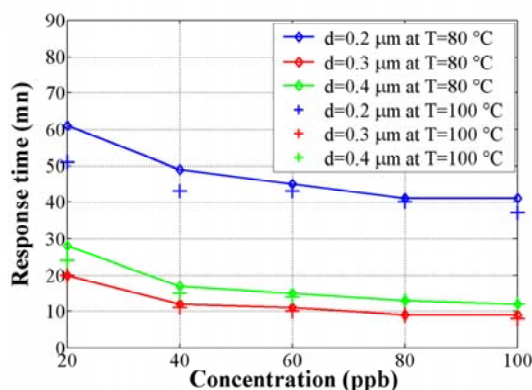


Figure 4.36: Calculated response time as a function of gas concentration and working temperature.

layer thickness of 0.3 μm it is less than 30 minutes and for 0.4 μm about 20 minutes. This is probably due to the fact that the influence of the depletion layer is stronger in the thinner sample which exhibits the highest sensitivity, but is less stable than thicker devices. In conclusion, the sensors response time

Table 4.14: Calculated response times as a function of temperature for the sample layer thickness 0,3 μm .

Temperature (°C)	Response time (min)
20	316
80	6
100	3

is longer under low gas concentration and shorter for thicker devices (higher working temperatures also ameliorate the response time). Table 4.14 gives the best computed response time obtained by a sensor with a 0.3 μm layer thickness at different temperatures under 100 ppb of NO_2 . The table shows clearly the amelioration of response time with temperature (316 minutes at 20 °C, 3 minutes at 100 °C). This is probably due to the better kinetics of adsorption at high temperatures.

4.6.6 Reproducibility

Reproducibility of the sample has been studied in terms of the reproducibility of device relative resistances. In Figure 4.37 the relative resistances of the sensor devices, for different series, versus NO_2 different concentrations are shown. In this Figure one can observe that the different series of sensor devices based on the same n-InP wafer coming from the same manufacturer are rather reproducible.

The behaviour of the sensor with an active layer thickness of $0.3 \mu\text{m}$ is not well explained yet.

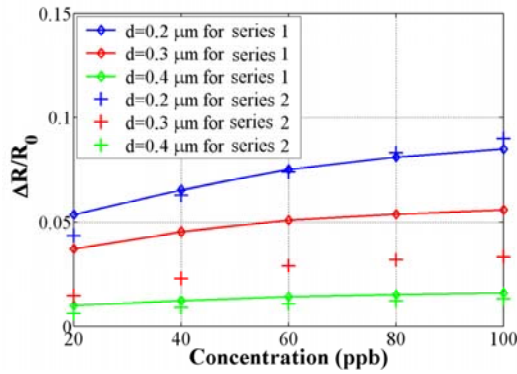


Figure 4.37: Comparison of relative resistances for different series of gas sensor.

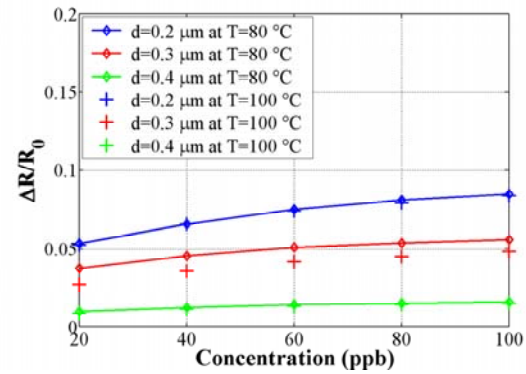


Figure 4.38: Influence of temperature on relative resistance.

4.6.7 Other parameters

Other important operating parameters, which are considered in gas sensor technology are temperature and humidity; they can strongly affect the behaviour of chemical gas sensors. Thus, it is very important to characterize the gas sensor under influence of the temperature and humidity.

Temperature

Temperature is an important parameter determining the operation of chemical sensors. In the case of the n-InP epitaxial layer devices, the parameter mostly affected by temperature changes is the response time, as shown in Table 4.14 where the calculated response time for the room temperature up to $100 \text{ }^\circ\text{C}$ are summarized. It is evident that an elevation of temperature improves the response time of the gas sensor; however the working temperature should not be higher than the critical one for the semiconductor device used (less than $120 \text{ }^\circ\text{C}$ in case of our sensors).

Humidity

It has been shown in previous work [23,26] that humidity affects the initial resistance of InP based sensors. From [23] the resistance increases with the amount of relative humidity. This effect was not studied in the present work.

all our experiments being performed with a mixture of gas and pure dry air.

In this Chapter the n-InP based sensor devices were presented as well as their characterization in terms of the sensing, chemical and electronic properties. The experimental studies showed the great sensitivity of the n-InP epitaxial layer based gas sensor at extremely low concentrations of NO₂, a rather short response time (less than 10 min. at 80 °C) and a great stability of R_0 , all of which would support its use in atmospheric gas sensing applications. NO₂ action on InP surface causes an augmentation of the resistance of the structure, which sensitivity depends strongly on the active layer thickness. This can be explained by an increase of the bulk depletion layer under NO₂ exposures and changes in surface potential barrier due to oxidizing gas action.

The Hall effect measurements in terms of electron concentration as a function of gas concentration proved that the gas sensing effect consists in development of the depleted layer in the semiconductor bulk. XPS spectroscopy combined with AES investigations gave evidence of the chemical complicated structure of the native oxide covering InP surfaces. It was observed that NO₂ action causes an increase of the InP native oxides layer thickness from 3 nm to 3.3 nm. The change in surface roughness after gas exposition well shows that gas action caused also the structural transformation of native oxide and carbon contamination layer.

The role of the native oxide layer in sensing mechanism and sensor response stabilization phenomena was explained. Moreover, the influence of native oxides on surface states density and surface Fermi level pinning was shown. The influence of surface Fermi level pinning on electronic properties of n-InP based sensor as well as on the great stability of n-InP initial resistance was discussed.

From the calculations a strong influence of the interface states (with a typical minimum value N_{SS0} in the range of 10^{12} eV⁻¹ cm⁻²) on the resistivity and electronic properties of n-InP epitaxial layers with thicknesses in sub-micrometer range was proved. This density of surface states caused the depletion layer near the InP surface with the thickness estimated at about 0.0971 μm. The n-InP layer resistivity showed also great sensitivity to the surface fixed charge Q_{FC} . These properties can be effectively used in the modelling and optimization of microstructured InP-based devices, in particular gas and ion sensors.

The gas sensor characteristics were also studied as well the influence of the temperature on device performances. Additionally the good quality of the ohmic contacts using AES microscopy, SEM and AFM images was proved.

Conclusion

- An extensive and comprehensive analysis of both chemical and electronic properties of the sensing n-InP epitaxial layers were performed by means of advanced analytical methods, including surface spectroscopic techniques (XPS, AES) and Hall effect measurements. Furthermore, the rigorous computer analysis of the influence of surface states on the electronic parameters of the near-surface region in a n-InP layer was carried out. The results of the applied approaches were correlated. A detailed description of the sensor structure was also presented, as well as the results of the studies bearing on its sensing properties, in terms of the InP layer sensitivity, reproducibility and sensitivity to temperature.
- Series of n-InP epitaxial layer devices with a different thickness of active layer from 0.2 to 0.4 μm and doping level given by producer of $2 \cdot 10^{16} \text{ cm}^{-3}$ were fabricated by the author comprising fabrication of ohmic contacts and final sensor mounting in the measuring cell. The adaptation of the Van der Pauw method to the experiments with gas was realized. The sensing measurement set-up allowing for the low gas concentration was constructed. The XPS and AES study as well as rigorous analysis of the electronic properties were also performed.
- The realized InP based gas sensors were tested for oxidising gas concentrations within the range of atmospheric pollutants quantities. The experimental studies showed that the sensors exhibited a great sensitivity to extremely low concentrations of NO_2 (20 ppb) and a rather short response time (3 min. at 100 °C). Moreover, the devices exhibited the great stability of R_0 in time, probably because of its chemical and electronic properties (native oxide layer, Fermi level pinning). These characteristics seem to qualify this type of sensor for outdoor applications in air quality monitoring.
- The role of the InP native oxide layer in sensing mechanism as well as its influence on electronic properties i.e. band bending and surface Fermi level was evidently shown. The stable oxide layer provides to the stable

sensor structure with very stable initial parameters as resistance. These oxides cause the surface Fermi level pinning that is known to make the structure insensitive on gas molecule adsorption, however, in our case the weak pinning of Fermi level does not make a n-InP surface completely insensitive, moreover it improves the stability of the n-InP based sensor.

- The chemical and electronic status as well as the relative resistance changes versus Q_{FC} were used in the elaboration of the existent modelling of gas sensing mechanism. NO_2 reacts with the active sites in the outer oxide layer predominately identified by In_2O_3 oxide, adsorbed at the n-InP surface, it capture an electron from InP bulk and becomes NO_2^- , with assumption that the transfer of electrons from InP bulk to InP surface oxides is possible. NO_2^- provokes an increase of the depletion layer width and changes in the surface potential barrier, by repulsion of the other electrons. This was investigated by Hall effect measurements, and the relationship between the number of charge carriers and the gas concentration showed that the gas effect consists in electron capture from the semiconductor bulk. The development of depletion layer width was estimated of around 5 nm for 200 ppb. Additionally, it was found that the Q_{FC}/q of about $-4 \cdot 10^{10} \text{ cm}^{-2}$ provokes the same change in the depletion layer width (around 5 nm) as 200 ppb of NO_2 .
- The gas sensor response towards NO_2 was studied in terms of resistance changes. Both the obtained experimental results and theoretical analysis show a strong dependence of the sensitivity of the sensor on the active layer thickness. Consequently, the sensor was optimized in terms of the active layer thickness for low doped n-InP epitaxial layers. The selected thicknesses for the epitaxial layer were 0.2, 0.3 and 0.4 μm , the best sensitivity being observed for a thickness of 0.2 μm . The samples with epitaxial layer thicknesses of 0.2 and 0.4 μm were then characterized in terms of its doping level and electron mobility using Van der Pauw method. The depletion layer width caused by the N_{SSc} in the range of about $10^{12} \text{ eV}^{-1} \text{ cm}^{-2}$ that is the value of an InP sample covered by native oxides, was also estimated. The computed depletion layer for a doping level $2 \cdot 10^{16} \text{ cm}^{-3}$ was in the range of 0.1 μm .
- A rigorous theoretical analysis of the resistivity of InP layers as a function of the surface state density N_{SSc} as well surface fixed charge Q_{FC} was conducted, in order to characterize their electronic status. The band bending was induced by the surface states density N_{SS} and the surface fixed charge Q_{FC} taking both positive and negative values. Such a charge represents both physically adsorbed ionic species and the surface doping applied in order to control the gas sensitivity of the layer. The band bending induced

by Q_{FC} was observed to change from accumulation to inversion. In the calculations, a U-shaped continuous surface state distribution in the energy gap was assumed in accordance with the Disorder Induced Gap State model. The layer thickness was varied in the sub-micrometer range down to the approaching the depletion region width. In addition, the in-depth profiles of the potential barrier and carrier density were computed. The theoretical analysis confirmed the effect of the surface states and depletion region width on the sensor resistance. The results of our calculations revealed a strong influence of the interface states (with a typical minimum value N_{SSc} in the range of about $10^{12} \text{ eV}^{-1} \text{ cm}^{-2}$) on the resistance of n-InP epitaxial layers with thicknesses in sub-micron range, contrary to standard approaches for semiconductor gas sensors modelling.

- The relative resistivity of the sensor was computed as a function of the surface fixed charge Q_{FC} and its taking positive or negative values, showing a very strong dependency on this parameter. Furthermore, the strong influence of the initial surface state density on the dynamics of the relative resistance changes versus Q_{FC} was demonstrated.
- The chemical status of the sensor was investigated by means of the surface spectroscopy. X-ray Photoelectron combined with Auger Electron Spectroscopy investigations all of which gave evidence of the chemical complexity of the surface region of InP material. Using Ar^+ sputtering the probable model of n-InP device was possible to estimate. It consists of a carbon and oxide contamination layer, a continuous layer of InP oxides and non-continuous alternate layers of In and P. The layer of oxide was predominately estimated to be In_2O_3 . In addition was observed that NO_2 action causes changes in InP native oxide layer thickness from 3 nm to 3.3 nm. This thickness change was estimated using XPS quantitative analysis based on the AES results. The change in surface roughness after gas exposure as well as XPS technique showed that gas action caused the structural transformation of the surface region, which can be explained by changes in the native oxide and contamination layers. This structural transformation of native oxide and carbon contamination layer may explain the sensor response stabilization.
- In addition, the weak dependence of the relative resistance and depletion region on temperature in the studied range was observed experimentally and checked by theoretical calculation.
- The good quality of the realized ohmic contacts to InP layers was demonstrated by studying of their contact resistance, that was found to be equal

about 270.6 Ohm. In addition, surface spectroscopic and microscopic studies of contact were performed. As a result of these studies, practically no contamination of the chemical composition of the contact was observed. The contact is characterized by a quite good homogeneity, which can be improved by annealing the sample after the contact realization.

In conclusion, within the Thesis the extended experimental and theoretical characterization of chemical and electronic properties of free InP epitaxial layers was performed. The measurements of the resistance variations demonstrated that the InP based sensors are extremely sensitive to oxidizing gas molecule adsorption and can be used for monitoring harmful gas concentration in the ppb range. Furthermore, the electronic quantities and processes taking part at the native oxide-InP interface exposed to oxidizing gas were described in detail. The consistency of both experimental and theoretical results was found. The obtained results allow for both better understanding of the gas action mechanism as well provide important information for thin layer semiconductor gas sensor technology, particularly in context of growing interest in low-dimensional integrated sensor systems based on III-V semiconductors.

The first step in the characterization and optimization of the gas sensors on the base of n-InP epitaxial layers was realized. Moreover, we understand better the action of gas on the n-InP surface. However, future studies in terms of chemical composition of the contamination layer as well as its influence on the electronic properties are needed. Also, the gas desorption process has not been explained yet. Therefore the in-situ and ex-situ analysis under the controlled gas flow may well elaborate our knowledge. At the end I propose to use the sample with modified near-surface region by Q_{FC} with positive sign, that will create the accumulation layer in our sensor, it can be interested step in technology process. The other interesting thing in InP sensor technology would be creation of the porous InP sample, that may increase the surface sensitivity of the sensors. As for outdoor tests, I propose the systematic study on construction of the micro-system that will be insensitive towards presence of ozone.

Appendixes

Appendix A

Conversion of $\mu\text{g}\cdot\text{m}^{-3}$ in ppb

The standard unit of pollutant concentration is $\mu\text{g}\cdot\text{m}^{-3}$, however most commercial analysers express the gas concentration in ppm or ppb. The unit ppm means a part of the pollutant per million (10^6) parts of solvent-air and ppb a part per billion (10^9). This appendix deals with a conversion between these two usual units.

The concentration in $\mu\text{g}\cdot\text{m}^{-3}$ $C_{\mu\text{g}\cdot\text{m}^{-3}}$ represents the relation between the mass of the pollutant $m_{\text{pollutant}}$ and the air volume V_{air} :

$$C_{\mu\text{g}\cdot\text{m}^{-3}} = \frac{m_{\text{pollutant}}}{V_{\text{air}}} \quad (\text{A.1})$$

and the concentration in ppb C_{ppb} represents the relation between the pollutant volume $V_{\text{pollutant}}$ and the air volume V_{air} :

$$C_{\text{ppb}} = \frac{V_{\text{pollutant}}}{V_{\text{air}}} \quad (\text{A.2})$$

The Equation for a perfect gas is:

$$V = \frac{n \cdot R \cdot T}{P} \quad (\text{A.3})$$

where:

- P is the gas pressure in Pa;
- V is the volume of the gas expressed in m^3 ;
- R is the gas constant equal to $8.314472 \text{ J}\cdot\text{mol}^{-1}$;
- T is the temperature in K;

- n is the number of moles defined by:

$$n = \frac{m}{M} \quad (\text{A.4})$$

where:

- m is the mass of gas expressed in μg ;
- M is the molar mass expressed in $\mu\text{g}\cdot\text{mol}^{-1}$.

From Equations A.1, A.2 and A.3, the C_{ppb} concentration as a function of $C_{\mu\text{g}\cdot\text{m}^{-3}}$ can be obtained and is given by the following expression:

$$C_{ppb} = \frac{C_{\mu\text{g}\cdot\text{m}^{-3}} \cdot R \cdot T}{M_{pollutant} \cdot P} \quad (\text{A.5})$$

where $M_{pollutant}$ is the molar mass of the pollutant in $\mu\text{g}\cdot\text{mol}^{-1}$.

Appendix B

Electron and Hole Statistics in Semiconductors

According to quantum mechanics, the energy states which are occupied by electrons are discrete with energy broadening between them according to the Heisenberg principle. These states can create a quasi-continuous band when the distance between them is much smaller than the random thermal motion energy [56,57,60].

The analysis of electron and hole statistics in a semiconductor introduces two concepts:

1. the energy state density in energy bands,
2. the probability distribution function.

The energy state density in energy bands $N(E)$ determines the quantity of surface states per unit energy and per unit volume. The probability distribution function f_0 defines the probability of a state occupation with a certain energy E by the charged particles. In the semiconductor bulk, under thermal equilibrium, electrons occupy energy states according to the Fermi-Dirac statistics. In the case of states occupied by electrons with opposite spins, the Fermi-Dirac distribution function is expressed by the following equation:

$$f_0(E) = \left[\exp\left(\frac{E - E_F}{k \cdot T}\right) + 1 \right]^{-1} \quad (\text{B.1})$$

where:

- E_F is the Fermi level energy;
- k is the Boltzmann's constant;
- T is the absolute temperature.

The distribution function of holes f_h is equal to:

$$f_h(E) = 1 - f_0(E) \quad (\text{B.2})$$

When impurities states, traps and other additional energy states caused for example by a gas action are taken into account, the Fermi-Dirac distribution function must be modified as follows:

$$f_{impc}(E) = \frac{1}{\frac{1}{\beta} \cdot \exp\left(\frac{E-E_F}{k \cdot T}\right) + 1} \quad (\text{B.3})$$

where β is the so-called factor of degeneracy ($\beta = 2$ for a donor impurity, $\beta = \frac{1}{2}$ for an acceptor impurity).

According to the theory of quasi-free electron, the density of energy states in the conduction band near its bottom E_C , is expressed by following function of the square root of the energy:

$$N(E) = 4 \cdot \pi \cdot \frac{(2 \cdot m_n)^{\frac{3}{2}}}{h^3} \cdot \sqrt{E - E_C} \quad (\text{B.4})$$

and near the top of the valence band E_V :

$$N(E) = 4 \cdot \pi \cdot \frac{(2 \cdot m_p)^{\frac{3}{2}}}{h^3} \cdot \sqrt{E_V - E} \quad (\text{B.5})$$

where:

- m_n and m_p are the effective masses of an electron and a hole, respectively;
- h is the Planck's constant.

At the equilibrium, the electron concentration n_0 and the hole concentration p_0 are:

$$n_0 = \int_{E_C}^{E_{C_{max}}} f_0(E) \cdot N(E) dE \approx \int_{E_C}^{-\infty} f_0(E) \cdot N(E) dE \quad (\text{B.6})$$

$$p_0 = \int_{E_{V_{min}}}^{E_V} f_h(E) \cdot N(E) dE \approx \int_{-\infty}^{E_V} f_h(E) \cdot N(E) dE \quad (\text{B.7})$$

where $E_{C_{max}}$ is the top of the conduction band and $E_{V_{min}}$ is the bottom of the valence band.

$E_{C_{max}}$ and $E_{V_{min}}$ can be replaced by plus infinity for $E_{C_{max}}$ and minus in the case of $E_{V_{min}}$, because of a quick decreasing of the f_0 function when $E \gg E_F$ and a quick decreasing of the f_h function when $E_F \gg E$.

Integrals can be simplified for a non-degenerated semiconductor:

- $E_F < E_C - k \cdot T$ for the n-type semiconductor;
- $E_F > E_V + k \cdot T$ for the p-type semiconductor.

Thus, in the n-type non-degenerated semiconductor case, the Fermi-Dirac distribution can be approximated by the Boltzmann distribution function:

$$f_0(E) = \frac{1}{\exp(\frac{E-E_F}{k \cdot T}) + 1} \approx \exp(\frac{E_F - E}{k \cdot T}) \quad (\text{B.8})$$

From Equations B.6, B.7 and B.8, electron and hole concentrations can be analytically approximated by the following expressions:

$$n_0 = N_C \cdot \exp(-\frac{E_C - E_F}{k \cdot T}) \quad (\text{B.9})$$

$$p_0 = N_V \cdot \exp(\frac{E_V - E_F}{k \cdot T}) \quad (\text{B.10})$$

where:

- N_C is the so-called effective density of states in the conduction band;
- N_V is the so-called effective density of states in the valence one.

N_C and N_V are expressed by the following relationships:

$$N_C = 2 \cdot \frac{(2 \cdot \pi \cdot m_n \cdot k \cdot T)^{\frac{3}{2}}}{h^3} \quad (\text{B.11})$$

$$N_V = 2 \cdot \frac{(2 \cdot \pi \cdot m_p \cdot k \cdot T)^{\frac{3}{2}}}{h^3} \quad (\text{B.12})$$

Appendix C

Hall effect functions

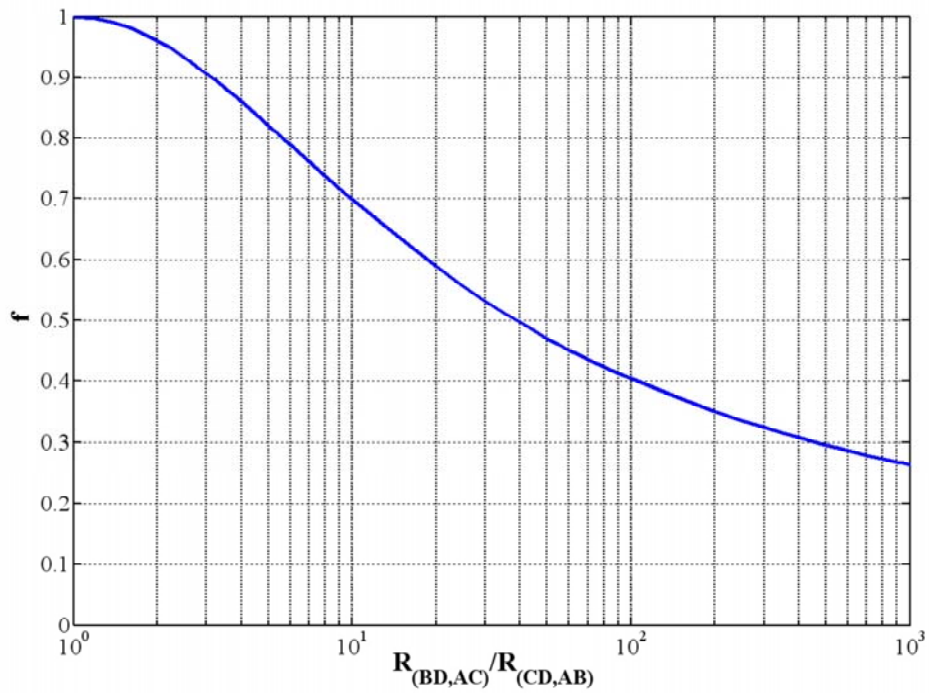


Figure C.1: Graphical representation of the function used in the Hall resistivity determination.

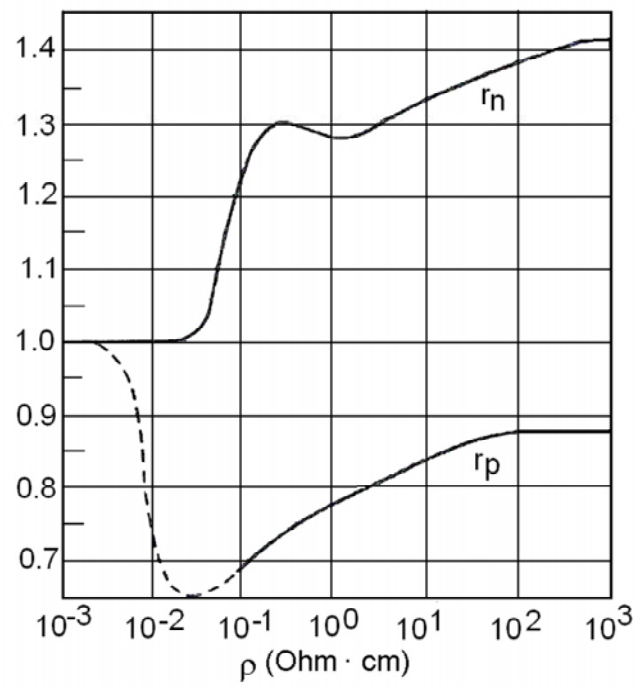


Figure C.2: Hall effect coefficient r_H versus Hall resistivity for silicon [91].

Appendix D

The configuration of Hall effect measurements

To obtain the sample resistivity, mobility and charge carrier density from the Van der Pauw method, measurements are done in two configurations: without and with magnetic field.

D.1 Configuration without magnetic field

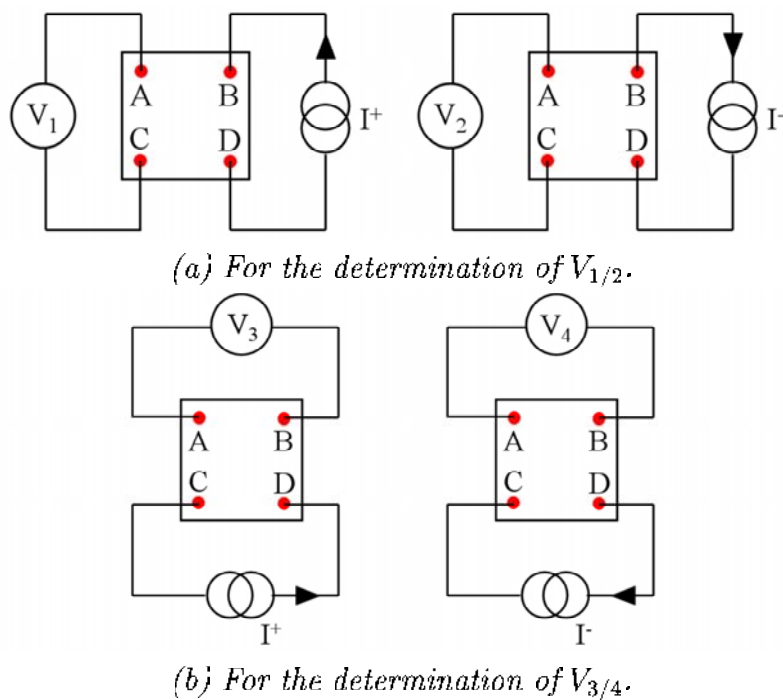


Figure D.1: Schemas of Hall effect measurements without magnetic field.

This configuration allows for measurements of the sample resistivity. Firstly, the Hall voltages are obtained:

$$V_{1/2} = V_A - V_C|_{I^+/I^-} \quad (\text{D.1})$$

$$V_{3/4} = V_A - V_B|_{I^+/I^-} \quad (\text{D.2})$$

Using these voltages the resistances $R_{(BD,AC)}$ and $R_{(CD,AB)}$ are calculated.

D.2 Configuration with magnetic field

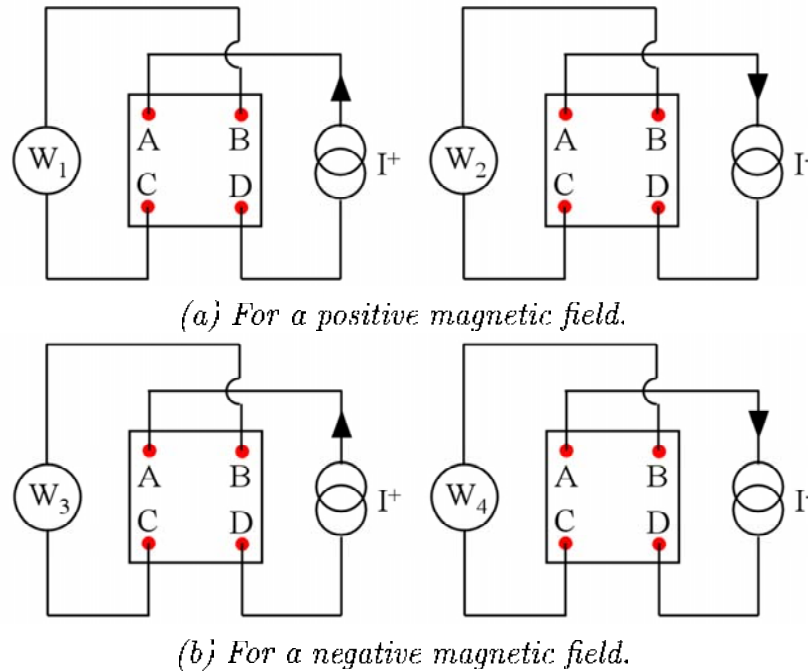


Figure D.2: Schemas of Hall effect measurements with magnetic field.

In this case, once the Hall resistivity obtained, Hall voltages measurements are performed with magnetic field. This is done to obtain the Hall constant and from its value the Hall mobility and charge carrier concentration are derived. Schemas of measurements of Hall voltages between contacts B and C with magnetic field oriented in two opposite directions are shown in Figure D.2.

Appendix E

Temperature regulation system

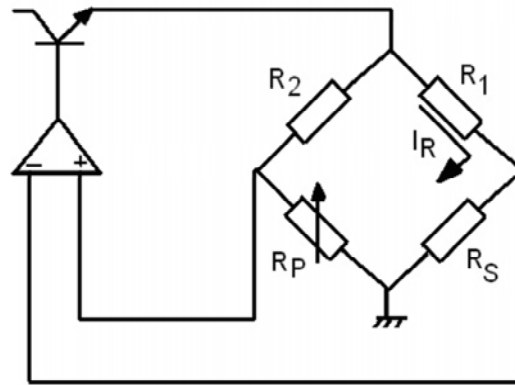


Figure E.1: *Electronic schema of temperature regulation system.*

Figure E.1 depicts the configuration of a Wheatstone bridge as the temperature control system. Branches of the Wheatstone bridge are constituted by the resistance of the substrate R_S , resistances R_1 and R_2 and also by the resistance of potentiometer R_P which it is possible to change using a handle.

When the Wheatstone bridge is in equilibrium, the relation between resistances is:

$$R_1 \cdot R_P = R_2 \cdot R_S \quad (\text{E.1})$$

The resistance of the potentiometer is equal to:

$$R_P = n \cdot R \quad (\text{E.2})$$

where n is the number of tours of the indicator and R is the variation of the resistance corresponding to one tour of the handle indicator. For the maximum number of tours, it is equal to $10 \text{ k}\Omega$:

$$n_{max} \cdot R = 10 \text{ k}\Omega \quad (\text{E.3})$$

The relation between n and resistances in the Wheatstone bridge is:

$$n = R_S \cdot R_2 \cdot R_1^{-1} \cdot R^{-1} \quad (\text{E.4})$$

While R_S as a function of temperature T is given by the following formula:

$$R_S(T) = R_0 \cdot (1 + \alpha \cdot T_S) \quad (\text{E.5})$$

where:

- T_S is the substrate temperature in °C,
- α is the constant coefficient of heater, determined experimentally by measuring R_S at two extreme temperatures,
- R_0 is the resistance of the substrate determined by measuring R_S at 0 °C.

Thus, the number of tours of the indicator as a function of temperature is given by Equation:

$$n = R_0 \cdot (1 + \alpha \cdot T_S) \cdot R_2 \cdot R_1^{-1} \cdot R^{-1} \quad (\text{E.6})$$

While replacing R_0 by the Equation E.5, the relation between the desired substrate temperature and the tour number is obtained by:

$$n = R_{S_c} \cdot (1 + \alpha \cdot T_S) \cdot (1 + \alpha \cdot T_0)^{-1} \cdot R_2 \cdot R_1^{-1} \cdot R^{-1} \quad (\text{E.7})$$

where:

- R_{S_c} is the resistance of the substrate at ambient temperature;
- T_0 is the ambient temperature.

Appendix F

Uncertainties of electrical measurements

For the measurements of the resistance and its changes due to gas action, the multimeter Keithley 2700 was used. The measurement mode is DC and the resistance range is 10 k Ω with a resolution of 10 m Ω . Thus, the accuracy of resistance measurements for 1 year is:

$$\Delta R = \pm (0.01\% \cdot rdg + 0.0006\% \cdot range) \quad (F.1)$$

For Hall effect measurements, estimated uncertainties on ρ , μ and n magnitude are computed using total differentials. The total differential of ρ is as following:

$$d\rho = \left| \frac{\partial \rho}{\partial d} \right| \cdot \Delta d + \left| \frac{\partial \rho}{\partial R_{(BD,AC)}} \right| \cdot \Delta R_{(BD,AC)} + \left| \frac{\partial \rho}{\partial R_{(CD,AB)}} \right| \cdot \Delta R_{(CD,AB)} \quad (F.2)$$

where Δd is equal to $\pm 20\%$ and the accuracy of measured resistances $R_{(BD,AC)}$ is:

$$\Delta R_{(BD,AC)} = \left| \frac{\partial R_{(BD,AC)}}{\partial V_A} \right| \cdot \Delta V_A + \left| \frac{\partial R_{(BD,AC)}}{\partial V_B} \right| \cdot \Delta V_B + \left| \frac{\partial R_{(BD,AC)}}{\partial I_{BD}} \right| \cdot \Delta I_{BD} \quad (F.3)$$

where ΔV_A and ΔV_B are measured by a Microvolt DMM Keithley Model 177 with a range of 200 mV. Its accuracy is equal to:

$$\Delta V = \pm (0.04\% \cdot rdg + 1 \cdot count) \quad (F.4)$$

The current is measured by a Keithley 197 multimeter with a range of 200 μ A and a resolution of 1 nA. Its accuracy is:

$$\Delta I = \pm (0.1\% \cdot rdg + 15 \cdot counts) \quad (F.5)$$

Similarly, is derived for for $R_{(CD,AB)}$.

Uncertainties on μ and for n are calculated as follows:

$$d\mu = \left| \frac{\partial \mu}{\partial R_H} \right| \cdot \Delta R_H + \left| \frac{\partial \mu}{\partial \rho} \right| \cdot \Delta \rho \quad (\text{F.6})$$

$$dn = \left| \frac{\partial n}{\partial R_H} \right| \cdot \Delta R_H \quad (\text{F.7})$$

In addition, the uncertainties on ΔR_H is equal to:

$$dR_H = \left| \frac{\partial R_H}{\partial R_{(AD,BC)}} \right| \cdot \Delta R_{(AD,BC)} + \left| \frac{\partial R_H}{\partial d} \right| \cdot \Delta d + \left| \frac{\partial R_H}{\partial B} \right| \cdot \Delta B \quad (\text{F.8})$$

where ΔB is equal to $\pm 10\%$ and $\Delta R_{(AD,BC)}$ is estimated analogically to $R_{(BD,AC)}$ and $R_{(CD,AB)}$; the magnetic field is measured by a Hall probe that is in our case a Model 810 Field Monitor Bell inc.

Appendix G

Principle of Hall effect measurements

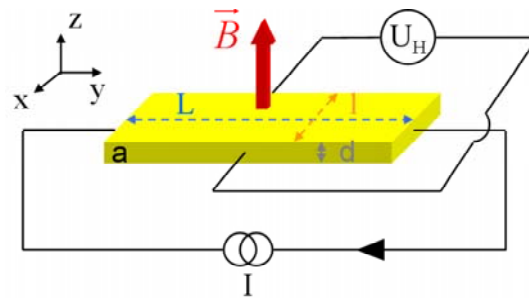


Figure G.1: *Principle of Hall effect measurements [91].*

In Hall effect measurements, the considered sample is a homogeneous (e.g., n-doped) semiconductor. In Figure G.1, the semiconductor sample with dimensions (L, l, d) is represented. The current I in the discussed example flows in the y -direction. In the presence of a magnetic field \vec{B} along z -axis, electrons experience a force driving them towards the side a . This force is the Lorentz force defined by:

$$\vec{F} = -q \cdot (\vec{v} \times \vec{B}) \quad (\text{G.1})$$

where q is the charge, \vec{v} and \vec{B} are the velocity of the electrons and the magnetic field respectively.

This net charge displacement results in the side b becoming positively charged and the side a negatively charged. This creates an electric field \vec{E}_x , which exerts a force \vec{F}' (equal and opposite to the Lorentz force) on the electrons. \vec{F}' is given by:

$$\vec{F}' = -q \cdot \vec{E}_x \quad (\text{G.2})$$

At equilibrium, we have:

$$\vec{F}' + \vec{F} = \vec{0} \quad (\text{G.3})$$

thus:

$$-q \cdot \vec{E}_x - q \cdot (\vec{v} \times \vec{B}) = \vec{0} \quad (\text{G.4})$$

Taking into account the sense of vectors \vec{E}_x , \vec{v} and \vec{B} :

$$\vec{E}_x - (\vec{v} \cdot \vec{B}) = 0 \quad (\text{G.5})$$

the current density going cross the sample is:

$$j = \frac{I}{l \cdot d} = -n \cdot q \cdot \frac{dx}{dt} = -n \cdot q \cdot v \quad (\text{G.6})$$

where n is the density of electrons (charge carrier concentration in the case of a n -type semiconductor).

From equations G.5 and G.6, we obtain:

$$E_x = v \cdot B = -\frac{j \cdot B}{n \cdot q} = \frac{-1}{n \cdot q} \cdot \frac{I \cdot B}{l \cdot d} \quad (\text{G.7})$$

where $\frac{-1}{n \cdot q}$ is the Hall constant and noted R_H .

To determine R_H , the Hall voltage U_H is measured:

$$U_H = R_H \cdot \frac{J \cdot B}{d} \quad (\text{G.8})$$

Once R_H has been determined, one can estimate the charge carrier concentration n and the Hall mobility μ_H for the sample characterised by the continuous ρ :

$$n = \frac{1}{q \cdot |R_H|} \quad (\text{G.9})$$

$$\mu_H = \frac{1}{n \cdot q \cdot \rho} = \frac{1}{\rho} |R_H| \quad (\text{G.10})$$

with:

$$\rho = \frac{U_H}{I} \cdot \frac{l \cdot d}{L} \quad (\text{G.11})$$

From μ_H , the mobility of electrons μ can be obtained by using the following equation:

$$\mu = r_H \cdot \mu_H \quad (\text{G.12})$$

where r_H is the Hall coefficient.

References

- [1] **Institute for ecology and industrial areas, Katowice**
<http://www.ietu.katowice.pl/>
- [2] **Institute for ecology and industrial areas, Poznan**
<http://www.poznan.pios.gov.pl>
- [3] **ATMO Auvergne**
<http://www.atmoauvergne.asso.fr/>
- [4] **W. Gopel, K.D. Schierbaum**
Sensors: a comprehensive survey, Wiley-VCH, 1991.
- [5] **S. Zhuiykov, T. Ono, N. Yamazoe, N. Miura**
High-temperature NO_x sensors using zirconia solid electrolyte and zinc family oxide sensing electrode, *Solid States Ionics*, vol. 152–153, pp. 801–807, 2002.
- [6] **K. Galatsis, Y.X. Li, W. Wlodarski, E. Comini et al.**
Comparison of single binary oxide MoO₃, TiO₂ and WO₃ sol-gel gas sensors, *Sensors and Actuators*, vol. B83, pp. 276–280, 2002.
- [7] **K. Galatsis, Y.X. Li, W. Wlodarski, E. Comini et al.**
Semiconductor MoO₃-TiO₂ thin film gas sensor, *Sensors and Actuators*, vol. B77, pp. 472–477, 2001.
- [8] **M. Ivanovskaya, D. Kotsikau, G. Faglia, P. Nelli et al.**
Gas sensitive properties of thin film heterojunction structures based on Fe₂O₃-In₂O₃ nanocomposites, *Sensors and Actuators*, vol. B93, pp. 422–430, 2003.
- [9] **M. Ivanovskaya, A. Gurlo, P. Bogdanov**
Mechanism of O₃ and NO₂ detection and selectivity of In₂O₃ sensors, *Sensors and Actuators*, vol. B77, pp. 264–267, 2001.

- [10] **M. Ivanovskaya, P. Bogdanov, G. Faglia, G. Sberveglieri**
The features of thin films and ceramic sensors at the detection of CO and NO₂, Sensors and Actuators, vol. B68, pp. 344–350, 2000.
- [11] **G.G. Mandayo, E. Castano, F.J. Gracia, A. Cirera et al.**
Strategies to enhance the carbon monoxide sensitivity of tin oxide thin films, Sensors and Actuators, vol. B95, pp. 90–93, 2003.
- [12] **M. Bouvet, A. Leroy, J. Simon, F. Tournilhac et al.**
Detection and titration of ozone using metallophthalocyanine based field effect transistors, Sensors and Actuators, vol. B72(1), pp. 86–93, 2001.
- [13] **M. Bouvet, A. Pauly**
Molecular semiconductor-based gas sensors, Encyclopedia of Sensors, vol. 6, pp. 227–269, 2006.
- [14] **J. Brunet, L. Talazac, V. Battut, A. Pauly et al.**
Evaluation of atmospheric pollution by two semiconductor gas sensors, Thin Solids Films, vol. 391, pp. 308–313, 2001.
- [15] **J. Brunet**
Etudes, élaboration et tests de dispositifs capteurs de gaz à semi-conducteurs destinés à la mesure de la pollution atmosphérique, Ph.D. Thesis, Blaise Pascal University, Clermont-Ferrand, 2003.
- [16] **R.D. Gould, N.A. Ibrahim**
The electrical response of evaporated cobalt phthalocyanine thin films on exposure to NO₂, Thin Solid Films, vol. 398–399, pp. 432–437, 2001.
- [17] **Y.L. Lee, C.Y. Sheu, R.H. Hsiao**
Gas sensing characteristic of copper phthalocyanine films: effects of film thickness and sensing temperature, Sensors and Actuators, vol. B99, pp. 281–287, 2004.
- [18] **H. Hasegawa**
Control of surfaces and heterointerfaces of AlGa_N/Ga_N system for sensor devices and their on-chip integration on nanostructures, Current Applied Physics, vol. 7, pp. 318–327, 2007.
- [19] **L. Mazet**
Réalisation et caractérisation de structures microélectroniques à base de semi-conducteur III-V (InP). Application capteurs de gaz, Ph.D. Thesis, Blaise Pascal University, Clermont-Ferrand, 2004.
- [20] **K. Wierzbowska, B. Adamowicz, L. Mazet, J. Brunet et al.**
High-sensitivity NO₂ sensor based on n-type InP epitaxial layers, Optica Applicata, vol. 35, n°3, pp. 654–662, 2005.

- [21] **K. Wierzbowska, A. Pauly, B. Adamowicz, L. Bideux**
Studies of gas sensing, electrical and chemical properties of n-InP epitaxial surfaces, *Physica Status Solidi (a)*, vol. 203, n°9, pp. 2281–2286, 2006.
- [22] **K. Wierzbowska, L. Bideux, B. Adamowicz, A. Pauly**
A novel III-V semiconductor material for NO₂ detection and monitoring, *Sensors and Actuators*, vol. A, in press.
- [23] **V. Battut**
Nouveaux matériaux sensibles pour capteurs de gaz à semi-conducteurs: polypyrroles mésomorphes et InP, Ph.D. Thesis, Blaise Pascal University, Clermont-Ferrand, 1997.
- [24] **V. Battut, J.P. Blanc, C. Maleysson**
Gas sensitivity of InP epitaxial thin layers, *Sensors and Actuators*, vol. B44, pp. 503–506, 1997.
- [25] **V. Battut, J.P. Blanc, E. Goumet, V. Souliere et al.**
NO₂ sensor based on InP epitaxial thin layers, *Thin Solid Films*, vol. 348, pp. 266–272, 1999.
- [26] **L. Talazac**
Capteurs de gaz oxydants à base de phosphore d'indium (InP) monocristallin. Application à l'évaluation de la pollution atmosphérique en milieu urbain, Ph.D. Thesis, University of Blaise Pascal, Clermont-Ferrand, 2000.
- [27] **L. Talazac, J. P. Blanc, J.P. Germain, A. Pauly**
NO₂ detection by a resistive device based on n-InP epitaxial layers, *Sensors and Actuators*, vol. B59, pp. 89–93, 1999.
- [28] **H. Hasegawa**
Fermi level pinning and Schottky barrier height control at metal-semiconductor interfaces of InP and related materials, *Japanese Journal of Applied Physics*, vol. 38, pp. 1098–1102, 1999.
- [29] **B. Adamowicz, M. Miczek, C. Brun, B. Gruzza et al.**
Rigorous analysis of the electronic properties of InP interfaces for gas sensing, *Thin Solids Films*, vol. 436, pp. 101–106, 2003.
- [30] **B. Adamowicz, H. Hasegawa**
Computer analysis of surface recombination process at Si and compound semiconductor surfaces and behavior of surface recombination velocity, *Japanese Journal of Applied Physics*, vol. 37, pp. 1631–1637, 1998.
- [31] **B. Adamowicz, H. Hasegawa**
Computer analysis of photon-induced non-equilibrium phenomena at Si and AlGaAs surfaces, *Vacuum*, vol. 57, pp. 111–120, 2000.

- [32] **L. Talazac, J.P. Blanc, V. Battut, F. Mollot**
NO₂ sensitivity of thin n-InP epitaxial layers, Electron Technology, vol. 33, pp. 213–216, 2000.
- [33] **L. Talazac, J. Brunet, V. Battut, J.P. Blanc et al.**
Air quality evaluation by monolithic InP-based resistive sensors, Sensors and Actuators, vol. B76, pp. 258–264, 2001.
- [34] **L. Talazac, F. Barbarin, C. Varenne, Y. Cuminal**
Highly NO₂ sensitive pseudo Schottky barrier diodes on p-type InP with improved electrical characteristics, Sensors and Actuators, vol. B77, pp. 447–454, 2001.
- [35] **L. Talazac, F. Barbarin, C. Varenne, L. Mazet et al.**
Gas sensing properties of pseudo-Schottky diodes on p-type indium phosphide substrates application to O₃ and NO₂ monitoring in urban ambient air, Sensors and Actuators, vol. B83, pp. 149–159, 2002.
- [36] **B. Adamowicz, M. Miczek, H. Hasegawa**
Computer analysis of the Fermi level behaviour at SiO₂/n-Si and SiO₂/n-GaAs interfaces, Electron Technology, vol. 33, pp. 249–252, 2000.
- [37] **H. Hasegawa**
Passivation and control of semiconductor interfaces by interface control layer, Material Science Forum, vol. 185–188, pp. 23–36, 1995.
- [38] **H. Hasegawa, T. Sato, T. Hashizume**
Evolution mechanism of nearly pinning-free platinum/n-type indium phosphide interface with a high Schottky barrier height by in-situ electrochemical process, Journal of Vacuum Science and Technology, vol. B15(4), pp. 1227–1235, 1997.
- [39] **H. Hasegawa, T. Sawada**
On the electrical properties of compound semiconductor interfaces in metal/insulator/semiconductor structures and the possible origin of interface states, Thin Solid Films, vol. 103, pp. 119–140, 1983.
- [40] **H. Hasegawa, L. He, H. Ohno, T. Sawada et al.**
Electronic and microstructural properties of disorder-induced gap states at compound semiconductor-insulator interfaces, Journal of Vacuum Science and Technology, vol. B5(4), pp. 1097–1107, 1987.
- [41] **Wikipedia**
<http://en.wikipedia.org/>
- [42] **Auto-online**
<http://www.auto-online.pl/>

- [43] **European Commission**
<http://ec.europa.eu/>
- [44] **AEA energy and environment**
<http://www.aeat.co.uk/>
- [45] **ATMO Picardie**
<http://www.atmo-picardie.com/>
- [46] **E. Comini, G. Faglia, G. Sberveglieri**
UV light activation of tin oxide thin films for NO₂ sensing at low temperatures, Sensors and Actuators, vol. B78, pp. 73–77, 2001.
- [47] **T. Okumura**
Hydrogen-related issues in GaAs Schottky Contacts, GaAs Manteck, Vancouver, 1999.
- [48] **K. Matsuo, N. Negoro, J. Kotani, T. Hashizume et al.**
Pt Schottky diode gas sensors formed on GaN and AlGaN/GaN heterostructure, Applied Surface Science, vol. 244, pp. 273–276, 2005.
- [49] **E. Souteyrand**
Transduction électrique pour la détection de gaz, CMC2, Les capteurs chimiques, pp. 52–62, 1997.
- [50] **S. M. Sze**
Physics of Semiconductor Devices, John Wiley and Sons, 1981.
- [51] **T. Becker, S. Ahlers, C. Braunmuhl, G. Muller et al.**
Gas sensing properties of thin- and thick-film tin-oxide materials, Sensors and Actuators, vol. B77, pp. 55–61, 2001.
- [52] **Y. Shimizu, N. Matsunaga, T. Hyodo, M. Egashira**
Improvement of SO₂ sensing properties of WO₃ by noble metal loading, Sensors and Actuators, vol. B77, pp. 35–40, 2001.
- [53] **K.C. Ho, Y.H. Tsou**
Chemiresistor-type NO gas sensor based on nickel phthalocyanine thin films, Sensors and Actuators, vol. B77, pp. 253–259, 2001.
- [54] **R. Tongpool**
Effect of nitrogen dioxide and temperature on the properties of lead phthalocyanine in polypyrrole, Thin Solid Films, vol. 438–439, pp. 14–19, 2003.
- [55] **C.M. Dooling, T.H. Richardson, L. Valli, R. Rella et al.**
NO₂ sensitivity of gadolinium bis-phthalocyanine assemblies prepared by ultra-fast LB deposition, Colloids and Surface A: Physicochemical and Engineering Aspects, vol. 198–200, pp. 791–796, 2002.

- [56] **W. Shockley**
Electrons and holes in semiconductors in transistors electronic application, PWN, 1956. In Polish.
- [57] **K.W. Szalimowa**
Physics of semiconductors, PWN, 1974. In Polish.
- [58] **H. Mathieu**
Physique des semiconducteurs et des composants électroniques, Masson, 1987.
- [59] **R.H. Williams, I.T. McGovern**
Surface characterisation of indium phosphide, Surface Science, vol. 51, pp. 14–28, 1975.
- [60] **A. Szaynok, S. Kuzminski**
Principles of the physics of semiconductors, WNT, 2000. In Polish.
- [61] **M. Miczek**
Electronic properties of III-V semiconductor surfaces from computer-aided photoluminescence efficiency studies, Ph.D. Thesis, Silesian University of Technology, Gliwice, 2003.
- [62] **W.E. Spicer, I. Lindau, P. Skeath, C.Y. Su**
Unified defect model and beyond, Journal of Vacuum Science and Technology, vol. 17(5), pp. 1019–1027, 1980.
- [63] **W.E. Spicer, P.W. Chye, P.R. Skeath, C.Y. Su et al.**
New and unified model for Schottky barrier and III-V insulator interface states formation, Journal of Vacuum Science and Technology, vol. 16(5), pp. 1422–1433, 1979.
- [64] **N. Kinrot, Y. Shapira**
Surface electronic structure of p-InP using temperature-controlled surface photovoltage spectroscopy, Physical Review, vol. B65(24), pp. 245303–245308, 2002.
- [65] **R.M. Feenstra**
Formation of metal/GaAs(110) interfaces studied by scanning tunneling microscopy, Applied Surface Science, vol. 56–58, pp. 104–116, 1992.
- [66] **V. Ramachandran, R.M. Feenstra**
Scanning tunnelling spectroscopy of Mott-Hubbard states on the 6H-SiC(0001) $\sqrt{3} \times \sqrt{3}$ surface, Physical Review Letters, vol. 82, n°5, pp. 1000–1003, 1999.

- [67] **W. Monch**
Metal-semiconductor contacts: electronic properties, Surface Science, vol. 299/300, pp. 928–944, 1994.
- [68] **W. Monch**
Chemical trends of barrier heights in metal-semiconductor contacts: on the theory of the slope parameter, Applied Surface Science, vol. 92, pp. 367–371, 1996.
- [69] **T. Sawada, K. Numata, S. Tohdoh, T. Saitoh et al.**
In-situ characterisation of compound semiconductor surfaces by novel photoluminescence surface state spectroscopy, Japanese Journal of Applied Physics, vol. 32, pp. 511–517, 1993.
- [70] **H. Hasegawa, M. Akazawa, K. Matsuzaki, H. Ishii et al.**
GaAs and $In_{0.53}Ga_{0.47}As$ MIS structures having an ultrathin pseudomorphic interface control layer of Si prepared by MBE, Japanese Journal of Applied Physics, vol. 27(12), pp. L2265–L2267, 1988.
- [71] **A. Guivarc’h, H. L’Haridon, G. Pelous, G. Hollinger et al.**
Chemical cleaning of InP surfaces: Oxide composition and electrical properties, Journal of Applied Physics, vol. 55(4), pp. 1139–1148, 1984.
- [72] **G. Hollinger, E. Bergignat, J. Joseph, Y. Robach**
On the nature of oxides on InP surface, Journal of Vacuum Science and Technology, vol. A3(6), pp. 2082–2088, 1985.
- [73] **G. Hollinger, J. Joseph, Y. Robach, E. Bergignat et al.**
On the chemistry of passivated oxide-InP interfaces, Journal of Vacuum Science and Technology, vol. B5(4), pp. 1108–1112, 1987.
- [74] **A. Nelson, K. Geib, C.W. Wilmsen**
Composition and structure of thermal oxides of indium phosphide, Journal of Applied Physics, vol. 54(7), pp. 4134–4140, 1983.
- [75] **S.J. Sferco, G. Allan, I. Lefebvre, M. Lannoo et al.**
Electronic structure of semiconductor oxides: $InPO_4$, $In(PO_3)_3$, P_2O_5 , SiO_2 , $AlPO_4$ and $Al(PO_3)_3$, Physical Review B, vol. 42, n°17, pp. 11232–11239, 1990.
- [76] **G.P. Schwartz, W.A. Sunder, J.E. Griffiths**
The In-P-O Phase Diagram: Construction and Applications, J. Electrochem. Soc.: Solid-State Science and Technology, vol. 129, n°6, pp. 1361–1397, 1982.
- [77] **J.F. Wager, K.M. Geib, C.W. Wilmsen, L.L. Kazmerski**
Native oxide formation and electrical instabilities at the insulator/InP

- interface*, Journal of Vacuum Science and Technology, vol. B1(3), pp. 778–781, 1983.
- [78] **J.F. Wager, C.W. Wilmsen**
Thermal oxidation of InP, Journal of Applied Physics, vol. 51(1), pp. 812–814, 1980.
- [79] **J. Zemek, O.A. Baschenko, M.A. Tyzykhov**
Non-destructive concentration depth profiling of native -oxide/InP (100) samples by angle-resolved X-ray induced photoelectron spectroscopy: effect of annealing, Thin Solids Films, vol. 224, pp. 141–147, 1993.
- [80] **F.L. Slejko**
Adsorption Technology, Marcel Dekker, 1985.
- [81] **M. Suzuki**
Adsorption Engineering, Elsevier, 1990.
- [82] **J.E. Lennard-Jones**
Cohesion, Proceedings of the Physical Society, vol. 43, pp. 461–482, 1931.
- [83] **J. Oscik**
Adsorption, PWN, 1973. In Polish.
- [84] **I. Langmuir**
The adsorption of gases on plane surfaces of glass, mica and platinum, Journal of the American Chemical Society, vol. 40, pp. 1361–1402, 1918.
- [85] **H. Freundlich**
Über die Adsorption in Lösungen, Zeitschrift für Physikalische Chemie, vol. 57, pp. 385–470, 1907.
- [86] **V.M. Aroutiounian, G.S. Aghababian**
To the theory of semiconductor gas sensors, Sensors and Actuators, vol. B50, pp. 80–84, 1998.
- [87] **H. Geistlinger**
Electron theory of thin-film gas sensors, Sensors and Actuators, vol. B17, pp. 47–60, 1993.
- [88] **A. Zangwill**
Physics at Surfaces, Cambridge University Press, 1988.
- [89] **J. Achard**
Contribution à l'étude du transport électronique dans les systèmes multicouches à base de semi-conducteurs III-V, Ph.D. Thesis, University of Blaise Pascal, Clermont-Ferrand, 1997.

- [90] **L.J. Van der Pauw**
A method of measuring specific resistivity and Hall effect of discs of arbitrary shape, Philips Research Reports, vol. 13, pp. 1–9, 1958.
- [91] **A. Vapaille, R. Castagne**
Dispositifs et circuits intégrés semiconducteurs, Dunod, 1987.
- [92] **M. Petit**
Etude par spectroscopies électroniques de la nitruration du phosphore d'indium, Ph.D. Thesis, University of Blaise Pascal, Clermont-Ferrand, 2004.
- [93] **L. Bideux, D. Baca, B. Gruzza, V. Matolin et al.**
Surface modification of GaAs during argon ionic cleaning and nitridation: EELS, EPES and XPS studies, Surface Science, vol. 566–568, pp. 1158–1162, 2004.
- [94] **M. Grasserbauer, H.J. Dudek, M.F. Ebel**
Angewandte Oberflächenanalyse, Springer, 1986.
- [95] **S. Tanuma, C.J. Powell, D.R. Penn**
Calculations of electron inelastic mean free paths (IMFPPS). IV. Evaluation of calculated IMFPPs and of the predictive IMFPP formula TPP-2 for electron energies between 50 and 2000 eV, Surface and Interface Analysis, vol. 20(1), pp. 77–89, 1993.
- [96] **A. Jablonski, B. Lesiak, L. Zommer, M.F. Ebel et al.**
Quantitative analysis by XPS using the multiline approach, Surface and Interface analysis, vol. 21(10), pp. 724–730, 1994.
- [97] **M. Pijolat, G. Hollinger**
New depth-profiling method by angular-dependent X-ray photoelectron spectroscopy, Surface Science, vol. 105, pp. 114–128, 1981.
- [98] **M.P. Seah, W.A. Dench**
Quantitative electron spectroscopy of surfaces: a standard data base for electron inelastic mean free paths in solids, Surface and Interface Analysis, vol. 1(1), pp. 2–11, 1979.
- [99] **C.D. Wagner, L.E. Davis, W.M. Riggs**
The energy dependence of the electron mean free path, Surface and Interface Analysis, vol. 2(2), pp. 53–55, 1980.
- [100] **K. Siegbahn, C. Nordling, A. Fahlman et al.**
ESCA : Atomic Molecular and Solid State Structure Studied by Means of Electrons Spectroscopy, Almquist and Wiksells, 1967.

- [101] **J.F. Moulder, W.F. Stickle, P.E. Sobol, K.D. Bomben**
Handbook of X-ray Photoelectron Spectroscopy, Physical Electronics Division, 1992.
- [102] **M. Ikeo, Y. Iijina, N. Nimura, M. Sigematsu et al.**
Handbook of X-ray photoelectron spectroscopy, Serving Advanced Technology, 1991.
- [103] **P. Auger**
The compound photoelectric effect, Journal de Physique et Radium, vol. 6, pp. 205–208, 1925.
- [104] **D.H. Narumand, K.D. Childs**
Auger spectrometers: a tutorial review, Applied Spectroscopy Reviews, vol. 34(3), pp. 139–158, 1999.
- [105] **M.F. Chung, L.H. Jenkins**
Auger electron energies of the outer shell electron, Surface Science, vol. 22, pp. 479–485, 1970.
- [106] **P.W. Palmberg, F.E. Riach, R.E. Weber, N.C. MacDonald**
Handbook of Auger electron spectroscopy, Physical Electronics Division, 1976.
- [107] **L. Bideux, D. Baca, B. Gruzza, V. Matolin et al.**
Surface modification of GaAs during argon ionic cleaning and nitridation: EELS, EPES and XPS studies, Surface Science, vol. 566–568, pp. 1158–1162, 2004.
- [108] **H. H. Andersen**
The depth resolution of sputter profiling, Applied Physics, vol. 18, pp. 131–140, 1979.
- [109] **A. Zalar, B. Pracek, P. Panjan**
Effects of surface structure on depth resolution of AES depth profiles of Ni/Cr multilayers, Surface and Interface Analysis, vol. 30, pp. 247–250, 2000.
- [110] **J.S. Pan, S.T. Tay, C.H.A. Huan, A.T.S. Wee**
XPS study of incident angle effects on the ion beam modofocation of InP surfaces by 6 keV O_2^+ , Surface and Interface Analysis, vol. 27, pp. 993–997, 1999.
- [111] **T. Saitoh, H. Iwadate, H. Hasegawa**
In-Situ surface state spectroscopy by photoluminescence and surface current transport for compound semiconductors, Japanese Journal of Applied Physics, vol. 30, pp. 3750–3754, 1991.

- [112] **M. Benzaquen, D. Walsh, K. Mazuruk**
High-temperature mobility of pure n-type InP epitaxial layers, Physical Review, vol. B36(8), pp. 4388–4393, 1987.
- [113] **R.M. Feenstra, M.A. Lutz**
Scattering from strain variations in high -mobility Si/SiGe heterostructures, Journal of Applied Physics, vol. 78, pp. 6091–6097, 1995.
- [114] **D.K. Hamilton**
Estimation of the conduction band deformation potential in indium phosphide from the temperature variation of drift mobility, Solid-State Electronics, vol. 24, pp. 317–319, 1981.
- [115] **Y. Liu, H. Wong, K. Radhakrishnan**
Increase in electron mobility of InGaAs/InP composite channel high electron mobility transistor structure due to SiN passivation, Thin Solids Films, vol. 515 (10), pp. 4387–4389, 2007.
- [116] **O. Madelung, M. Shulz, H. Weiss**
Landolt-Bornstein: Numerical data and functional relationships in Science and Technology, O. Madelung, vol.17, 1982.
- [117] **S.N. Mohammad, A.V Bemis, R.L. Carter, R.B. Renbeck**
Temperature, electric field, and doping dependent mobilities of electrons and holes in semiconductors, Solid-State Electronics, vol. 36, n°12, pp. 1677–1683, 1993.
- [118] **J. Oswald**
Schottky diodes with a -doped near-surface region, Journal of Applied Physics, vol. 90 (12), pp. 6205–6209, 2001.
- [119] **K. Radhakrishnan, H.Q. Zheng, P.H. Zhane et al.**
Characterization of silicon-doped InP grown by solid-source molecular beam epitaxy using a valved phosphorous cracker cell, Journal of Crystal Growth, vol. 204, pp. 275–281, 1999.
- [120] **J.R. Schrieffer**
Effective carrier mobility in surface-space charge layers, Physical Review, vol. 97, n°3, pp. 641–645, 1954.
- [121] **Y.W. Zhao, Z.Y. Dong, C.J. Li**
Approach for defect suppression and preparation of high quality semi-insulating InP, Journal of Crystal Growth, vol. 275, pp. e381-e385, 2005.
- [122] **Physico Technical Institute**
<http://www.ioffe.rssi.ru/>

List of publications

Journal papers

- [P1] **L. Berry, J. Brunet, C. Varenne, L. Mazet et al.**
NO₂ gas sensing studies: impact of geometrical and physical characteristic of ohmic contacts on n-InP epitaxial layer, Materials Science and Engineering: C, vol. 27(4), pp 654–658, 2007.
- [P2] **J. Brunet, A. Pauly, L. Mazet, C. Varenne et al.**
Molecular semiconductors based gas sensors dedicated to selective oxidising pollutants evaluation, Journal of Porphyrins and Phthalocyanines, vol. 10(4-6), pp 812, 2006.
- [P3] **L. Mazet, C. Varenne, J. Brunet, K. Wierzbowska et al.**
An original methodology dedicated to real-time detection of oxidizing gases based on pseudo-Schottky diode junction, Sensors and Actuators B: Chemical 2, in press.
- [P4] **A. Pauly, J. Brunet, K. Wierzbowska, L. Mazet et al.**
Molecular materials dedicated to gas sensor applications: molecular engineering, design of micro-systems and urban air quality control applications, Journal of Porphyrins and Phthalocyanines, vol. 10(4-6), pp 368, 2006.
- [P5] **C. Varenne, L. Mazet, J. Brunet, K. Wierzbowska et al.**
Improvement in lifetime of pseudo-Schottky diode sensor: towards selective detection of O₃ in gaseous mixture (O₃, NO₂), Thin Solid Films, vol. 516, pp. 2237–2243, 2008.
- [P6] **K. Wierzbowska, B. Adamowicz, L. Mazet, J. Brunet et al.**
High-sensitivity NO₂ sensor based on n-type InP epitaxial layers, Optica Applicata, vol. 35, n°3, pp. 654–662, 2005.

- [P7] **K. Wierzbowska, A. Pauly, B. Adamowicz, L. Bideux**
Studies of gas sensing, electrical and chemical properties of n-InP epitaxial surfaces, Physica Status Solidi (a), vol. 203, n°9, pp. 2281–2286, 2006.
- [P8] **K. Wierzbowska, L. Bideux, B. Adamowicz, A. Pauly**
A novel III-V semiconductor material for NO₂ detection and monitoring, Sensors and Actuators, vol. A 142, pp. 237–241, 2008.
- [P9] **K. Wierzbowska, B. Adamowicz, B. Lauron, L. Bideux et al.**
Rigorous analysis of electronic properties and AFM studies of oxidising gas sensitive n-InP epitaxial layers, Journal of Physics, in press.

Conference papers

- [P10] **B. Adamowicz, M. Miczek, K.B. Wierzbowska, H. Hasegawa**
Rigorous analysis of the contribution of surface states to the conductivity of semiconductor thin layers, Fall Meeting of the European Materials Research Society, Warsaw, 2004.
- [P11] **L. Berry, J. Brunet, C. Varenne, L. Mazet et al.**
Influence of technological process steps on the reproducibility, sensitivity and stability of InP based resistive gas sensors, Eurosensors XIX, Barcelone, 2005.
- [P12] **L. Bideux, K. Wierzbowska, A. Pauly**
XPS study of the properties of III-V compounds used for NO₂ and O₃ detection, European Conference on Surface Science, Paris, 2006.
- [P13] **L. Mazet, C. Varenne, J. Brunet, A. Pauly et al.**
An original methodology of measurements for ozone detection in a mix (O₃, NO₂) with pseudo-Schottky Pd-InP gas sensor, Eurosensors XIX, Barcelone, 2005.
- [P14] **A. Pauly, J. Brunet, K. Wierzbowska, L. Mazet et al.**
Molecular materials dedicated to gas sensor applications: molecular engineering, design of micro-systems and urban air quality control applications, International Conference on Porphyrins and Phthalocyanines, Rome, 2006.
- [P15] **K. Wierzbowska, B. Adamowicz, L. Mazet, J. Brunet et al.**
High-sensitivity NO₂ sensor based on n-type InP epitaxial layers, X Seminarium Powierzchnia i Struktury Cienkwarstwowe, Wroclaw, 2005.
- [P16] **K. Wierzbowska, B. Adamowicz, M. Miczek, L. Mazet et al.**
The studies on chemical, electronic and sensing properties of devise based

on n-InP epitaxial layers, Fall Meeting of the European Materials Research Society, Warsaw, 2005.

- [P17] **K. Wierzbowska, A. Pauly, L. Bideux, B. Adamowicz et al.**
A novel III-V semiconductor material for NO₂ detection and monitoring, Eurosensors XX, Göteborg, 2006.
- [P18] **K. Wierzbowska, B. Adamowicz, B. Lauron, L. Bideux et al.**
Rigorous analysis of electronic properties and chemical studies of oxidizing gases sensitive n-InP epitaxial layers, 17th International Vacuum Congress, 13th International Conference on Surfaces Science and International Conference on Nano Science and Technology, Stockholm, 2007.

Résumé

Cette thèse est consacrée à l'étude de la physico-chimie des structures électroniques et microélectroniques à base de phosphure d'indium (InP). Le contexte scientifique de cette étude est tout d'abord abordé dans une description de la pollution atmosphérique ainsi que de sa métrologie. Les propriétés physico-chimiques et électroniques de InP sont particulièrement détaillées. Les structures des capteurs de gaz en cours de développement pour cette application sont ensuite répertoriées. Les méthodes de caractérisation chimique (spectroscopie de surface de type XPS et Auger, microscopie à force atomique AFM) et électronique (Van der Pauw) ainsi que l'analyse théorique des propriétés électroniques des couches minces sont également présentées. Enfin, des mesures en laboratoire à température et concentration variables de NO₂ proches de celles rencontrées dans une atmosphère urbaine sont présentées. Les résultats obtenus suite à l'analyse théorique et aux différentes expériences ont montré le rôle prédominant des oxydes natifs présents à la surface de InP sur les réponses des capteurs. Ces derniers interviennent également sur la stabilité de la réponse aux gaz, tout comme leurs propriétés physico-chimiques.

Les résultats des caractérisations électroniques et chimiques corroborent les résultats des essais des capteurs et permettent une modélisation de l'action du gaz sur InP.

Mots clefs : InP, épitaxie par jets moléculaire (MBE), modélisation de la physique et chimie des structures électroniques et microélectroniques à base d'InP, spectroscopie de surface de type XPS et Auger, matériaux semi-conducteurs, caractérisation électronique des couches minces (méthode Van der Pauw, mobilité des électrons, nombre de porteurs), états de surface, structures de capteur de gaz, calcul numérique.

Abstract

The aim of this Thesis was a realization and a characterization of a novel nitrogen dioxide (NO₂) sensor on the base of n-type indium phosphide (InP) epitaxial layers. First, a short survey through the air pollutants as well as their detection and monitoring methods is presented. After, the physical and chemical properties of InP (taken from literature) are detailed. In the experimental part, the description as well as the fabrication method of the gas sensor devices with different n-InP layer thickness (from 0.2 to 0.4 μm) are shown. The results of the tests under NO₂ (less than 50 ppb) as well as the results of the tests at different temperatures for different sensor series are also given. The methods and results of chemical characterization, like X-ray photoelectron spectroscopy (XPS), Auger electron spectroscopy (AES) combined with ion sputtering and Atomic Force Microscopy (AFM) are presented and applied in order to get the in-depth composition profile of InP native oxides; before and after gas action. The obtained results by Van der Pauw method are also presented i.e., the charge carrier concentration before and after action of NO₂. Finally, theoretical analysis of the influence of surface states and temperature on the electronic parameters of the InP near-surface region was also performed.

Both experimental data and theoretical analysis showed the influence of InP native oxide layer on the sensing mechanism and surface phenomena (surface Fermi level pinning, sensor stability, etc.) of InP. The results of the theoretical and experimental analysis are coherent and allow to develop a model of the gas action on the n-InP epitaxial layers.

Keywords: NO₂ gas sensor, InP epitaxial layers, III-V semiconductor, surface states, theoretical calculations, X-ray photoelectron spectroscopy (XPS), Auger electron spectroscopy (AES), electron mobility, charge carrier concentration, Hall effect, Van der Pauw method.